Applications of Electrochemical Impedance Spectroscopy to *in-situ* Dynamic Characterization of Energy Conversion and Storage Systems

by

Ying Zhu

A dissertation submitted to the Graduate Faculty of
Auburn University
in partial fulfillment of the
requirements for the Degree of
Doctor of Philosophy

Auburn, Alabama
December 14th, 2013

Keywords: impedance spectroscopy, equivalent circuit simulation,
proton exchange membrane fuel cell, solid oxide fuel cell, Ni-MH rechargeable battery

Approved by

Bruce J. Tatarchuk, Chair, Charles E. Gavin III Professor of Chemical Engineering
Mario R. Eden, Joe T. & Billie Carole McMillan Professor of Chemical Engineering
R. Mark Nelms, Professor of Electrical and Computer Engineering
Jin Wang, B. Redd Associate Professor of Chemical Engineering

Abstract

Electrochemical impedance spectroscopy (EIS) is considered as a powerful and valid technique for non-destructive *in-situ* dynamic measurement of electrochemical power systems. Together with equivalent circuit (EC) simulation, EIS is competent to perform impedance simulation, system characterization, mechanism validation, performance evaluation, and system diagnostics. The impedance measurement and simulation of both energy conversion systems and energy storage systems are presented in this dissertation.

The performance of a commercial high temperature proton exchange membrane (PEM) fuel cell tack module is studied by measuring its impedance at various current loads and different operating temperatures above 100°C. The high temperature operation is achieved by its novel phosphoric acid (PA) doped polybenzimidazole (PBI) membranes. The performance of a traditional PEM stack module operated at a temperature below 65°C is also studied by impedance measurement. A generalized EC model is proposed and validated to simulate both commercial PEM fuel cell stacks. The performance comparison between two stacks and the performance degradation of HT-PEM fuel cell stack are analyzed qualitatively and quantitatively based on EC simulation and impedance interpretation. The impedance study on PEM stacks at commercial level reveals a more realistic status of current fuel cell development.

The single cells of tubular solid oxide fuel cell (T-SOFC) fueled directly with

reformate mixture are studied by impedance measurement and EC simulation. Due to the complexity and uncertainty of SOFC mechanisms and the difficulty of SOFC operation at varying conditions, the EC simulation lacks validation for impedance interpretation. However, the impedance spectra measured under limited operation conditions still provide the preliminary validation for the physical interpretation of the proposed EC model. The measurements and simulation performed on the T-SOFC single cell tubes provide experimental data for studies on reformate fueled SOFC systems.

Impedance measurement and EC simulation are also applied to two commercial Ni-MH D-size rechargeable cells at different state-of-health (SoH). Their impedance spectra are measured and simulated at varying state-of-charge (SoC) levels. A validated EC model can be utilized to find out the correlation between battery impedance and SoC for power prediction and battery diagnostics. The prediction of battery SoC is useful to further develop a powerful and efficient smart-charging system for portable electronics and even electric vehicle development.

Acknowledgments

Table of Contents

List of Tables

List of Figures

List of Figures

Chapter 1

Backgrounds and Introduction

1.1. Motivation

After being recognized as one of the most important energy sources in the late eighteenth century, fossil fuels arose to predominate the commercial implementation of energy conversion and power generation along with the development of combustion engines. However, there are two severe challenges to combustion engines and fossil fuel systems. One is the environmental crisis brought by the consumption of fossil fuels. According to the statistic data of U.S. Energy Information Administration (EIA), over 80% of U.S. primary energy consumption comes from fossil fuels in 2011 (Figure 1.1) [1]. It includes 35% of consumption from petroleum, 25% from natural gas, and 20% from coal. Although the emergence and development of renewable and nuclear energy save the consumption of fossil fuels in some applications, the dramatically growing energy demands could not be satisfied without the increasing consumption of fossil fuels. The indisputable dependence upon the non-renewable combustion sources inevitably brings excessive emission of greenhouse gases, generation of other water and air pollutions (sulfuric, carbonic, and nitric acid, heavy metals, and organic compounds), and depletion of natural resources. U.S. Environmental Protection Agency (EPA) reported that 89% of greenhouse gas emissions in 2010 [2] were produced from combustion sources. The application of alternative energy sources can provide a feasible solution to
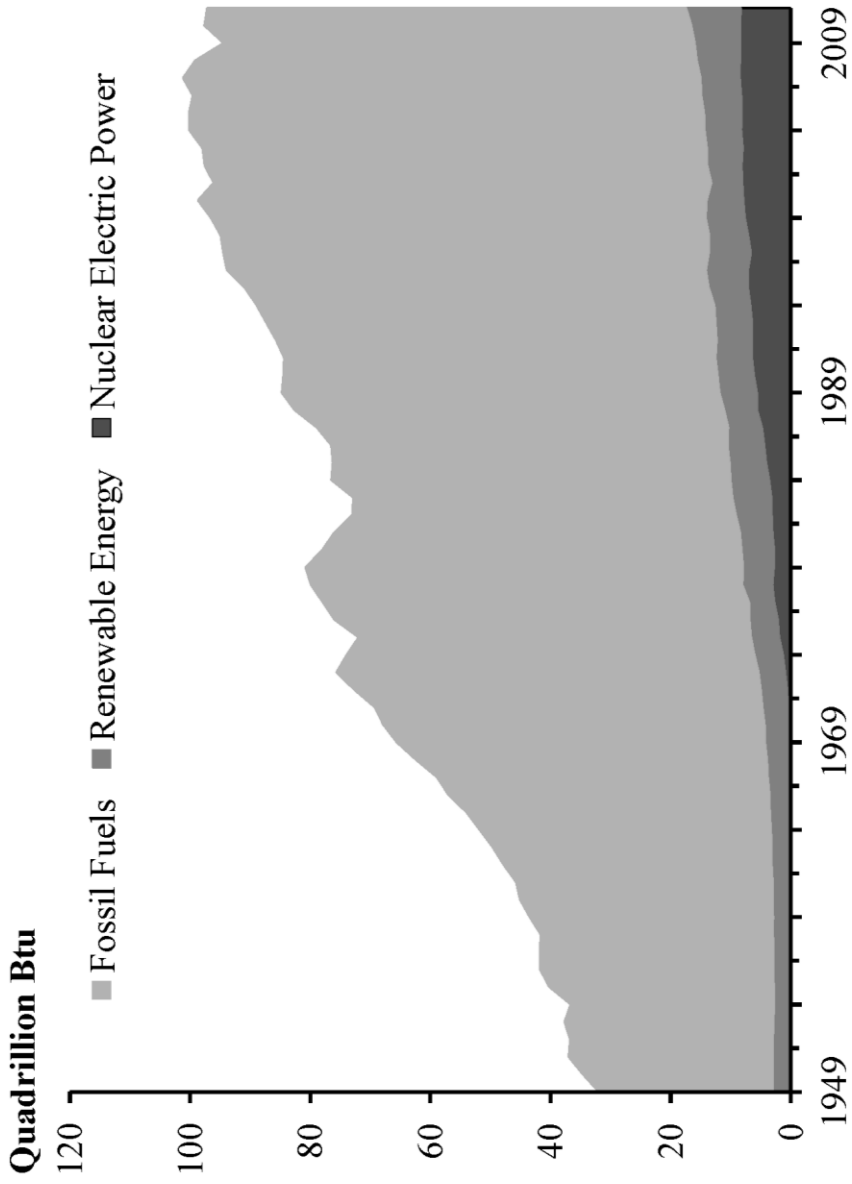
Figure 1.1. U. S. primary energy consumption estimated by major source, 1949 - 2011. The fossil fuels includes the sources of petroleum (35%), natural gas (25%), and coal (20%). (Data source: US EIA Annual Energy Review 2011 [1])

the issues of combustion sources. This idea inspires the development of Fischer-Tropsch synthetic fuels [3-5], biofuels [6, 7], and hydrogen fuel [8, 9].

The other severe issue of combustion system is its low energy conversion efficiency. Based on the current technology, the traditional automobile engines generally perform at an energy efficiency between 17% to 23% [10]. Even with further improvement, the expected thermal efficiency of a well designed combustion engine is still restricted by the intrinsic characteristics of the Carnot cycle according to the Second Law of Thermodynamics. A large portion of input chemical energy has to be consumed to overcome the energy losses due to irreversible processes and temperature gradient. The low efficiency not only decreases the economical efficiency, but also increases the pollution due to incomplete combustion of fuels. The more fuels consumed, the more economic losses will cost and the more pollution will produced. Other than developing alternative fuels for combustion systems, it improves the energy sustainability and power economics in essence to replace the combustion systems with other high energy efficient systems.

Electrochemical cell is a promising alternative to traditional combustion engine for commercial applications. Its maximum conversion efficiency is no longer vulnerable to the criteria of the Carnot cycle. The electrochemical work is a type of non-expansion work. A reversible electrochemical process at constant temperature and pressure theoretically converts all of the Gibbs energy change to electrochemical work. A theoretical comparison between a hydrogen-oxygen (H_2-O_2) electrochemical cell and a reversible heat engine shown that the reversible work of the electrochemical cell was

much larger than the heat engine at the temperatures below 950 K and even larger than twice below 500 K [11]. The development and improvement of electrochemical cells, including fuel cells and rechargeable batteries, provide the practical and effective solution for energy sustainability and efficiency.

1.2. Energy conversion systems

1.2.1. Fuel cells

Fuel cells are capable of continuously converting chemical energy to electrical energy at a high energy efficiency level without combustion. Similar to combustion engines, fuel cells produce energy in real time without energy storage. A continuous supplement of fuel is required for non-interrupted cell operation. A proper system design is important to establish a reliable and durable fuel cell system that can be used as an enduring, high efficient, and environmentally benign power source for many applications, such as global transportations, portable devices, and residential backups. Along with fuel processors, power electronics, and thermal management, fuel cells can consist a integrated system called the combined heat and power (CHP) [12]. It is able to produce both electricity and heat simultaneously from the same power source.

The concept of fuel cell was firstly demonstrated by Humphry Davy in 1801. It was then further developed into principle by Christian Friedrich Schönbein in 1838. Shortly after that, the first functional fuel cell was successfully constructed by William Grove in 1839 [13], called "gaseous voltaic battery" [14]. With Grove's demonstration model, it was successfully proved that the reaction of hydrogen (H_2) and oxygen (O_2) could produce electricity. Based on others' experience and attempts at improving the "gas

battery", Ludwig Mond and Carl Langer developed the first practical system to produce electricity. Their "new gas battery" [15] published in 1889 was considered as the prototype of current fuel cells. However, it was not until 1960s when the commercial application of fuel cell was initially accomplished in NASA's Gemini program [11]. Later in 1967, the hydrogen powered fuel cell vehicle produced by General Motors [11] inspired the research and development of fuel cell application to commercial automotives. The increasing demand for novel energy systems to replace the combustion engines accelerates the improvement of fuel cells. It is possible to attain an energy efficiency up to 45% in a commercial proton exchange membrane (PEM) fuel cell system [11], and as high as 60% by a natural gas powered solid oxide fuel cell (SOFC) device (named BlueGen, announced by Ceramic Fuel Cells Limited in 2009 [16]).

The attraction of fuel cell lies in its simple chemistry but complicated mechanisms. For general hydrogen fueled cells, the chemical reactions of half cells are hydrogen oxidation reaction (HOR) at anodes and oxygen reduction reaction (ORR) at cathodes. The detailed cell mechanisms of fuel cells change one from another with different electrode catalyst, electrolyte materials, electrode / electrolyte interface structure, fuel gas compositions, and fuel cell operating conditions. For example, the charge carrier through electrolytes of H_2-O_2 fuel cells could be protons (H^+), hydroxyl ions (OH^-), carbonate ions (CO_3^{2-}), and oxygen ions (O^{2-}) depending on different electrolyte compositions, which further changes the half cell reactions and electrode mechanisms.

1.2.2. Classifications

According to current manufacture technologies, fuel cells can be classified into five main types based on the characteristics of their electrolytes [17]. They are alkaline fuel cells (AFC), proton exchange membrane (PEM) fuel cells, phosphoric acid fuel cells (PAFC), molten carbonate fuel cells (MCFC), and solid oxide fuel cells (SOFC).

AFC utilizes aqueous alkaline solutions as electrolyte, generally potassium hydroxide (KOH) solution. The hydroxyl ions (OH^-) in the electrolyte solution are the charge carrier. This type of fuel cell is able to be operated at high temperature around 250°C with high concentrated KOH solution (85wt%) or at a temperature lower than 120ºC with lower concentrated KOH solution (35wt% to 50wt%) [18]. Although the aqueous status and sensitivity of its electrolyte brings high requirements on handling, transportation, and fuel purity, AFC is one of the most preferred choices for the Space Shuttle Program because of its low manufacture cost, high energy efficiency, and moderate operating conditions.

PEM fuel cell is equipped with solid polymer electrolyte that well overcomes the drawbacks of AFC. The aqueous status and sensitivity of electrolyte are no long the restrictions of fuel cell handling. The charge carrier of this type of fuel cell is proton. After its birth, PEM fuel cell successfully replaced the applications of AFC in many areas, especially as stationary, portable, and transport fuel cells. It performs a highest power density of about 350 mA/cm^2 among all five fuel cell types [19], and becomes one of the most promising solutions to combustion engines.

6

PAFC was the first type of fuel cells to be commercialized and widely employed for stationary applications [14]. It uses concentrated or liquid phosphoric acid (H_3PO_4, abbreviated to PA) as electrolyte. Proton transport is responsible for the electrolyte conductivity. Its optimal operating temperature ranges from 150°C to 220°C [18]. However, the development of PAFC was slowed and gradually replaced by PEM fuel cell because of the high cost of fuel processing and stack materials [18].

A molten mixture of alkali metal carbonates is employed as the electrolyte of MCFC. Unique to other types, carbonate ions (CO_3^{2-}) provide ionic conductivity of the electrolyte [14]. Its high operating temperature up to around 650°C solves several issues existing in low temperature fuel cells, such as fuel purification, catalyst activity, and heat management. However, the unique electrolyte and high temperature brings new problems of corrosion and stability. Its low power density comparing to other types of fuel cells also limits the practical applications of MCFC.

SOFC employ solid and nonporous metal oxide [18] as its electrolytes. The charge carriers could be oxygen ions (O^{2-}) and protons (H^+) depending on different electrolyte compositions. Due to restrictions on materials and fuel compositions, the development of current SOFC technology generally focuses on O^{2-} conducting electrolytes. The extremely high temperature, ranging between 600°C to 1000°C, overcomes the poisoning issues of low temperature fuel cells and improves cell kinetics and heat management. An electrical efficiency of 60% were announced to be achieved in 2009 by a natural gas powered SOFC device (BlueGen by Ceramic Fuel Cells Limited, [16]). On the other hand, the high operating temperature also becomes the cause of disadvantages. SOFCs

operating at lower temperature ranges are under development to overcome the issues of material fabrication, condition stability, and system compatibility.

In some other cases, fuel cells can also be classified according to fuel types [18]. Direct methanol fuel cell (DMFC) has a supplement of methanol without reforming. It employs the same cell structure as PEM fuel cell, but performs higher energy density. The issue hindering the commercial development of DMFC lies in its slower oxidation kinetics and sever fuel crossover [20]. Solid carbon can be supplied directly to AFC, MCFC, and SOFC without gasification. It is called direct carbon fuel cell (DCFC). A great improvement of coal-based power generation with high efficient energy conversion is achievable if DCFCs can be developed into practical systems [18].

1.2.3. Proton exchange membrane (PEM) fuel cells

1.2.3.1.Basic mechanisms

PEM fuel cell is one of the most developed fuel cell types that have large prospect in commercial applications. The employment of polymer electrolyte membranes well overcomes the limitations of aqueous electrolyte. The solid and thin electrolyte improves the durability, portability, and safety of PEM fuel cells. The half-cell reactions of PEM fuel cells are:

$$\text{Anode:} \qquad 2H_2 \rightarrow 4H^+ + 4e^- \qquad \text{(HOR)} \qquad (1.1)$$

$$\text{Cathode:} \qquad O_2 + 4H^+ + 4e^- \rightarrow 2H_2O \quad \text{(ORR)} \qquad (1.2)$$
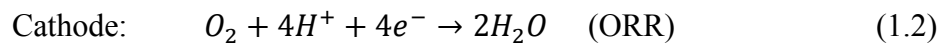
Based on the current research results, platinum (Pt) is considered as the best catalyst for reactions at both electrodes [21]. Although the detailed mechanisms are still under discussion, HOR process has proven to have very fast kinetics. The activation losses of

PEM fuel cells are usually contributed by ORR process, either controlled by the adsorption of oxygen onto the electrode or by the transport of oxygen ions to the electrode/electrolyte interfaces. The polymer electrolytes of fuel cell allow the penetration of protons only but insulate electrons, which ensures the correct direction of electron migration to produce electricity. The migration of protons though electrolytes is fulfilled by the proton-hopping mechanism along the chains of water molecules and hydrophilic acid groups bonded to the hydrophobic polymer backbones [22, 23]. The membrane conductivity significantly depends on the water uptake of the electrolyte polymers, which is sensitive to relative humidity and temperature.

1.2.3.2. Current challenges to applications

Most of traditional PEM fuel cells for commercial application are featured by perfluorosulfonic acid (PFSA) based membranes. The sulfonic acid groups are the hydrophilic groups that provide proton conductivity. And the perfluorinated polymers are the hydrophobic backbones to provide mechanical supports. Commercial products of PFSA membranes were first produced by DuPont in1970s [19], called Nafion[®]. This became a standard prototype and quickly followed by several different modified types, such as Flemion[®] by Asahi Glass, Aciplex-S[®] by Asahi Chemical, and Dow[®] by Dow Chemical. PFSA was found to be one of the most promising membranes for PEM fuel cell commercial applications. It exhibits great proton conductivity, high hydrogen and oxygen solubility, fast electrode reaction kinetics, excellent mechanical properties, but low gas permeability [22]. The commercial Nafion was reported to achieve a lifetime of over 60,000 hours under fuel cell operating conditions [20, 22].

It is critical to maintain the level of water uptake in PFSA membranes, because the proton conductivity relies on the membrane water content. Membrane dehydration occurs when the operating temperature exceeds the boiling point of water. It not only degrades the proton conductivity but also causes severe membrane shrinkage [22]. To ensure a functional and long-term operation, the temperature of PEM fuel cells has to be restricted below 100ºC under ambient pressure. On the other hand, higher temperature provides better cell performance. A temperature of around 80ºC has been considered as the optimal condition for PEM fuel cell operation under ambient pressure. However, this operating condition is close to the boiling point of water. Attentions have to be paid to gas-liquid dual phase water management.

Carbon monoxide (CO) poisoning of the electrode catalyst become one of the most critical concerns of PEM fuel cell applications. For carbon-supported Pt electrode catalyst, a CO content of only 10 ppm to 20 ppm [24] in the fuel supplement causes severe degradation in the PEM fuel cell operated at 80ºC. The HOR process at anode electrodes on Pt catalyst follows the reaction path of dissociative chemisorption of hydrogen and electrochemical oxidation of adsorbed hydrogen atoms. The catalyst poisoning is resulted from the adsorption of CO molecules to the Pt sites, competing with the chemisorption of hydrogen. The consumption of Pt sites by CO molecules impedes the following electrochemical oxidation of hydrogen. The adsorption of CO on Pt exhibits a large negative standard entropy [24]. An elevated temperature can theoretically enhance the selectivity of hydrogen adsorption on Pt. The experimental results show that the CO tolerance of PEM fuel cells can significantly increases up to 30,000 ppm at 200ºC [25].

Other challenges to the traditional PEM fuel cells include the development of hydrogen infrastructure for direct hydrogen supply, the potential applications of methanol reformate and direct methanol power systems, and thermal management and heat recovery due to low operating temperature [22].

1.2.4. High temperature (HT) PEM fuel cells

1.2.4.1. Phosphoric acid (PA) doped polybenzimidazole (PBI) membranes

Most concerns of PFSA membrane based traditional PEM fuel cells can be meliorate by elevating the operating temperature. Thus, it is desired to develop alternative membranes to overcome the temperature limitation of PFSA membranes. Three different types of alternative membranes have been found to be realistic. They are classified by its fabrication methods. The first type is fabricated by attaching charged units to a conventional polymer [23]. Most attentions to this type of alternative membranes are paid to sulfonated polymer membranes and their composites [22]. The second type is named inorganic-organic composites or hybrid, which is fabricated by incorporating a polymer matrix with inorganic compounds [23]. Modified PFSA membranes [22], especially modified Nafion membranes [19, 26], are highly recommended due to competitive advantages of PFSA membranes in PEM fuel cell applications over others. Modifications of PFSA membrane are mainly focused on the proton conductivity at higher temperature, water uptake and retain at higher temperature, low humidification operations, and mechanical stability at higher temperature. The third type of alternative membranes is acid-base polymer membranes. This type of membranes is complexes fabricated by doping strong acids or polymeric acids in conventional polymers [23]. So far, phosphoric acid (H_3PO_4, abbreviated to PA) doped polybenzimidazole (PBI) has been found to be

11

one of the most commercially promising materials for HT-PEM fuel cell under ambient pressure [19].

The advantages of PBI over other polymers, including low cost [27], high glass transition temperature [28], excellent textile fiber properties [29], and great thermal stability [30], promise itself to be an excellent polymer for membrane fabrications. One of the most significant advantages of a PA doped PBI membrane over a PFSA based membrane is that its conductivity no longer relies on the water content due to its unique proton conduction mechanism [23, 31-33], but strongly depends on the PA doping level [23, 34-36] and the operating temperature [23, 36, 37].

1.2.4.2. Proton conduction mechanisms of PA-PBI membranes

The conductivity of PA doped PBI membrane is reported to be strongly depend on PA doping level and temperature [22, 23, 34, 35, 37]. PA is doped onto the PBI backbone in two different manners. One is named as bond acids. As far as the doping level is lower than two molecules of PA per repeat unit of PBI [22, 23, 35], corresponding to two N sites for H bonding in a PBI monomer unit, the acids are stably linked to the PBI structure by H bonding. This can also be explained by the fact that the maximum degree of protonation for PA is reached at two moles PA per repeat unit of PBI [34, 37]. The conductivity at low PA doping level comes from a cooperative movement of two protons along the polymer-PA anion chain [34], that is one proton hopping away from an acid anion to form a N-H bond with the polymer and this anion accepting the proton hopping from another N-H bond at the same time. This type of proton migration provides great contribution to membrane conductivity but is not enough for fuel cell applications.

Experimental data [22, 23, 35] supported that the conductivity of PA doped PBI significantly increases with an increasing doping level of PA when more than two molecules of PA per repeat unit of PBI are doped. The bonded PA remains at a level of two molecules per repeat unit. The rest doped acid can be easily washed away, and are called the unbonded free acids. The unique proton conduction mechanism of the unbonded free PA by self-ionization and self-dehydration provides the main attribution to the conductivity [23]:

$$5H_3PO_4 \rightleftharpoons 2H_4PO_4^+ + H_3O^+ + H_2PO_4^- + H_2P_2O_7^{2-} \qquad (1.3)$$
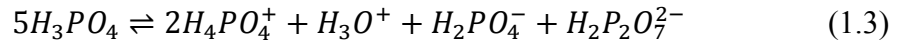
The proton conduction mechanism is described as a proton hopping mechanism along the anionic chains of $H_2PO_4^-/HPO_4^{2-}$. This mechanism significantly increase the conductivity of PA-PBI membranes to meet the requirement of fuel cell applications.

Arrhenius law is employed to explain the activation behavior of both proton hopping conduction processes [37] but with different activation energy:

$$\sigma_{P,T}T = A_P exp\left(-\frac{E_{a,P}}{R_{ig}T}\right) \qquad (1.4)$$

where A_P are pre-exponential factors, $E_{a,P}$ is the activation energy, and R_{ig} is the ideal gas constant. The subscriptions, P and T, refer to the temperature and pressure conditions under the measurement.

For PA doped PBI membranes, water is no longer the essential contributor to the conductivity. And the water drag coefficient of PBI membranes is reported close to zero [38, 39]. However, the presence of water still significantly promotes the proton conductivity. The acid further dissociate with the existence of water and provides more

charge carriers (Eq. 1.3) [23]. The addition of water also decreases the viscosity within the membrane and enhances the mobility and conductivity.

$$H_3PO_4 + H_2O \rightleftharpoons H_3O^+ + H_2PO_4^- \tag{1.5}$$
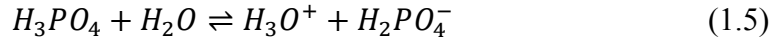
The situation becomes more complicated when the content of water increases. An increase of activation energy was reported with the increasing relative humidity (RH) at low doping level of PA [40]. This causes a decrease of conductivity with the increasing RH. Another explanation pointed out that the negative effect of reducing charge carriers due to excessive water content is more significant than the enhancement by decreasing viscosity [23], and the conductivity decreases at the presence of further addition water.

1.2.5. Solid oxide fuel cells (SOFCs)

1.2.5.1. Current development

Practical SOFC was developed in the early 1960s. However, the first solid oxygen-ion conductor, Nernst mass, was invented by Nernst much more earlier in 1899, composed of zirconium dioxide (ZrO_2) with 15wt% yttrium (III) oxide (yttria, Y_2O_3) [41]. Nernst mass was initially operated in electrolysis mode. The first prototype of ceramic fuel cell was demonstrated in 1937, shortly after Schottky suggesting the application of Nernst mass as fuel cell electrolyte in 1935 [41]. As the development of ceramic materials for SOFC electrodes and electrolytes, studies of SOFC also include [42] electrode catalysts, mechanisms and kinetics of reactions, cell optimal designs, system stability, degradations mechanisms, cell diagnostics, and scale up. Up till now, the most commonly used materials for SOFCs are yttria-stabilized zirconia (YSZ) electrolyte, nickel-zirconia cermet (Ni-YSZ) anode and lanthanum manganite ($LaMnO_3$)

based cathode. The prevailing ceramic materials provide good stability, electrical conductivity, catalytic activity, and compatibility with each others.

1.2.5.2. Basic mechanisms

The mechanisms of electrode reactions of SOFCs are much more complicated than PEM fuel cells. The rate determining steps changes with the materials of electrodes, types of catalysts, fuel compositions, and cell operating conditions. The current understandings of these mechanisms are limited. Generally, oxygen-ion conducting electrolytes are more preferred than proton conducting electrolytes for applications at commercial levels due to the feasibility of fuel compositions. CO and hydrocarbons cannot used as fuels for SOFCs with proton conducting electrolytes.

For oxygen-ion conducting SOFCs, the reaction occurring on the cathode electrodes are the oxygen reduction reaction (ORR), coupling with adsorption of oxygen and diffusion of O_2 and oxygen species. After the produced oxygen-ions transferring through the ceramic electrolyte and reaching the anode electrodes, it oxidizes the fuel composition on the anode.

$$\text{Cathode:} \quad \frac{1}{2}O_2 + 2e^- \rightarrow O^{2-} \quad \text{(ORR)} \quad (1.6)$$

$$\text{Anode:} \quad O^{2-} + H_2 \rightarrow H_2O + 2e^- \quad \text{(HOR)} \quad (1.7)$$
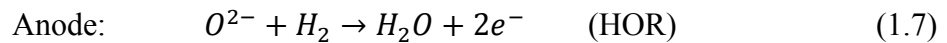
The fuels supplied to anode can be pure H_2, H_2 mixed with CO and / or H_2O, and even hydrocarbons. CO is no longer a poisoning composition under the operating temperature of SOFCs. The shift reaction is the favorable path for CO oxidation reaction when H_2O exists [41]:

$$\text{Anode:} \quad CO + H_2O \rightarrow CO_2 + H_2 \quad \text{(the shift reaction)} \quad (1.8)$$
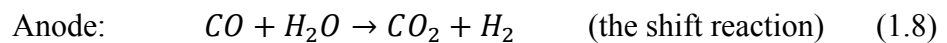
When directly fueled with hydrocarbons, the reforming process occurs internally that simplifies the fuel pretreatment. The reforming reaction produces a mixture of H_2-H_2O-CO-CO_2, which is further oxidized to H_2O and CO_2 to produce electricity. One of the important factors for the reforming process is the steam ratio in the fuel supplement. Insufficient steam may lead to the formation of carbon [41]:

$$2CO \rightarrow CO_2 + C \tag{1.9}$$

$$C_nH_{2n+2} \rightarrow (n+1)H_2 + nC \tag{1.10}$$

The formation of carbon may bring anode degradation due to its impedance to fuel supplement and its deposition on the active sites of electrode surface.

The requirements on the fuel composition for SOFCs are no longer as strict as for PEM fuel cells and other fuel cell systems operated at lower temperatures. The attention has to be paid to sulfur contaminant. A mixture of few parts per million (ppm) sulfur compounds can cause severe irreversible performance degradation in SOFCs. Up to date, the general accepted explanations for sulfur poisoning includes the formation of nickel sulfide (NiS) at anode and the adsorption of hydrogen sulfide (H_2S) on anode surface The adsorbed H_2S not only competes for active sites on anode surface with hydrogen adsorption process, but also impedes the shift reaction (Eq. 1.8). The study on sulfur poisoning mechanisms and the improvement of desulfurization technology provide significant supports to the development of SOFC systems.

1.3. Energy storage systems

1.3.1. Rechargeable batteries

Unlike traditional combustion engines and fuel cells, the operation of rechargeable batteries does not require an in-time fuel supplement. It stores energy in chemicals and converts it into electrical energy at needs. However, it takes time to recharge between two discharge processes, during which it demands an input of electrical energy.

The phrase "electric battery" was innovatively re-defined in late 1740's by Benjamin Franklin [43] when he described a series of his experiments with electricity. However, Franklin's "electric battery" referred to the pile of glass plate capacitors set up in 1748. The production and storage of energy were not achieved until Alessandro Volta designed and built his "crown of cups" and the columnar pile in late 1790s [43]. The Volta pile published in 1800 is generally acknowledged as the first battery because it fulfilled one of the most important functions of batteries: energy storage in chemicals and energy conversion to electrical energy by chemical reactions.

The phenomena of a current in opposite direction was observed by Nicholas Gautherot in 1801 from a voltaic battery consisting of two copper plates and sulfuric acid. Shortly after that, the first reversible system was successfully developed by Johann Ritter in 1802 [10]. However, the real rechargeable batteries (also known as secondary batteries) did not come out until Raymond Gaston Planté invented the first lead (Pb)-acid battery in 1859 [10]. The original concerns to the emergence and development of rechargeable batteries focused on the environmental problems caused by the toxic substances used in batteries. The pollutant substance, generally mercury, used in primary

batteries was greatly reduced by decreasing the use of mercury batteries. And the reuse and recycle of rechargeable batteries also moderated the pollutions introduced by itself.

The greater contribution of rechargeable batteries to human beings was explored and well developed with the advancing requirements of grid energy storage. Since rechargeable batteries are feathered by reversible electrochemical reactions, they are able to adapt the energy supplement to the energy demand, that is to store energy in chemicals during valley period and convert energy into electricity during peak period. Having developed for over 150 years, rechargeable batteries have been matured in the commercial applications to automotive starters, electronic products, and all other portable electrical devices daily used. Even EVs requiring light power consumption, such as bicycles and wheelchairs, have been well commercialized. The development and commercialization of pure electric automobiles powered by a build-in rechargeable battery makes it possible to save human lives out from energy crisis and environmental pollutions caused by fossil fuels and combustion engines. The development of electric rail network began from the 19th century and prevailed in UK in most of the 20th century [10]. In the past few decades, electric bicycles also predominated in city transportations in China. One of the most challenge issues is the range limitation that an EV can travel with unit battery charge time.

1.3.2. Nickel-Metal Hydride rechargeable batteries

1.3.2.1.Development and advantages

Beginning from 1980s, nickel metal hydride (Ni-MH) batteries were rapidly developed and commercialized based on the mature manufacture of nickel-cadmium (Ni-

Cd) batteries. It gradually replaced the predominance of lead-acid batteries in the market for rechargeable storage systems in early 1990s. Although Li-ion battery quickly became the dominant in the market of portable electronics, the important role of Ni-MH system in the commercial market is still irreplaceable.

Ni-MH rechargeable storage systems are able to overcome several critical concerns of other prevailing types of storage batteries. The overall performance of nickel-iron (Ni-Fe) batteries is limited by the self-discharge of iron-electrodes caused by corrosion reactions [44]. Pb-acid batteries and Ni-Cd batteries present great energy performance, but their widespread applications are disputed due to environmental contaminations. The sodium-nickel chloride systems have complicated thermal management due to the high operating temperature [45]. Nickel-hydrogen (Ni-H_2) batteries suffer from safety problems, high self-discharge rate, and low volumetric energy density despite its high gravimetric energy density. Li-ion batteries have better economical efficiency for unit energy storage on the cell level than Ni-MH batteries; however, Li-ion batteries are still more expensive at the pack level considering the safety and life-time of the systems [46].

Ni-MH rechargeable battery has identical electrolyte and cathode materials to Ni-Cd systems [17]. The electrolyte is usually a concentrated potassium hydroxide (KOH) solution, and the active material for cathode (nickel positive plate) is nickel oxyhydroxide (NiOOH) [47]. But unlike the traditional Ni-Cd systems, the hydrogen (H_2) reacted at the anode (negative plate) of commercial Ni-MH batteries is absorbed in a metal alloy [47]. Following Ovshinsky's pioneering metal alloy structure for battery electrodes [48], the

disordered AB_5 type mischmetal (Mm) alloy has been developed to the most commercial level performing a better cycle ability than other types [17].

1.3.2.2. Basic mechanisms

The basic principles and electrochemical reactions occurring during discharge process in the Ni-MH battery are described as [45] (Figure 1.2):

At the positive electrode,

$$NiOOH + H_2O + e^- \rightarrow Ni(OH)_2 + OH^-, \ E^0 = 0.52 \ V \ vs. SHE \qquad (1.11)$$

At the negative electrode,

$$MH + OH^- \rightarrow M + H_2O + e^-, \ E^0 = 0.83 \ V \ vs. SHE \qquad (1.12)$$
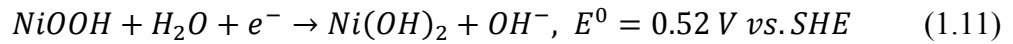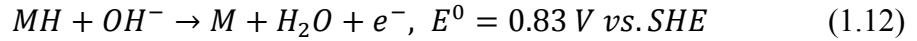
The overall cell reaction is written as

$$NiOOH + MH \rightarrow Ni(OH)_2 + M, \ E^0_{cell} = 1.35 \ V \ vs. SHE \qquad (1.13)$$
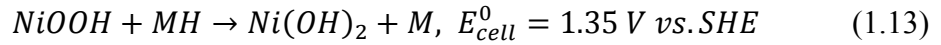
The nickel electrode is thermodynamically unstable in the sealed cell. Oxygen evolution reaction (OER) occurs at the electrode as a parallel and competing reaction when the battery is in an overcharge process (Figure 1.2). The parasitic reaction is expressed as:

$$4OH^- \rightarrow 2H_2O + O_2 + 4e^-, \ E^0 = -0.401 \ V \ vs. SHE \qquad (1.14)$$
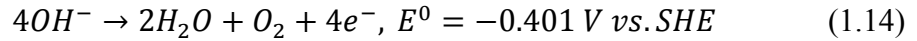
This reaction happens during the charge and overcharge processes. Reaction (1.14) starts as a parallel side-reaction, competing with the primary charging Reaction (1.11) at a certain state-of-recharge (SoR, i.e. the actual charge input as percent of the battery-rated capacity). At a higher charging rate, the difference between SoR and SoC may even start earlier due to higher potential and mass transfer limitation of the electrolyte. Hence, the HEV storage application preferably uses the 70%~80% SoC level as the higher hybrid operation limit. However, the nickel-based battery is normally designed that the cell capacity is limited by the positive electrode. The negative to positive capacity ratio varies

$$4M + 4H_2O + 4e^- \rightarrow 4MH + 4OH^-$$
$$\underline{O_2 + 4MH \rightarrow 4M + 2H_2O}$$
$$O_2 + 2H_2O + 4e^- \rightarrow 4OH^-$$

O_2 transport $\downarrow$

$$4OH^- \rightarrow 2H_2O + O_2 + 4e^-$$

charging $\leftarrow$ positive electrode $\rightarrow$ discharging

NiOOH $\leftrightarrow$ Ni(OH)$_2$

KOH

MH $\leftrightarrow$ M

charging $\leftarrow$ negative electrode $\rightarrow$ discharging

H_2 transport $\downarrow$

$$2H_2O + 2e^- \rightarrow H_2 + 2OH^-$$
$$H_2 + 2OH^- \rightarrow 2H_2O + 2e^-$$
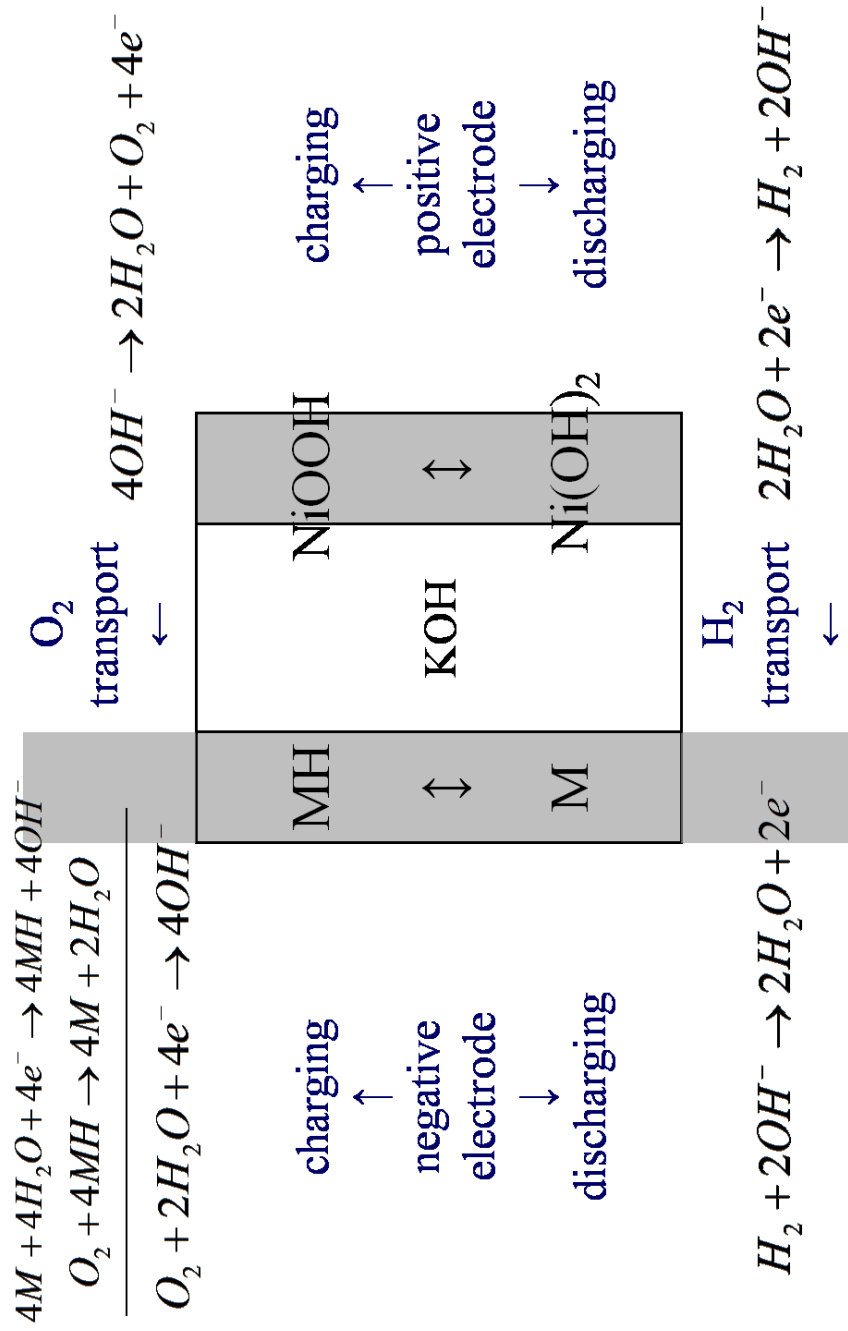
Figure 1.2. Illustration of Ni-MH rechargeable battery mechanisms and its over-charge protection mechanism.

21

from 1.5 to 2.0. The evolved oxygen from the positive electrode diffuses to the MH electrode and recombines to form water. Typically, the discharge reserve is approximately 20% of the positive capacity [45]. The range from 0 to 20% SoC level is called as deep discharge region. In order to ensure proper power output capability, the HEV energy storage considers the 20~30% SoC level as the lower hybrid operating limit [49].

1.4. Conclusion

Although the applications of energy conversion and storage systems at commercial level are still under development, the high energy efficiency and the low emissions of electrochemical cells continuously attract attentions and efforts for researches on fuel cells and rechargeable batteries. Their application to portable devices, vehicles, and large scale stationary power systems is feasible and has been realized to some extent. However, the unclear mechanisms and restrictions of operating conditions keep challenging the further improvement and commercialization. In the following chapters, the focuses are placed on *in-situ* dynamic characterizations of the HT-PEM fuel cell stack (Chapter 3), tubular SOFC cells (Chapter 5), and Ni-MH rechargeable batteries (Chapter 6). The analysis of stack degradation is also detailed for the study of HT-PEM fuel cell stack (Chapter 4). Electrochemical impedance spectroscopy (EIS) and equivalent circuit (EC) simulation are employed in this work for the in-situ dynamic measurement and simulation. The fundamental of EIS is presented in the next chapter (Chapter 2).

Reference

[1] "Annual Energy Review 2011," U. S. E. I. Administration, Ed., ed, 2012.

[2] U.S. Environmental Protection Agency, Greenhouse Gas Report Program 2010, 2012. Available at: http://www.epa.gov/ghgreporting/ghgdata/reported/index.html, 2012.

[3] B. Tatarchuk, H. Yang, R. Kalluri, and D. Cahela (Inventors), Microfibrous Media for Optimizing and Controlling Highly Exothermic and Highly Endothermic Reactions/Processes, 2011; Patent No: WO2011/057150A1.

[4] M. Sheng, D. Cahela, H. Yang, B.J. Tatarchuk, in: AIChE Annual Meeting, Nashville, TN, 2009.

[5] M. Sheng, H.Y. Yang, D.R. Cahela, B.J. Tatarchuk, Journal of Catalysis, 281 (2011) 254-262.

[6] T.L. Chew, S. Bhatia, Bioresource Technology, 99 (2008) 7911-7922.

[7] Y. Chen, Journal of Industrial Microbiology & Biotechnology, 38 (2011) 581-597.

[8] A. Demirbas, Energy Sources Part A - Recovery Utilization and Environmental Effects, 30 (2008) 924-931.

[9] L.-X. Yuan, Z.-X. Wang, T. Dong, T. Kan, X.-F. Zhu, Q.-X. Li, Journal of University of Science and Technology of China, 38 (2008) 6.

[10] C.L. Mantell, Batteries and Energy Systems, McGraw-Hill, 1983.

[11] G. Hoogers, Fuel Cell Technology Handbook, subsequent ed., CRC Press, 2002.

[12] R. O'Hayre, S.-W. Cha, W. Colella, F.B. Prinz, Fuel Cell Fundamentals, John Wiley & Sons, 2006.

[13] G. Wand, in: Fuel Cell Today, Available at: http://www.fuelcelltoday.com/about-fuel-cells/history.

[14] J. Larminie, A. Dicks, Fuel Cell Systems Explained, second ed., John Wiley & Sons, 2003.

[15] L. Mond, C. Langer, in: Proceedings of the Royal Society of London, Harrison and Sons, St. Martin's Lane, London, 1889, pp. 296-304.

[16] Ceramic Fuel Cell Limited, Ceramic Fuel Cells Achieves World-Best 60% Efficiency for its Electricity Generator Units, 2009. Available at: http://www.cfcl.com.au/Assets/Files/20090219_CFCL_Announcement_60_percent_ Efficiency.pdf.

[17] E. Barsoukov, J.R. Macdonald, Impedance Spectroscopy: Theory, Experiment, and Applications, John Wiley & Sons, 2005.

[18] EG&G Technical Services, Inc., Fuel Cell Handbook, seventh ed., 2004, pp. 427. Contract No. DE-AM26-99FT40575.

[19] S.J. Peighambardoust, S. Rowshanzamir, M. Amjadi, International Journal of Hydrogen Energy, 35 (2010) 9349-9384.

[20] B. Smitha, S. Sridhar, A.A. Khan, Journal of Membrane Science, 259 (2005) 10-26.

[21] K. Kordesch, G.R. Simader, Fuel Cells and Their Applications, Wiley, 1996.

[22] Q.F. Li, R.H. He, J.O. Jensen, N.J. Bjerrum, Chemistry of Materials, 15 (2003) 4896-4915.

[23] R.H. He, Q.F. Li, G. Xiao, N.J. Bjerrum, Journal of Membrane Science, 226 (2003) 169-184.

[24] Q.F. Li, R.H. He, J.A. Gao, J.O. Jensen, N.J. Bjerrum, Journal of the Electrochemical Society, 150 (2003) A1599-A1605.

[25] N.H. Jalani, M. Ramani, K. Ohlsson, S. Buelte, G. Pacifico, R. Pollard, R. Staudt, R. Datta, Journal of Power Sources, 160 (2006) 1096-1103.

[26] J.L. Zhang, Y.H. Tang, C.J. Song, Z.T. Xia, H. Li, H.J. Wang, J.J. Zhang, Electrochimica Acta, 53 (2008) 5315-5321.

[27] J.S. Wainright, J.T. Wang, D. Weng, R.F. Savinell, M. Litt, Journal of the Electrochemical Society, 142 (1995) L121-L123.

[28] P. Musto, F.E. Karasz, W.J. Macknight, Polymer, 34 (1993) 2934-2945.

[29] T.S. Chung, Journal of Macromolecular Science-Reviews in Macromolecular Chemistry and Physics, C37 (1997) 277-301.

[30] S.R. Samms, S. Wasmus, R.F. Savinell, Journal of the Electrochemical Society, 143 (1996) 1225-1232.

[31] H. Steininger, M. Schuster, K.D. Kreuer, A. Kaltbeitzel, B. Bingol, W.H. Meyer, S. Schauff, G. Brunklaus, J. Maier, H.W. Spiess, Physical Chemistry Chemical Physics, 9 (2007) 1764-1773.

[32] K.D. Kreuer, S.J. Paddison, E. Spohr, M. Schuster, Chemical Reviews, 104 (2004) 4637-4678.

[33] M.F.H. Schuster, W.H. Meyer, M. Schuster, K.D. Kreuer, Chemistry of Materials, 16 (2004) 329-337.

[34] R. Bouchet, E. Siebert, Solid State Ionics, 118 (1999) 287-299.

[35] Q.F. Li, R.H. He, R.W. Berg, H.A. Hjuler, N.J. Bjerrum, Solid State Ionics, 168 (2004) 177-185.

[36] C. Wannek, W. Lehnert, J. Mergel, Journal of Power Sources, 192 (2009) 258-266.

[37] R. Bouchet, S. Miller, M. Duclot, J.L. Souquet, Solid State Ionics, 145 (2001) 69-78.

[38] Q.F. Li, H.A. Hjuler, N.J. Bjerrum, Journal of Applied Electrochemistry, 31 (2001) 773-779.

[39] D. Weng, J.S. Wainright, U. Landau, R.F. Savinell, Journal of the Electrochemical Society, 143 (1996) 1260-1263.

[40] Y.L. Ma, J.S. Wainright, M.H. Litt, R.F. Savinell, Journal of the Electrochemical Society, 151 (2004) A8-A16.

[41] N.Q. Minh, T. Takahashi, Science and Technology of Ceramic Fuel Cells, Elsevier Science, 1995.

[42] S.C. Singhal, K. Kendall, High-temperature Solid Oxide Fuel Cells: Fundamentals, Design, and Applicatons, Elsevier, 2003.

[43] J.F. Keithley, The Story of Electrical and Magnetic Measurements: From 500 BC to the 1940s, Wiley, 1999.

[44] L. Ojefors, Electrochimica Acta, 21 (1976) 263-266.

[45] A.K. Shukla, S. Venugopalan, B. Hariprakash, Journal of Power Sources, 100 (2001) 125-148.

[46] E.J. Cairns, P. Albertus, Annual Review of Chemical and Biomolecular Engineering, Vol 1, 1 (2010) 299-320.

[47] B. Hariprakash, A.K. Shukla, S. Venugoplan in: G. Jürgen (Ed.), Secondary Batteries - Nickel Systems | Nickel-Metal Hydride: Overview, in: Encyclopedia of Electrochemical Power Sources, Elsevier, Amsterdam, 2009, pp. 494-501.

[48] Venkatesan S, Fetcenko MA, Corrigan DA, Gifford PR, Dhar SK, and Ovshinsky SR, MRS online proceedings library 1995; 393: 243; doi:10.1557/PROC-393-243.

[49] R.F. Nelson, Journal of Power Sources, 91 (2000) 2-26.

Chapter 2

Electrochemical Impedance Spectroscopy

2.1. Electrochemical system evaluation and diagnostics

2.1.1. Purposes and procedures

It is significantly important to obtain deep understanding of energy conversion and storage systems to approach both technical and commercial breakthrough in sustainable energy development. The purpose of system characterization is to find out how and to what degree the properties, kinetics, and other effects of a system influence its performance. The understanding of performance also provides information to assess and optimize the systems. For fuel cells, attentions are mainly paid to electrode structures, electrolyte fabrications, conductivity mechanisms, reaction limitations, catalytic poisoning, and cell degradations. And for rechargeable batteries, the important system parameters include actual capacity, rate performance, charge/discharge curves, depth-of-discharge (DoD), state-of-charge (SoC), and state-of-health (SoH).

The evaluation and diagnostics of power systems refers to the process that uses logical judgment, analytical methods, and empirical knowledge to determine the nature and causes of the conditions, situations, and problems of power systems. An integrated procedure uses various diagnostic tools to measure and monitor the parameters and behaviors of power systems under loads and off load in a certain sequence. It can be applied to system characterization, design validation, component and technique

evaluation, and operation optimization [1]. The techniques of evaluation and diagnostics are especially important for commercial products of power systems. An *in-situ* real-time technique facilitates regular system maintenance and ensures a long-term stable system performance.

Several organizations are focusing on setting up testing procedures or protocols for fuel cell . They are standard methodology focusing on system operating parameters. Martin [1] combined and summarized the procedures proposed by US Fuel Cell Council (USFCC) and Joint Research Council (JRC) into an integrated testing prototype for PEM fuel cell diagnostics. He listed each step of pretest evaluation, testing, and posttest evaluation procedures in sequence, and described the suitable techniques and their measuring parameters for each step in details. The testing procedures of JHQTF (by USFCC) and the Fuel Cell Testing & Standardization NETwork (FCTestNet) / Fuel Cell Systems Testing, Safety, and Quality Assurance (FCTes^{QA}) (by JRC) were also carried out for SOFC tests, both on single cells and cell stacks. The requirements on the supplied and generated data put forward in Joint Hydrogen Quality Task Force (JHQTF) by USFCC are [1]:

➢ applicable: industrial relevant

➢ repeatable: duplicable under the same conditions with the same type of equipment

➢ reproducible: duplicable under the same conditions with a different type of equipment

➢ scalable and serviceable: sufficient information for scale-up

These criteria are not only important for fuel cell diagnostics but also applicable to the procedures of battery tests. Only meeting the requirements, the testing procedure has practical value for studies of general power systems.

2.1.2. Non-destructive *in-situ* diagnostic tools

Generally, there are three stages in a whole set of testing procedures. They are pretest evaluation, testing, and posttest evaluation. Non-destructive diagnostic tools are required for the stages of pretest evaluation and testing. And for the testing procedure, an *in-situ* diagnostic tools is preferred for real-time measurement. For electrochemical power systems, there are three types of diagnostic tools classified as non-destructive *in-situ* techniques. They are polarization curve (*i-V* curve), current interruption (CI), and electrochemical impedance spectroscopy (EIS).

Polarization curve, also called "*i-V*" curve, explicitly illustrate the relationships of current and cell potential. In some cases, the dependence of the cell output power on current is also plotted. It can be conducted either by a steady-state or a transient state technique [1]. In steady-state mode, the polarization curve is simply recorded by measuring the cell potential at each current step. And a slow current sweep rate can be utilized to obtain a transient polarization curve.

CI is capable to obtain the ohmic resistance of an electrochemical system directly from measurement. Since the response of physical processes to the current change is much faster than electrochemical processes, ohmic response can be distinguished from electrochemical responses by their different voltage transient behaviors when the current applied to the electrochemical system is interrupted. CI technique has been applied to the measurement, evaluation, and diagnostics of alkaline dry cells [2], rotating disk electrodes (RDE) [2], cathodes of molten carbonate fuel cells (MCFC) [3], single direct methanol fuel cells (DMFC) [4], a small scale DMFC stack [5], and PEM fuel cells [6-8].

29

Other than polarization curve and CI techniques, EIS does not obtain data directly from measurement. It generates the system impedance over a spectrum of frequencies from the measuring data of amplitudes and phase shifts. However, the great prospect of EIS lies in characterizing chemical reactors in terms of electronics. Chemical, electrochemical, and physical processes occurring in electrochemical systems are simulated in chemical process simulators (ASPEN for example) to study the mass balance, thermodynamics, and kinetics of the systems. The moles are able to be converted to electrons; however, this is where chemical engineering typically ends. On the other side, electrical circuits are simulated in analog circuit simulators (PSpice for example) to predict circuit behaviors and provide industrial standard solutions, such as the non-linear transient analysis for voltage and current versus time. It is EIS that generates equivalent circuits (EC) and establishes the connection between the world of chemical engineering (chemical processes) and electrical engineering (power electronics). Depending on the power applications, the unique load requirements are described in circuit simulators. The minimum weigh and volume of the power supplies can be designed to meet the load requirements. In this way, the *in-situ* real-time measuring technique as well as EC simulation systematically provides a competent methodology for integrated system design, operation, and control [9].

Since EIS has the ability to establish the connection between the load outputs and the power supply, it can be applied to smart batteries for power prediction. A proper charge-discharge process is significantly important for maintaining rechargeable battery at a long-term well-performing status. The phrase of "smart battery" was proposed in 1990s [10] and gradually developed to a technically defined concept. It enables communications

between a rechargeable battery and its host system. The requirement of electric vehicle (EV) commercialization further developed the concept of "smart" into EV charging infrastructure. A real smart charging system should be able to determine SoC of rechargeable batteries and protect them from over-charging process. However, SoC cannot be measured directly. One of the generalized method is to monitor the voltage of the battery and estimate its SoC level according to its discharge curve. Accuracy is the upmost concern of this method, because the voltage difference of a unit battery is in small magnitude and sensitive to current, temperature, and battery chemistry. Compensation variables are usually required for accuracy corrections. Impedance is sensitive to current, temperature, and battery chemistry. It can be accurately measured by EIS as well as its change with SoC. Thus, EIS is expected to be applied to SoC determination and power detection for battery control and testing.

2.2. Electrochemical impedance spectroscopy (EIS)

The history of impedance spectroscopy (IS) can be dated back to 1880s, when Heaviside initially introduced the concept of "impedance" [11, 12] to his research on electromagnetic induction. It was almost a century lag behind the first measurement of direct current (*dc*) resistance (the so called "pure resistance") conducted by Georg Simon Ohm in early 1800's and published later in 1825 [13]. Kennelly [14] quickly followed up Heaviside's idea and extended the concept of "impedance" to generalized conductors in 1883. He also mathematically defined the total impedance, in a complex plane, as the vector sum of its resistance, its inductance-speed[1], and the reciprocal of its capacity-

---

[1] Inductance-speed: The product of angular frequency and inductance, ωL.

speed[2] [14]. However, the technique of IS itself did not come out until Nernst [15] employed Wheatstone bridge to measure dielectric constants in 1894.

During the past century, impedance measurement contributed to the characterization of materials and devices, study of electrochemical reaction systems, corrosion of materials, and investigations of power sources. According to different materials and systems it applied to, IS can be classified into two branches [16]. The one following Nernst's initial achievement is called non-electrochemical IS. It applies to dielectric materials, electronically conducting materials, and other complicated materials with combining features [16]. The other branch, newly coming out based on the development of non-electrochemical IS, is named electrochemical impedance spectroscopy (EIS). It focuses on IS applications to ionically conducting materials and electrochemical power sources [16]. The popularity of IS keeps improving especially after the prevailing of electronics and computers. Not only is it capable of dealing with complex processes, reactions, and variables through simple electrical elements, it is also a valid technique for power source diagnosis and system quality controls.

2.2.1. Measuring techniques

EIS measurement is conducted by superimposing an electrical stimulus on the output of the tested electrochemical system and measuring the resulting signal. The impedance of the measuring system is then calculated from the stimulus and its resulting signal by transform functions and Ohm's Law. In this way, the performance of the system under

---

[2] Capacity-speed: The product of angular frequency and capacitance, ωC.

measurement can be studied as a black box, which is described as "feeling an elephant that we cannot see" in Mark Orazem and Tribollet's book [15]. Thus, for an electrochemical system, it is possible to study the properties of its interfaces and materials without taking the system apart. The word "*in-situ*" generally refers to this type of techniques that characterizes electrochemical systems under operation with the help of voltage, current, and time, distinguishing from "*ex-situ*" techniques which studies individual components departed from electrochemical systems in a non-assembled and non-functional form [17].

Different kinds of electrical stimulus can be used in EIS measurement, including a step function of voltage, a random noise, a single frequency signal, and any other types of stimuli generated by combining the foregoing three ones [18]. With the increasing commercial availability of measuring instruments, the characterization of electrochemical systems generally employs an *ac* signal (either a small *ac* voltage or *ac* current). In most cases, it is also called "*ac* impedance".

Several impedance measuring instruments are commercially available, including products from EG&G Inc., Gamry Instruments, Scribner Associate Inc., and AMETEK (Solartron Analytical and Princeton Applied Research). An instrument set basically consists of a potentiostat, or known as an electrochemical interface, connecting to a frequency response analyzer (FRA). Besides, a complete circuit connection for measurement requires an electronic load. Specifications of different instruments are designed for different scales of measurements. The feasibility and accuracy of measurements are determined by the frequency resolution, frequency accuracy, and bandwidth of instruments and electronic loads. For example, batteries and fuel cells are

low impedance systems, usually much lower than 1 Ω (sometimes even down to milliohms) [18]. Their impedance measurement requires a high current and a low frequency bandwidth. A typical connection diagram for *ac* impedance measurement of a traditional PEM fuel cell stack is presented in Figure 2.1 [19]. The commercial instrument connected in this measuring system is Gamry FC350[TM] Fuel Cell Monitor. It is featured by its capability to measure impedance at high current levels. The four-terminal connection is commonly used for low impedance measurement (such as batteries and fuel cells) to avoid measurement errors led by the impedance of cables and connections [18].

It is worth to noting that the choice of *ac* signal value have great effect on impedance measurement. The reliability of EIS analysis is based on the assumption that the measured system is linear. It is also important to keep the system in a relatively steady state throughout the measurement to ensure the accuracy of the measured data. The measured impedance data may appear scattered and unregulated if the signal is too weak to excite a measurable perturbation. On the other hand, the signal has to be small enough to keep the measuring system within the range of pseudo-linearity. A larger signal also brings more extra heat that breaks the steady state of the system. The data measured at low frequencies behave more sensitive to the strength of the applied *ac* signal due to larger impedance at lower frequency [20]. Correspondingly, an appropriate value of the signal should be well picked to ensure the accuracy of the impedance data measured. It is not necessary to determine an exact value for the input signal, however, it has to be controlled in a certain range which is neither so small that the output signals are too weak
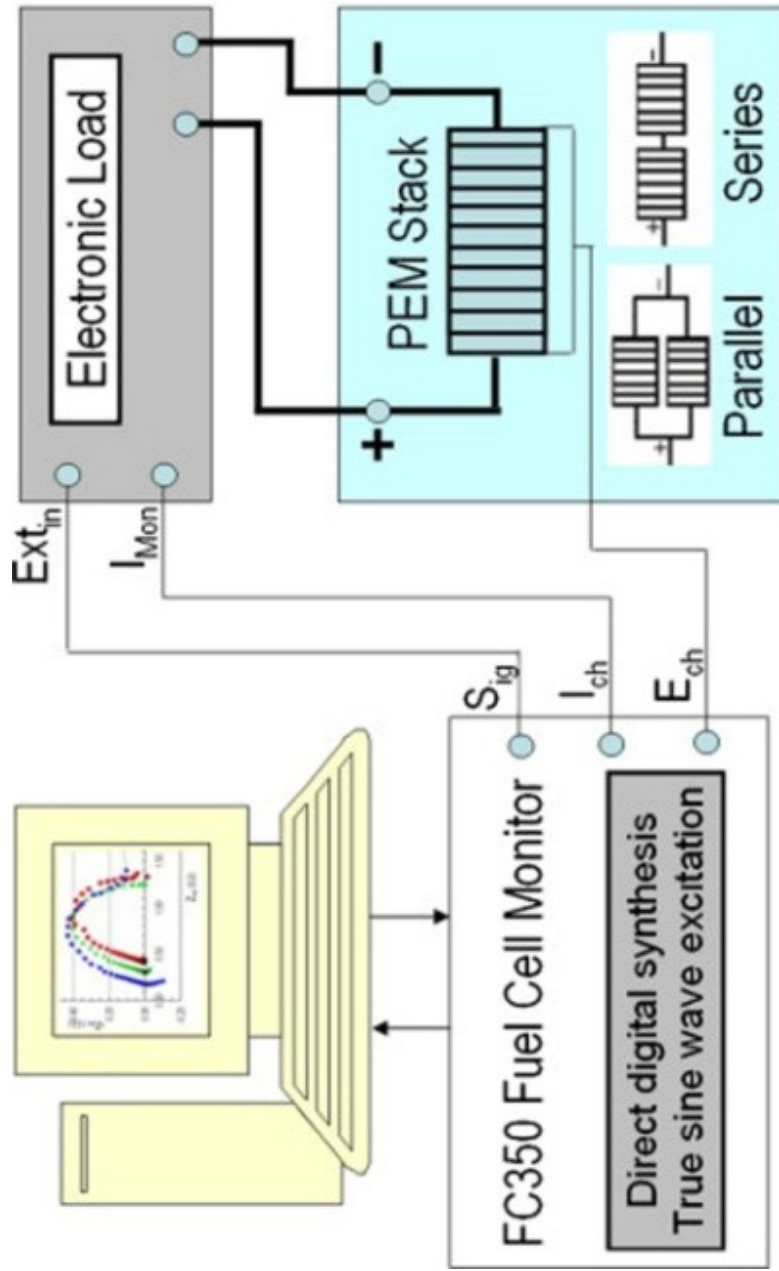
Figure 2.1. A typical connection diagram for *ac* impedance measurement conducted on PEM fuel cell stacks: single stack, two stacks in parallel arrangement, and two stacks in series arrangement [19].

to be measured, nor so large that a great distortion is introduced into measurements. Different signal values can be trailed before measurements to find out a suitable one.

There are two traditional modes for impedance measurements according to different regulating variables: potentiostatic mode and galvanostatic mode. Potentiostatic mode employs a small *ac* voltage signal with fixed amplitude and measures the resulting *ac* current. In this mode, the *dc* voltage is controlled at a certain value that facilitate the control of system linearity. Reversely, a small *ac* current signal with fixed amplitude is superimposed on the regulated *dc* current in galvanostatic mode. The resulting *ac* voltage is measured. Galvanostatic mode provides higher accuracy than potentiostatic mode when measuring low impedance systems because the voltage can be measured more accurately than controlled. This mode is more welcomed where a steady *dc* current is required during the entire measurement. However, it is difficult to control the resulting *ac* voltage strictly within the linear range especially at low frequencies.

A novel measuring mode, hybrid mode, is put forward to overcome the drawback of galvanostatic mode. It was firstly known as variable-amplitude galvanostatic mode when studying H-cells with copper/sea water system [20]. The validation and accuracy of impedance measurement rely on the pseudo-linear behavior of electrochemical systems. The current signal is regulated before measurement of each data point in hybrid mode to ensure that its resulting voltage stays within the linear region. A desired voltage perturbation and an estimated impedance magnitude are set before the measurement. The initial current perturbation is calculated by [9]:

$$\Delta I_1 = \Delta V / |Z_{est}| \tag{2.1}$$

ΔI_1 is the amplitude of the current perturbation superimposed on the *dc* load for measurement at the first frequency point. ΔV is the amplitude of the desired voltage perturbation. $|Z_{est}|$ is the magnitude of the system impedance estimated before the measurement. The measured impedance value at this frequency point is then recorded as Z_1. The current perturbation employed for each following frequency point is calculated by [9, 20]:

$$\Delta I_n = \Delta V / |Z_{n-1}| \tag{2.2}$$

ΔI_n is the amplitude of the current perturbation used at the nth measuring point, and $|Z_{n-1}|$ is the magnitude of the system impedance measured at the $(n\text{-}1)^{th}$ point. Similar to galvanostatic mode, the power systems are studied under constant current density. However, the current signal applied to the systems at each measuring point is different. By the step of signal regulation, it is able to yield the *ac* voltage at the desired magnitude. The behaviors of tested power systems are ensured in the pseudo-linear region.

2.2.2. Data presentation

The two most preferred methods to present impedance data are the Nyquist plot and the Bode plot. Nyquist plot, named after Harry Nyquist, is a polar plot of the transfer function [21]. In some publications, it is also called the complex-plane plot or the Argand plot [18]. An example of Nyquist plot is shown in Figure 2.2a (plotting method adapted from [21]). This impedance spectrum is a set of continuous complex impedance points produced by the circuit diagram [11] over a certain range of frequency (from zero to positive infinite in Figure 2.2a). The x-axis presents the real component of the impedance points and the y-axis presents their negative imaginary component. In this way, the capacitive impedance arcs are flipped to the first quadrant in the plot. As the frequency

37
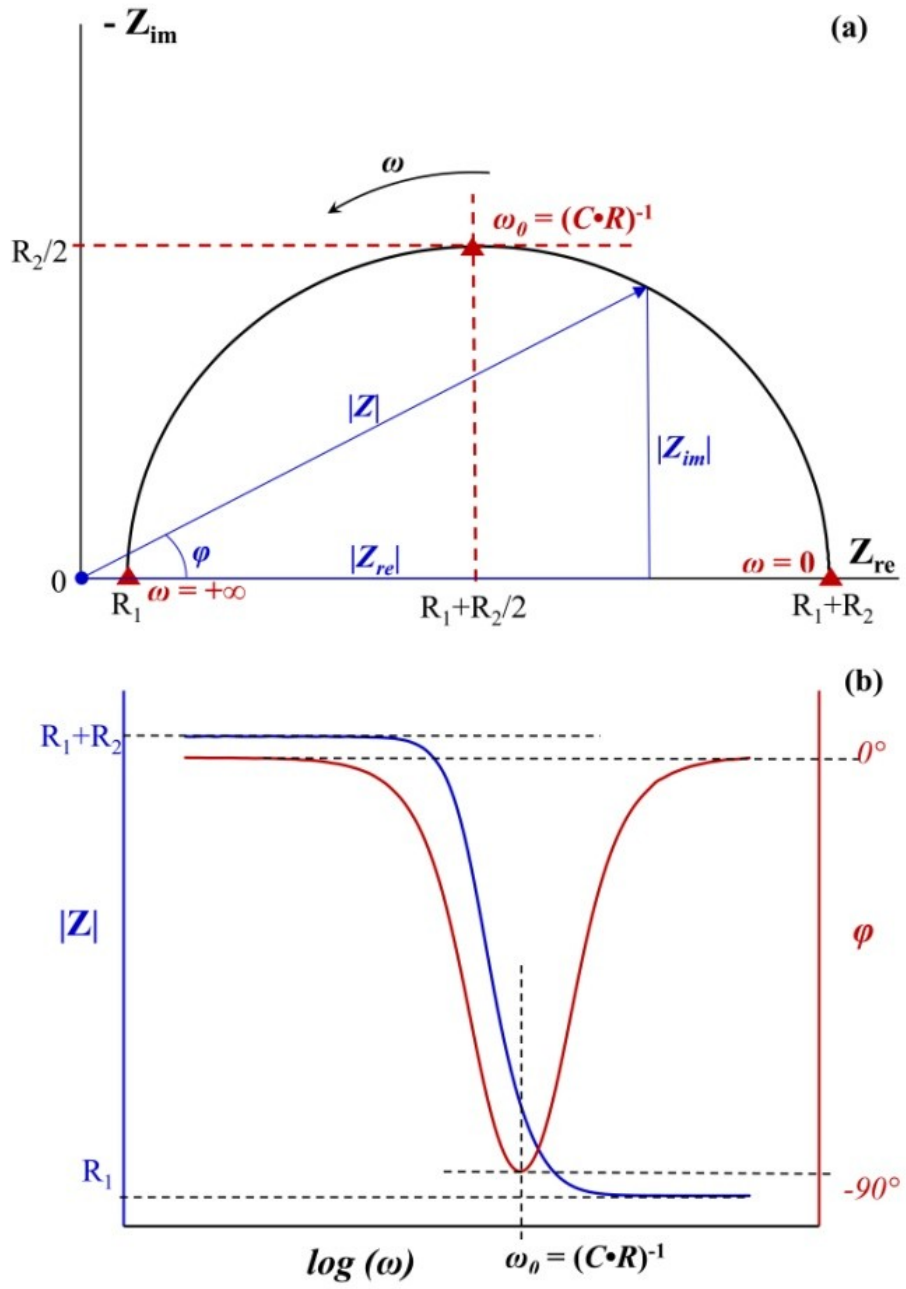
Figure 2.2. Examples of (a) Nyquist plot and (b) Bode plot generated by the EC diagram [11].

goes from zero to positive infinite, the impedance points move toward the origin of the plane. The impedance value and phase angle of the points can be calculated from the Nyquist plot:

$$|Z| = \sqrt{|Z_{re}|^2 + |Z_{im}|^2}$$ (2.3)

$$tan\,\varphi = \frac{|Z_{im}|}{Z_{re}}$$ (2.4)

Nyquist plot can provide plenty information of impedance variables but failed to present their frequency dependence. Bode plot, named after Hendrik W. Bode, overcomes this inadequacy. It displays the frequency dependence of a linear, time-invariant system, usually shown in logarithmic axis. Figure 2.2b is an example of Bode plot generated by the diagram [11]. It includes a magnitude plot presenting the magnitude of impedance ($|Z|$) versus the logarithmic angular frequency (log ω), and a phase plot presenting the phase shifts of *ac* current to *ac* voltage (φ) against the logarithmic angular frequency (log ω).

2.2.3. Equivalent circuit (EC) simulation and data interpretation

There are mainly two methods to derive models for impedance simulation, visually summarized and classified in a flow chart by Macdonald [16]. One mathematically establishes models based on the theory, which puts forward a hypothesis for physical and chemical processes contributed to the impedance. The other one utilizes empirical models, called equivalent circuits (EC). Some researchers also presented a combining method with both of them [22]. The values of certain variables, such as ohmic resistance, were acquired directly from the empirical EC simulation and used as known variables to establish the mathematical model. Whichever employed, the validations of data

themselves are essential before simulation. The relations originally published by Kramers (1929) and Kronig (1926) (K-K Transforms) became a simple but effective method for data validation from 1980s, in order to ensure the causality, linearity, and stability of the measured systems [23, 24]. Both the mathematical models and the empirical ECs also have to be validated before data interpretation and system characterization. The fitting programs, generally following the procedures of complex nonlinear least squares (CNLS) fit algorithm (such as LEVM [25] and EQUIVCRT [26]), are employed to validate the proposed EC models by estimating the parameter standard deviation and the goodness of fit [25].

Comparing to mathematical models, deriving an EC model is easier, faster, and more intuitive. An EC diagram is a physical electrical circuit which produces a similar load response to the measured system, derived based on both experiences and theories. The overpotential losses of the testing cell (electrochemical systems) are introduced by the impedances contributed by different physical and chemical processes occurring in the cell (electrochemical system). The impedances of different processes predominate different frequency regions. Thus, they can be identified and mechanistically discriminated by EC simulation according to different process relaxation times. However, the physical interpretation of circuit elements is not straightforward due to the uncertainty of EC diagrams. Different arrangements or combinations of EC elements can produce the same dynamic response when three or more elements are employed in one EC diagram. The only solution to overcome this difficulty is acquiring sets of impedance data with different variables and changing conditions.

2.2.3.1.   Ideal EC elements

Resistor R, capacitor C, and inductor L are three fundamental elements reflecting ideal processes. Their mathematical expressions and physical meanings [27] are summarized in Table 2.1. Z is the impedance of the elements. Y is the reciprocal of Z, called admittance. The impedance behaviors of an ideal resistor, capacitor, and inductor are sketched out individually in Figure 2.3 (plotting method adapted from [27]).

The impedance of an resistor is calculated at $R = 10$ Ω. The real part of its impedance equals to its resistance. The impedance of an ideal resistor does not have imaginary part. As frequency changes, the impedance of an ideal resistor keeps constant.

The impedance of an capacitor is calculated at $C = 0.01$ F (at frequency from 0.04 Hz to 100 kHz). It only has imaginary part. And this imaginary part is in negative value. The magnitude of an ideal capacitor's impedance decreases with increasing frequency.

The impedance of an ideal inductor is calculated at $L = 0.01$ H (at frequency from 0.1 mHz to 7 kHz). It also has imaginary part only, but in positive value. The magnitude of an ideal inductor's impedance equals to the value of its imaginary part. It increases with increasing frequency.

2.2.3.2.   Non-ideal EC elements

The three ideal EC elements are not able to reflect non-ideal factors in practical cases. A generalized element, constant phase element (CPE) Q, was developed to simulate non-ideal processes. Q reflects the exponential distribution of time constants. This non-ideal distribution may be caused by the surface roughness and vary thickness of

Table 2.1. The mathematical expressions and physical meanings [27] of ideal EC elements: *R*, *C*, and *L*.

Element Symbol	Element Name	Impedance Expression	Physical Interpretation
R	Resistor	$Z_R = R$	Contributed by energy losses, dissipation of energy, and potential barrier
C	Capacitor	$Z_C = \dfrac{1}{j\omega C}$	Contributed by accumulations of electrostatic energy or charge carriers
L	Inductor	$Z_L = j\omega L$	Contributed by accumulations of magnetic energy, self-inductance of current flow, or charge carrier's movement
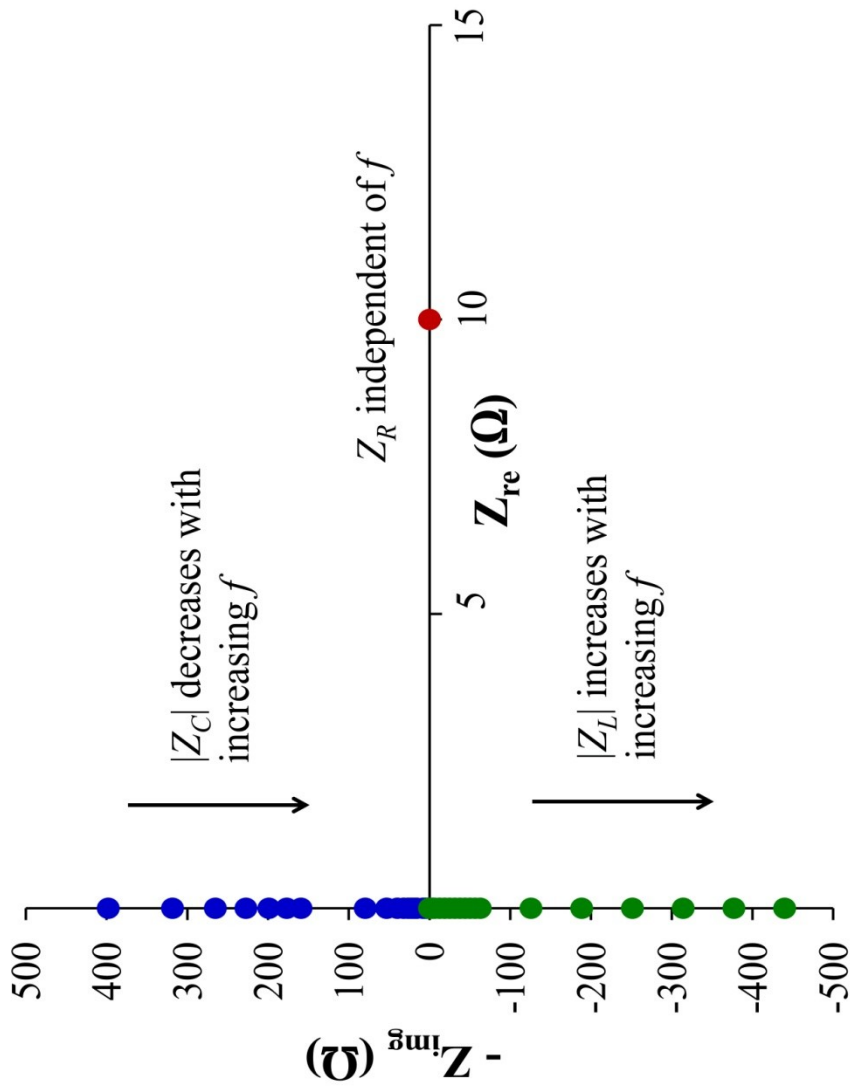
Figure 2.3. Illustration of impedance spectra of ideal EC elements in Nyquist plot.

43

electrodes, unevenly distributed current, and non-homogeneous reaction rate. In the impedance expression of Q [18]:

$$Z_Q = \frac{1}{Y_{0,Q}(j\omega)^\alpha} \tag{2.5}$$

the exponent α reflects the degree of non-ideality. When the value of α in the expression of Q equals to 1, 0, and -1, it can be found that Eq. 2.5 becomes the same as the expression of capacitor C, resistor R, and inductor L, respectively. Figure 2.4 (plotting method adapted from [27]) shows two sets of impedance data produced by the expression of Q with $A = 100$ F^{-1}. They behaves as straight lines across the origin in Nyquist plot. When the value of α decreases from 0.8 to 0.5, the slope decreases. The angle of the incline equals to $(\alpha \cdot 90)°$.

Emil Warburg developed the expression of the impedance response for diffusion processes in 1899 [15]. This is now called Warburg diffusion element (W). It is used to simulate an one-dimensional unrestricted diffusion process to a large planar electrode. The impedance expression of Z_W is [28]:

$$Z_W = \frac{\sigma}{\sqrt{\omega}} - j\frac{\sigma}{\sqrt{\omega}} \tag{2.6}$$

Thus, the magnitude of W ($|Z_W|$) can be calculated by:

$$|Z_W| = \sqrt{2}\frac{\sigma}{\sqrt{\omega}} \tag{2.7}$$

In Eq 2.6 and 2.7, ω is the angular frequency, the same as in Eq 2.5. And σ is called the Warburg coefficient, given by [28]:

$$\sigma = \frac{R_{ig}T}{\sqrt{2}\cdot n^2 F^2 A}\left(\frac{1}{D_O^{1/2}C_O^*} + \frac{1}{D_R^{1/2}C_R^*}\right) \tag{2.8}$$

where, R_{ig} is ideal gas constant; F is the Faraday constant; n is the stoichiometric number of electrons involved in the standard chemical reaction system (Eq. 2.9); and D_O and D_R
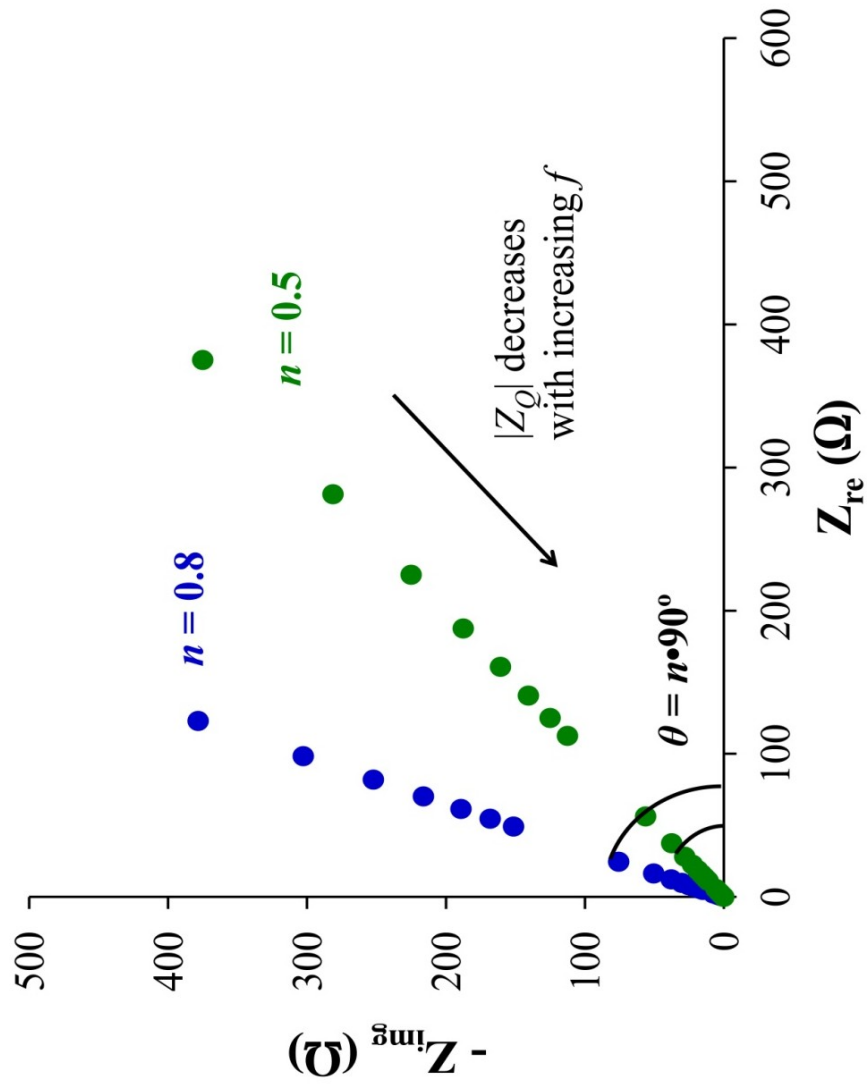
Figure 2.4. Illustration of impedance spectra of constant phase element (Q) and Warburg element (W) in Nyquist plot.

are diffusion coefficient of the oxidized and reduced form of the reaction species; and $C_O{}^*$ and $C_R{}^*$ are bulk concentration of species, respectively.

$$O + ne \rightleftharpoons R \tag{2.9}$$

For EC simulation, a more simplified and straight way is to employ the magnitude of admittance at $\omega = 1$ rad s^{-1} as model parameter [29]:

$$Y_0 = \frac{1}{\sqrt{2} \cdot \sigma} = \frac{n^2 F^2 A}{RT} \left(\frac{1}{D_O^{1/2} C_O^*} + \frac{1}{D_R^{1/2} C_R^*} \right)^{-1} \tag{2.10}$$

The impedance spectrum of Warburg element behaves as a straight line with unit slope in Nyquist plot, exactly the same as a CPE (Q) with the exponent $\alpha = 0.5$ (Figure 2.4).

Finite diffusion element (FDE) O, or sometimes called Porous Bounded Warburg, was established based on Warburg element (W). Its application is extended to a rotating disk electrode (RDE), where diffusion occurs over the Nernst Diffusion Layer (NDL), that is a diffusion layer with finite thickness. The expressions for Z_O [30] is:

$$Z_O = \frac{1}{Y_0 \sqrt{j\omega}} \tanh\left(B \sqrt{j\omega} \right) \tag{2.11}$$

where, Y_0 is the same parameter as the one employed in the model of Warburg element with the same physical meaning and the same expression equation (Eq. 2.10); and

$$B = \delta / \sqrt{D} \tag{2.12}$$

which is called time constant. In Eq. 2.12, δ is the thickness of the diffusion layer and D is the diffusion coefficient. Figure 2.5 [27] shows a typical Nyquist plot of an O element. The intercept of the spectrum to the real axis is the impedance of FDE [30] calculated at $\omega = 0$:

$$R_O = Z_O(\omega = 0) = \lim_{\omega \to 0} \frac{\tanh(B\sqrt{j\omega})}{Y_0 \sqrt{j\omega}} = \lim_{\omega \to 0} \frac{B\sqrt{j\omega}}{Y_0 \sqrt{j\omega}} = \frac{B}{Y_0} \tag{2.13}$$
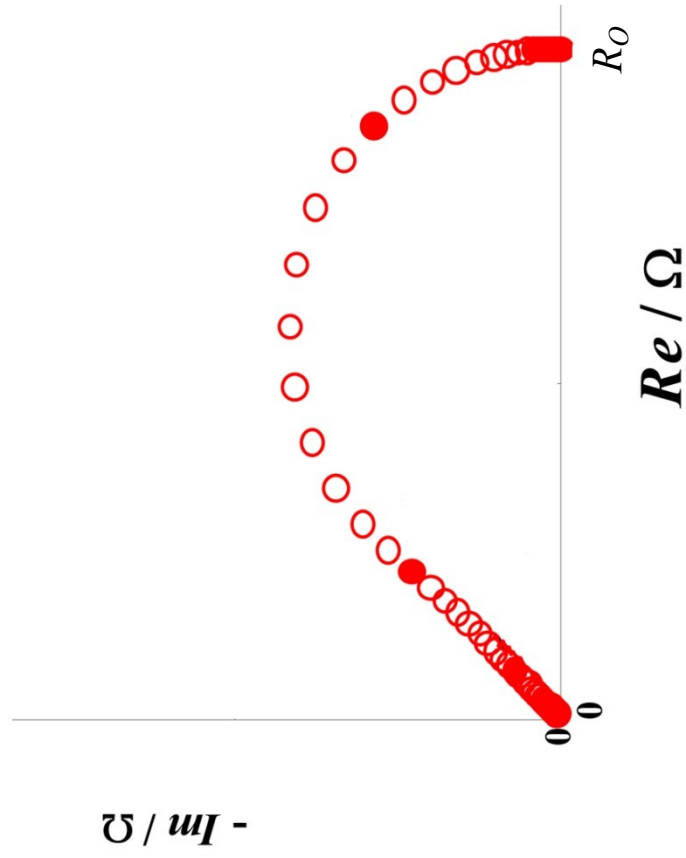
Figure 2.5. Illustration of impedance spectrum of finite diffusion element (O) in Nyquist plot [27].

The impedance spectrum of FDE (O) presents the same behavior as Warburg element (W) at higher frequency region. As frequency decreases, it changes to an arc similar to (CR), detailed in the following section.

2.2.3.3. Typical EC circuits

The (CR) circuit is one of the basic combinations commonly used in EC simulations. The elements enclosed in parentheses are connected parallel to each other. And the square brackets indicate that the elements enclosed are connected in series. For example, (CR) means a pure capacitor C and a pure resistor R are parallel in the connection; while [31] means a pure capacitor and a pure resistor are connected in series. Figure 2.6 presents the Nyquist plot of (CR). It is a semi-circle centering at ($R/2$, 0) with a radius of $R/2$. As the angular frequency ω increases from 0 to ∞, the summit of the semi-circle is reached at:

$$\omega = \omega_0 = \frac{1}{CR} \tag{2.14}$$

The (CR) circuit can be employed to simulate an ideal double-layer process. The non-ideal one requires the circuit of (QR). The element Q replaces C to reflect the non-ideality of a double-layer process. (QR) behaves as a depressed semi-circle having its center dropped down below the Z_{real} axis (Figure 2.6). The degree of the depression is presented by the exponent α of the Q element.

The EC diagram [11] mentioned previously in Figure 2.2 is another fundamental combination. Based on the spectrum of (CR), [11] shifts horizontally along the positive Z_{real} axis in Nyquist plot (Figure 2.2a). The smaller intercept with the Z_{real} axis equals to
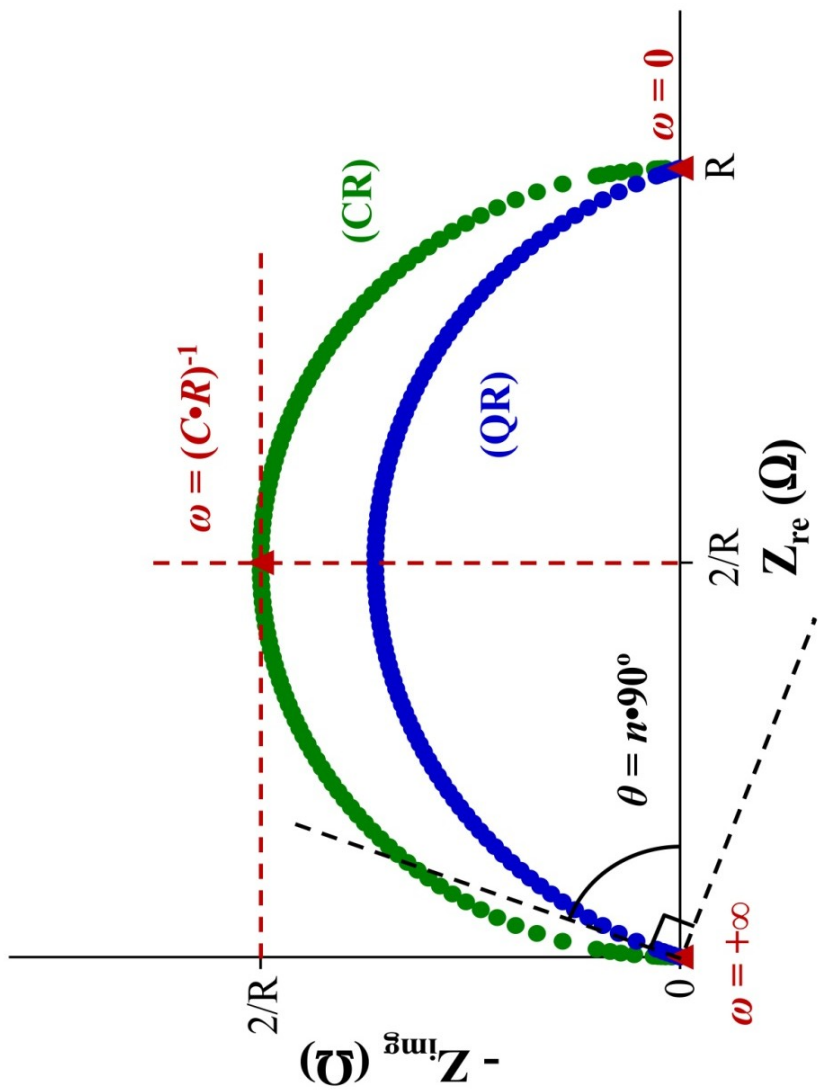
Figure 2.6. Illustration of impedance spectrum of (*CR*) sub-circuit in Nyquist plot, along with the spectrum of (*QR*) sub-circuit.

49

the resistor R_1. And the larger intercept equals to the sum of R_1 and R_2. The center of the semi-circle is $(R_1+R_2/2, 0)$ and its radius is $R_2/2$.

Randles circuit $[R_\Omega(C_{dl}[R_{ct}W])]$ considers the contribution from a diffusion process. It consists of one ohmic resistance R_Ω, one parallel $(C_{dl}R_{ct})$ sub-circuit behaving as a semi-circle in Nyquist plot, and one infinite diffusion element W behaving as a unit slope line at the lowest frequency region. Figure 2.7 [32] sketches the impedance spectrum of a Randles circuit. The dash lines illustrate the overlap region of $(C_{dl}R_{ct})$ and W.

The impedance spectra of a typical EC diagram commonly used to simulate electrochemical cells is sketched in Figure 2.8 [33]. This diagram consists of three time constants. Its total impedance is the sum of the ohmic losses Z_Ω, the anode polarization losses Z_a, the cathode polarization losses Z_c, and the mass transfer losses Z_m. The ohmic losses are simulated by one pure resistor R_Ω. Its value is represented as the smaller intercept on the real axis. The anode and cathode polarization losses are simulated by a parallel (CR) sub-circuit respectively. Their impedance spectra look like two overlapping semi-circle in Nyquist plot. Some electrochemical systems, like Ni-MH batteries, have strong Warburg behavior in the low frequency region for the mass transfer processes. The diagram can be expressed as $[R_\Omega(C_aR_a)(C_c[R_cW])]$. However, some do not always show this behavior obviously, such as PEM fuel cells. The low frequency arc can be simulated by a parallel (QR) sub-circuit instead of a pure Warburg element. The diagram is expressed as $[R_\Omega(C_aR_a)(C_c[R_c(Q_mR_m)])]$. The Warburg element and sub-circuit (Q_mR_m) are connected in series with R_c because the mass transfer processes are considered as cathodic processes.

50
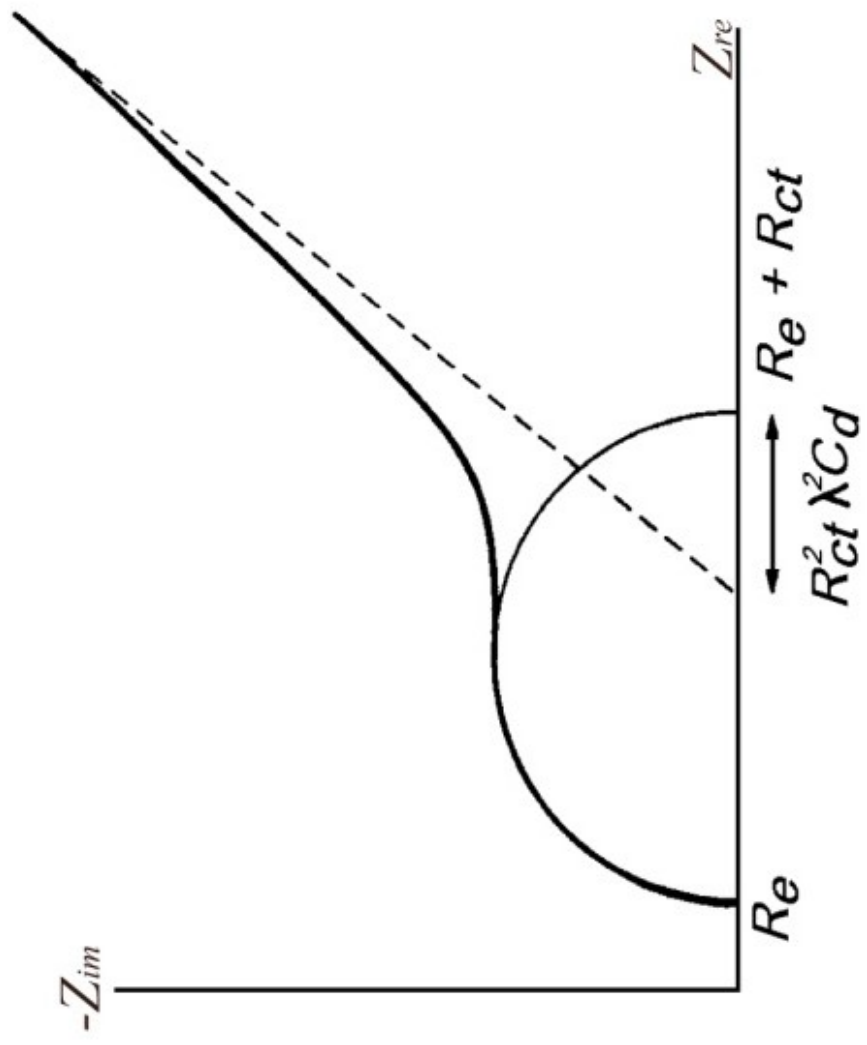
Figure 2.7. Nyquist plot of Randle's circuit ([32] Courtesy of Solartron Analytical).
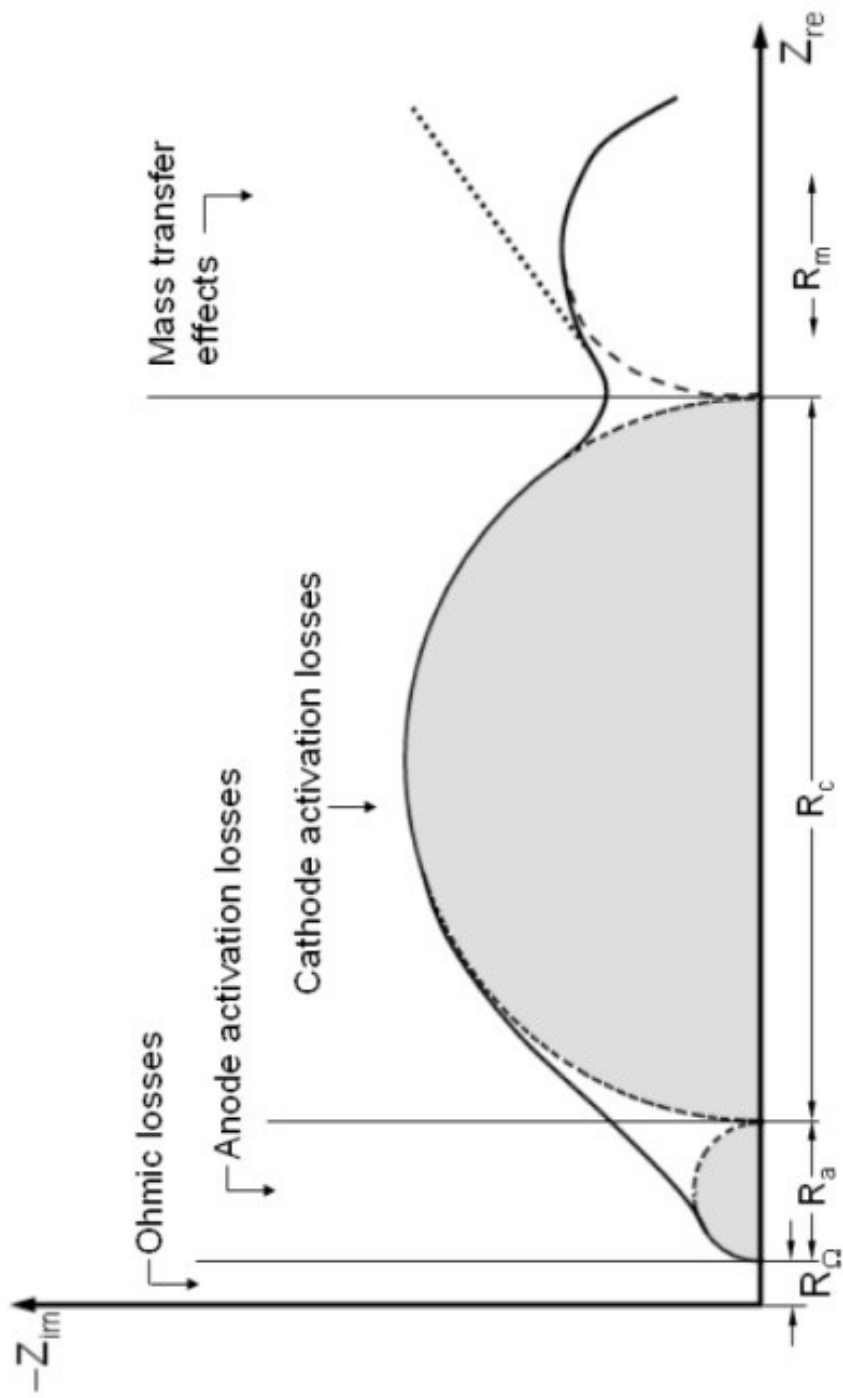
Figure 2.8. Nyquist plot of a typical EC model for batteries and fuel cells [33].

Reference

[1] H.H. Wang, H. Li, X.Z. Yuan, PEM Fuel Cell Diagnostic Tools, Taylor & Francis Group, 2011.

[2] W.J. Wruck, R.M. Machado, T.W. Chapman, Journal of the Electrochemical Society, 134 (1987) 539-546.

[3] C. Lagergren, G. Lindbergh, D. Simonsson, Journal of the Electrochemical Society, 142 (1995) 787-797.

[4] M. Liu, J.H. Wang, S.B. Wang, X.F. Xie, T. Zhou, V.K. Mathur, Chinese Journal of Chemical Engineering, 18 (2010) 843-847.

[5] Y.C. Park, D.H. Peck, S.K. Kim, S. Lim, D.H. Jung, J.H. Jang, D.Y. Lee, Journal of Power Sources, 195 (2010) 4080-4089.

[6] F.N. Buchi, A. Marek, G.G. Scherer, Journal of the Electrochemical Society, 142 (1995) 1895-1901.

[7] T. Mennola, M. Mikkola, M. Noponen, T. Hottinen, P. Lund, Journal of Power Sources, 112 (2002) 261-272.

[8] M.A. Rubio, A. Urquia, S. Dormido, Journal of Power Sources, 171 (2007) 670-677.

[9] Y. Zhu, W.H. Zhu, B.J. Tatarchuk, In-Situ Dynamic Characterization of Energy Storage and Conversion Systems, in: A. Zobaa (Ed.) Energy Storage - Technologies and Applications, InTech, 2013.

[10] H.J. Bergveld, W.S. Kruijt, P.H.L. Notten, Battery Management Systems: Design by Modelling, Springer, 2002.

[11] O. Heaviside, The Induction of Currents in Cores, in: Electrical Papers, Macmillan and Co., New York, 1894, pp. 353-415.

[12] O. Heaviside, Electromagnetic Induction and Its Propagation (2nd Half), in: Electrical Papers, Macmillan and Co., New York, 1894, pp. 39-154.

[13] H.P. Hall, A History of Impedance Measurement, in: IET Labs, Inc. Available at : http://www.ietlabs.com/genrad_history/papers_application_notes/.

[14] A.E. Kennelly, in: The 76th meeting of the American Institute of Electrical Engineers, New York, 1893, pp. 172-232.

[15] M.E. Orazem, B. Tribollet, Electrochemical Impedance Spectroscopy, John Wiley & Sons, Inc., Hoboken, New Jersey, 2008.

[16] J.R. Macdonald, Annals of Biomedical Engineering, 20 (1992) 289-305.

[17] R. O'Hayre, S.-W. Cha, W. Colella, F.B. Prinz, Fuel Cell Fundamentals, John Wiley & Sons, New York, Hoboken, New Jersey, 2006.

[18] E. Barsoukov, J.R. Macdonald, Impedance Spectroscopy: Theory, Experiment, and Applications, Wiley-Interscience, 2005.

[19] W.H. Zhu, R.U. Payne, R.M. Nelms, B.J. Tatarchuk, Journal of Power Sources, 178 (2008) 197-206.

[20] P.T. Wojcik, P. Agarwal, M.E. Orazem, Electrochimica Acta, 41 (1996) 977-983.

[21] S.M. Shinners, Modern Control System Theory and Design, John Wiley & Sons, 1998.

[22] J.W. Hu, H.M. Zhang, L. Gang, Energy Conversion and Management, 49 (2008) 1019-1027.

[23] D.D. Macdonald, M. Urquidimacdonald, Journal of the Electrochemical Society, 132 (1985) 2316-2319.

[24] B.A. Boukamp, Journal of the Electrochemical Society, 142 (1995) 1885-1894.

[25] J.R. Macdonald, Electrochimica Acta, 35 (1990) 1483-1492.

[26] B.A. Boukamp, Solid State Ionics, 20 (1986) 31-44.

[27] D. Vladikova, in: International Workshop "Advanced Techniques for Energy Sources Investigation and Testing", Sofia, Bulgaria, 2004.

[28] A.J. Bard, L.R. Faulkner, Electrochemical Methods: Fundamentals and Applications, Wiley, 2001.

[29] Research Solutions & Resources LLC. Electrochemistry Resources: Electrochemical Impedance: Diffusion and EIS: Warburg. Available at: http://consultrsr.com/resources/eis/diffusion.htm.

[30] R.U. Payne, Y. Zhu, W.H. Zhu, M.S. Timper, S. Elangovan, B.J. Tatarchuk, International Journal of Electrochemistry, 2011 (2011).

[31] A. Parthasarathy, S. Srinivasan, A.J. Appleby, C.R. Martin, Journal of the Electrochemical Society, 139 (1992) 2530-2537.

[32] C. Gabrielli, Identification of Electrochemical Processes by Frequency Response Analysis, in: Solatron Analytical AMETEK, Inc. 1998; Technical Report No. 004/83.

[33] W.H. Zhu, R.U. Payne, B.J. Tatarchuk, Journal of Power Sources, 168 (2007) 211-217.

Chapter 3

EIS Application to Proton Exchange Membrane Fuel Cells

Stack Characterization and Performance Comparison between High
Temperature and Traditional Proton Exchange Membrane Fuel Cell Stacks

3.1. Introduction

This chapter is submitted to Journal of Power Sources as a journal article. In order to keep the consistency of this dissertation and avoid content duplication to Chapter 1, the introduction and backgrounds of the journal article are not included here. Instead, a brief review on EIS applications to HT-PEM fuel cells and PA-PBI membranes will be presented in this section.

The work in this chapter highlights the advantages of EIS technique and EC simulation in their application to dynamic characterization and evaluation of proton exchange membrane (PEM) fuel cell systems. Both stacks are manufactured based on current PEM technologies at commercial level. The comparison of stack characterization reveals the advantages of the HT-PEM fuel cell stack over the traditional one as well as its immaturity in development. This work provides references for improvement of PEM fuel cells aiming at commercial applications. Based on the current research development, the insufficient experimental impedance data of HT-PEM fuel cell systems challenges the validation of proposed theories and mechanisms. The results of impedance spectra and EC simulation in this work also provide further experimental data for mechanism validation and stack diagnostics.

3.1.1. Impedance measurement of HT-PEM fuel cells

Compared to the impedance study of traditional PEM fuel cell systems, there have been only limited studies of EIS applications to high temperature PEM fuel cells. Impedance measurement was pioneered to study the electrical conductivity of PBI-based films at the end of 1990s. Fontanella and his co-workers [1] utilized impedance measurement to study the conductivity of PA doped PBI films at the temperatures below 100°C at a pressure up to 0.25 GPa. Soon after that, Bouchet and Siebert [2] published their work of measuring the conductivity of acid doped PBI films with the help of impedance measurement. However, in these works, impedance measurement was utilized only as an auxiliary method.

It had not been applied to a membrane electrode assembly (MEA) or a fully constructed PEM fuel cell based on a high temperature membrane until 2005. Xu [3] employed impedance analysis to study the effect of relative humidity (RH) on oxygen reduction reaction (ORR) kinetics for a high temperature PEM fuel cell manufactured from Nafion-Teflon-phosphotungstic acid (NTPA) membranes. Almost at the same time, Ramani [4] published their impedance measurement to a PEM fuel cell based on PA doped Nafion membrane at 120°C and 35% RH.

Several EIS studies on PA-PBI based HT-PEM fuel cells emerged from 2006 [5-9]. Jalani and his co-workers [5] published their impedance analysis of a single cell assembly, named Celtec®-P series 1000 MEA (BASF Fuel Cell). Qi and his group [9] applied EIS to study the performance and degradation of a PA-PBI based PEM fuel cell at 180°C with a load of 0.2 A cm^{-2}. But both of the group did not perform EC simulations of the cell impedance. At the same time, a more completed EIS application was published

by Jingwei Hu and his co-workers [6-8, 10], which included a series work of impedance measurement and analysis, EC simulations, and degradation tests of cell performance.

3.1.2. Current discussions on impedance analysis

The published applications of EIS on high temperature PEM fuel cells, although limited, present different measurement results one from another. Several different EC models have also been proposed to interpret measured impedance data. Ohmic resistances, introduced by cell components (electrodes, membranes, gas diffusion layers, and other supporting plates) and connections, and wiring inductions are involved in impedance analysis of all published works. Main differences exist in the analysis and interpretation of polarization impedance. Cells tested with different configurations and operating conditions may perform differently from each other, however, they should behave certain characteristics in common, especially, the cells configured the same type of membrane. Below, the EIS applications to high temperature PEM fuel cells based on PA doped PBI membranes will be summarized and discussed. The emphases are placed in the EC simulation and data interpretation.

So far, up to three arcs have been reported in Nyquist plots of measured impedance spectra. But these three arcs may not be well separated in all cases. One arc may overlap with its neighboring ones when they shift to a similar frequency range with the change of cell operating conditions. Or one arc may decrease to be negligible under some conditions. The processes involved in data interpretation mainly include charge transfer process, mass transfer process, and gas diffusion process. While, some groups observing two impedance arcs in Nyquist plot prefer to classify the impedance arcs as anodic and cathodic processes [11-16].

58

3.1.2.1.Ohmic resistance

Ohmic resistance (R_Ω) was reported as a set of scattered numbers with increasing current density in Jalani's work [5]; however, a trend of decline was still observable from those published data. Later, it was confirmed in many other experiments that R_Ω decreases with increasing current density [15, 17-20]. Following Zhang's theory [17], it has been accepted that the decrease of R_Ω is resulted from an increase in the proton conductivity of the membrane due to higher water productivity at higher current density. However, Zhang [17] also expected a constant level of R_Ω at a current density larger than 1.0 A cm^{-2} because of a constant water uptake of the membrane balanced between produced and purged water. This constant level was observed in Andreasen's experiments both on a 1 kW cell stack [16] and a single cell MEA [21] even at a current density lower than 1.0 A cm^{-2}.

The effect of operating temperature on R_Ω is more complicated than current density. And lots of attentions have been paid to it since the activation behavior closely relates to the proton conductivity mechanism of membranes. Some reported that R_Ω decreases with increasing temperature [15, 17, 21]. The proton hopping mechanism proposed by Bouchet [2, 22] was applied to explain this thermal effect [17]. But, inconsistent with these results, many other researchers reported an increase of R_Ω with increasing temperature when the temperature went higher than around 140ºC [11, 18, 20].

3.1.2.2.High frequency impedance arc

High frequency (HF) impedance arc appears right after the wiring inductive loop as frequency decreases in Nyquist plot. And generally it is quite a small semi-circle comparing to the following impedance arcs. It dominates the region of frequency from

above 100 Hz up to 1000 Hz [5, 16, 17, 19-21, 23], or even higher. The effects of temperature [17, 20] and current density [19, 20] on this impedance arc are observable but not as significant as on other impedance arcs dominating lower frequency regions. The resistance of this HF impedance arc decreases with increasing current densities, and its time constant decreases with increasing temperature. The latter can be observed in Nyquist plot as the impedance arc shifts toward higher frequency, or "shrinks". Kinetically, this phenomenon can be explained as the process occurring faster at higher temperature.

It has been validated and discussed in many published works that this HF impedance arc is contributed by charge transfer processes. Its impedance is generally simulated by the ($R_{ct}C_{dl}$) sub-circuit in EC models. The R_{ct} refers to charge transfer resistance and the C_{dl} refers to double-layer capacitance introduced by the charge accumulation and separation in the interface of electrode-electrolyte. In some cases, the double layer capacitor may be substituted by a CPE to reflect the non-ideal characteristics of the interface.

Many researchers preferred to ascribe this HF arc to the charge transfer process occurring on the anode, that is the charge transfer process involved in hydrogen oxidation reaction (HOR) [11, 15, 16, 18]. While some other groups stated that the charge transfer processes of both HOR and ORR contributed to this HF impedance arc but the contribution of HOR was negligible at low current density [17, 20].

3.1.2.3. Middle frequency impedance arc

Middle frequency (MF) impedance arc is contributed by the most dominating process occurring in the cell. It usually appears as the largest semi-circle in Nyquist plot and spans from 100 Hz to 1 Hz [5, 16, 17, 19-21, 23]. A consistent interpretation proposed for this arc has been almost accepted in all published cases that an activation process related to ORR contributes to this polarization loss.

In some cases, only one impedance arc was observed in Nyquist plot [6-8, 10, 24, 25]. This only arc should be explained as mass transfer impedance. Firstly, the LF arc does not perform significant contribution to the total impedance all the time (discussed later). Secondly, as mentioned in the discussion of HF arc, sometimes the HF arc may shrink to be hardly observable. In this case, the HF arc actually is merged by the MF arc and the total impedance appears as one arc.

3.1.2.4. Low frequency impedance arc

Low frequency (LF) impedance arc only appears in some certain cases when the contributions of concentration processes to cell impedance are comparably significant. Generally, it dominates frequency region below 1 Hz to around 0.1 Hz [5, 16, 17, 19-21, 23]. The impedance of this arc strongly depends on the composition of cathode gas, which is generally air, oxygen, or a mixture of them. Besides, the LF arc enlarges with the increase of current loads and may dominate the total impedance at high current loads instead of MF arc. Studies on oxygen stoichiometry can provided further information for the study of diffusion processes.

3.2. Experimental details

3.2.1. HT-PEM fuel cell stack

The commercial HT-PEM fuel cell stack module (Serenus 166Air C Fuel Cell Evaluation Kit, Serenergy Inc.) under research is featured by PA-PBI membranes. The active area of the membrane electrode assembly (MEA) is about 45 cm^2. The whole stack consists of 65 planar single cells, that is 66 electrode plates. The nominal power at its beginning of life (BOL) is about 1 kW. The stack is capable to be operated in the temperature range between 100°C and 175°C, with an optimum at 160°C. It can be fueled not only with pure hydrogen (H_2) but reformate gases.

Pure H_2 was supplied to the anode during impedance measurement. Ambient air was supplied through a blower to the cathode. A purge valve (Bürkert 6011, 2/2-way Miniature Solenoid Valve) was installed at the fuel outlet to provide a dead-end anode configuration. The pressure of the stack system was stable at 45 mbar (0.6527 psig) by a proportional valve (Bürkert 2835, 2/2-way proportional valve) installed at the H_2 inlet. The valve was controlled by a digital controller (Bürkert 8611, eControl) and a pressure sensor (Bürkert 8314, pressure transmitter) by feedback mechanism. An illustration of the experimental configuration is shown in Figure 3.1. The bold black solid lines indicate the electric circuit connections. And the thin black solid lines refers to signal channels for data communication.

EIS measurement was conducted by Gamry FC350^{TM} fuel cell monitor (Gamry Instruments), in conjunction with TDI-Dynaload$^®$ RBL488 programmable load. A LabVIEW (National Instruments) based program, called Embedded Fuel Cell Control Unit (EFCU) (Serenergy Inc.) was installed to monitor the module status during its
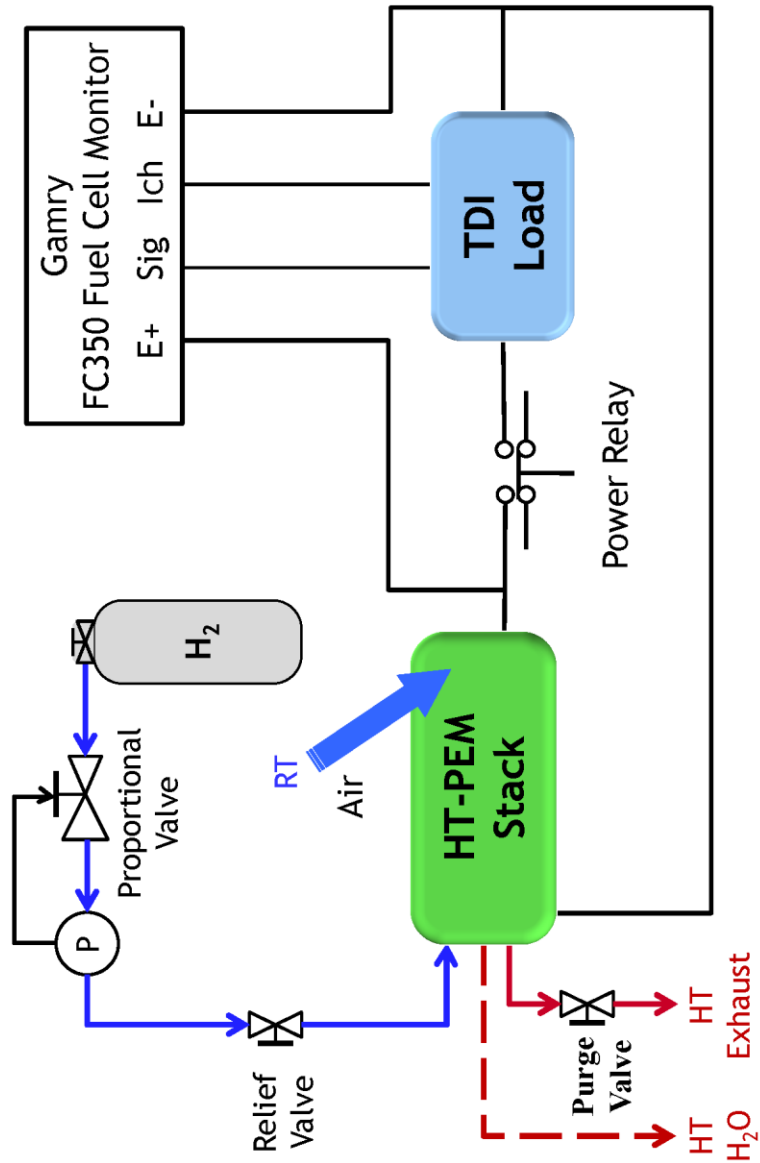
Figure 3.1. Illustration of the electrical configuration for obtaining impedance data from the HT-PEM fuel cell stack. A fuel cell monitor (Gamry Instruments) and a current load (TDI-Dynaload) are connected to this measuring circuit. Solid arrows refer to gas inlet and outlet of the anode. Dashed arrow refers to water outlet of the cathode. Bold lines refer to electrical connections, and thin lines refer to signal channels.

operation. A set of impedance data of the whole stack module (including the blower, heater, bleeder resistors, sensors, and other electronic devices embedded in the system) was measured during cell operation. The operating temperature was set at 160°C. A *dc* current of 4.5 A, 9 A, 12 A, 13.5 A, and 15 A, corresponding to the current density of 100 mA cm^{-2}, 200 mA cm^{-2}, 267 mA cm^{-2}, 300 mA cm^{-2}, and 333 mA cm^{-2}, was loaded to the stack from low to high. The frequency swept from 10 kHz to 0.1 Hz at a rate of 10 points per decade under each current load setting.

3.2.2. Traditional PEM fuel cell stack

The traditional PEM fuel cell stack module, named Nexa^{TM} fuel cell system (Ballard Power Systems Inc.), was studied by EIS measurement [26, 27]. Nexa system is a 47-cell stack module with an unregulated *dc* power of 1.2 kW. Its output current can reach 44 A. The stack voltage normally rises up to 41 V at open circuit and 26 V at full load. The fuel cell geometric working area is estimated as *ca.* 122 cm^2 due to the inexistence of manufacturing data [26]. The automated operation is maintained by an embedded controller board. H$_2$ was supplied to the stack anode at 5.0 psig, and air was supplied through a blower to the stack cathode at 2.2 psig.

An experimental configuration similar to the one used for HT-PEM fuel cell stack (Figure 3.1) was employed to obtain the impedance data of the Nexa stack. Gamry FC350^{TM} fuel cell monitor in conjunction with TDI-Dynaload$^{®}$ RBL488 programmable load was utilized to measure the stack impedance. The *dc* current load was set at 12.2 A, 24.4 A, and 32.5 A, from low to high, corresponding to a current density of 100 mA cm^{-2}, 200 mA cm^{-2}, and 267 mA cm^{-2} that is consistent with the load condition of the HT-PEM system. The measuring frequency swept from 10 kHz to 0.01 Hz. The operating

temperature of the Nexa stack module was automatically stabilized between 40ºC and 65ºC.

3.3. Results and discussion

3.3.1. Impedance spectra of HT-PEM fuel cell stack

Five impedance spectra of the HT-PEM fuel cell stack module measured under different current loads are plotted together in one Nyquist plot (Figure 3.2). The operating temperature is set at 160ºC. As the current increases from 100 mA cm^{-2} to 333 mA cm^{-2}, a decrease of total stack impedance is observed. It is mainly contributed by the decrease of the impedance arcs dominating the frequency range lower than 100 Hz. The smaller intercept of the spectra and the real axis (the one closer to the origin of Nyquist plot, measured at the frequency above 1000 Hz) almost keeps constant at around 15 Ω cm^2 despite the change of the stack load. But the larger intercept of the spectra and the real axis (the one further from the origin of Nyquist plot, measured at the frequency point lower than 1 Hz) decreases significantly from approximately 70 Ω cm^2 to 40 Ω cm^2 with increasing current density. No significant change of the impedance arc dominating high frequency range can be observed from Figure 3.2. High frequency inductive impedance also keeps at a steady status with the change of the stack load.

3.3.2. EC simulation of HT-PEM fuel cell stack

3.3.2.1.EC model for simulation

Due to limited researches on HT-PEM fuel cells, no general consensus has been achieved on its EC simulation, neither the EC models nor the physical explanations of EC elements. The impedance arcs contributed by different activation and concentration processes overlap with each other to a different extent under different operating
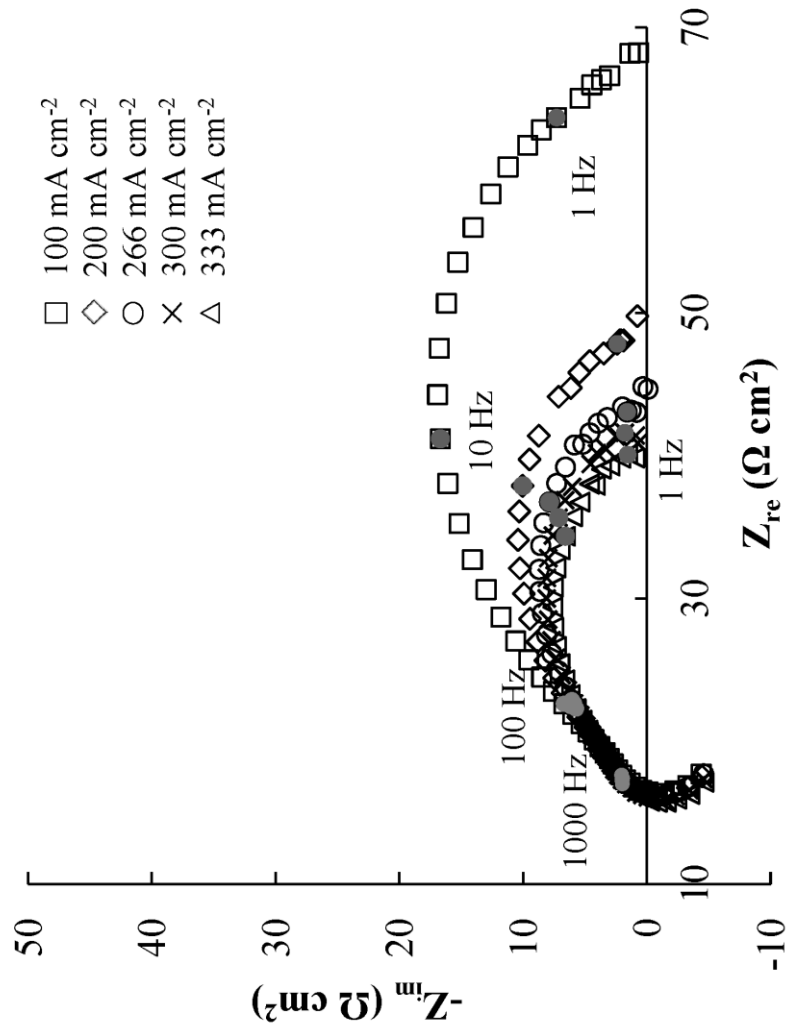
Figure 3.2. Impedance spectra of the HT-PEM fuel cell stack measured at a current density of (□) 100 mA cm^{-2}, (◇) 200 mA cm^{-2}, (○) 267 mA cm^{-2}, (×) 300 mA cm^{-2}, and (△) 333 mA cm^{-2}. The impedance data at frequency of 1000 Hz, 100 Hz, 10 Hz, and 1 Hz of each spectra are marked with solid dots. The operating temperature is set at 160°C. Pure H$_2$ is supplied to the stack anode at around 45 mbar and ambient temperature. Ambient air is taken into the stack cathode by the blower.

conditions. The generated impedance spectra significantly differ from one another. In this work, a three time constant non-ideal EC model (Figure 3.3) is proposed to simulate the HT-PEM fuel cell stack. It consists of one pure resistor R_Ω, one paralleled (C_aR_a) sub-circuit, one paralleled (Q_cR_c) sub-circuit, one finite diffusion element (FDE) O, and one wiring inductance L. In this EC model, one constant phase element (CPE) Q_c is used to replace the ideal capacitor and reflect the non-ideality of cathode processes caused by the inhomogeneous characterization of the electrode surface. The detail explanations are presented in the following section of EC interpretation.

The impedance spectrum measured at a *dc* current load of 9 A (200 mA cm^{-2}) is simulated by the non-ideal EC model (Figure 3.3). The measured data and its fitting curve are shown in Figure 3.4. The smaller intercept on the real axis refers to the ohmic resistance (R_Ω) of the stack module. The difference between two intercepts on the real axis refers to the polarization resistance (R_p) of the stack, which is a combined contribution of activation and concentration processes. The small capacitive arc dominating the high frequency region is simulated by the paralleled (C_aR_a) sub-circuit. This arc has a summit frequency at about 680 Hz. The depressed large capacitive impedance arc spanning over the rest frequency region is simulated as two overlapped capacitive arcs. The middle frequency arc, which has a summit frequency around 20 Hz, is simulated by the paralleled (Q_cR_c) sub-circuit. This impedance arc is much larger than others and dominates the stack impedance. The low frequency arc is simulated by the diffusion element and gives very limited contribution to the stack impedance under its operating condition. The proposed non-ideal EC model is then validated by simulating the impedance spectra measured under other load conditions (Figure 3.5). The simulating
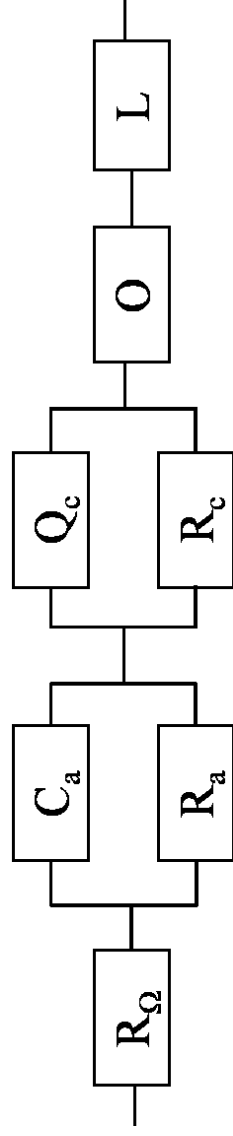
Figure 3.3. The non-ideal EC model proposed to simulate the HT-PEM fuel cell stack.
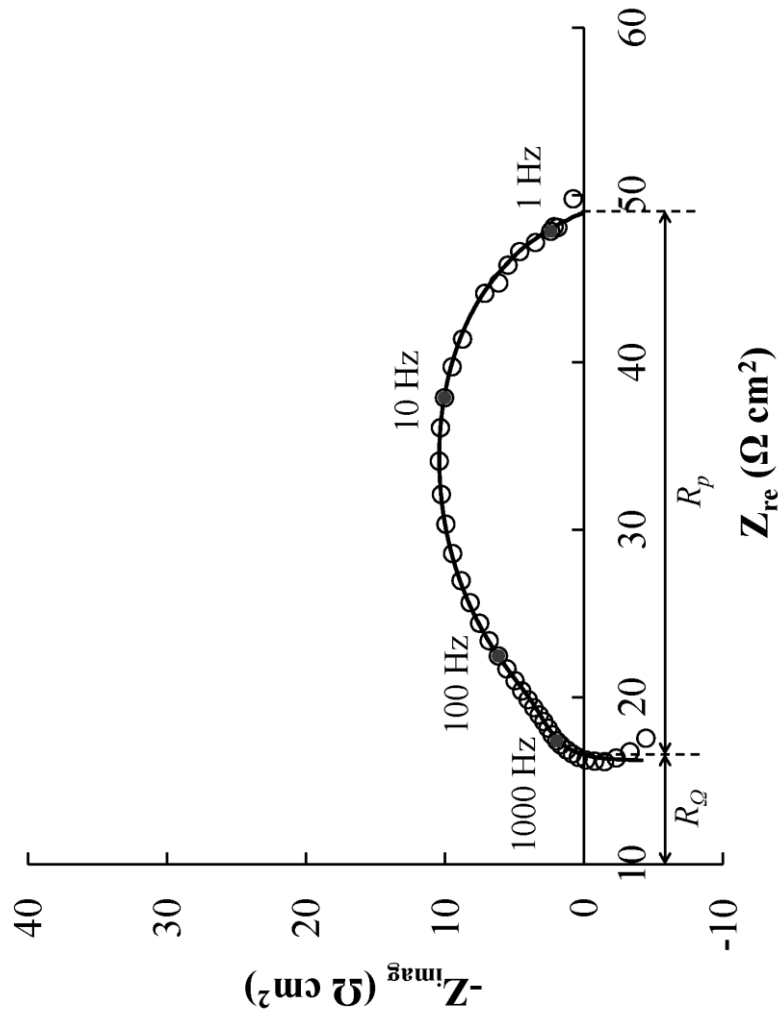
Figure 3.4. The impedance spectrum of the HT-PEM fuel cell stack measured under a current load of 9 A (200 mA cm^{-2}). The impedance data measured at frequency of 1000 Hz, 100 Hz, 10 Hz, and 1 Hz are marked with solid dots (●). The operating temperature is set at 160°C. The fitting curve is simulated by the non-ideal EC model (Figure 3.3). Pure H$_2$ is supplied to the stack anode at around 45 mbar and ambient temperature. Ambient air was taken into the stack cathode by the blower.
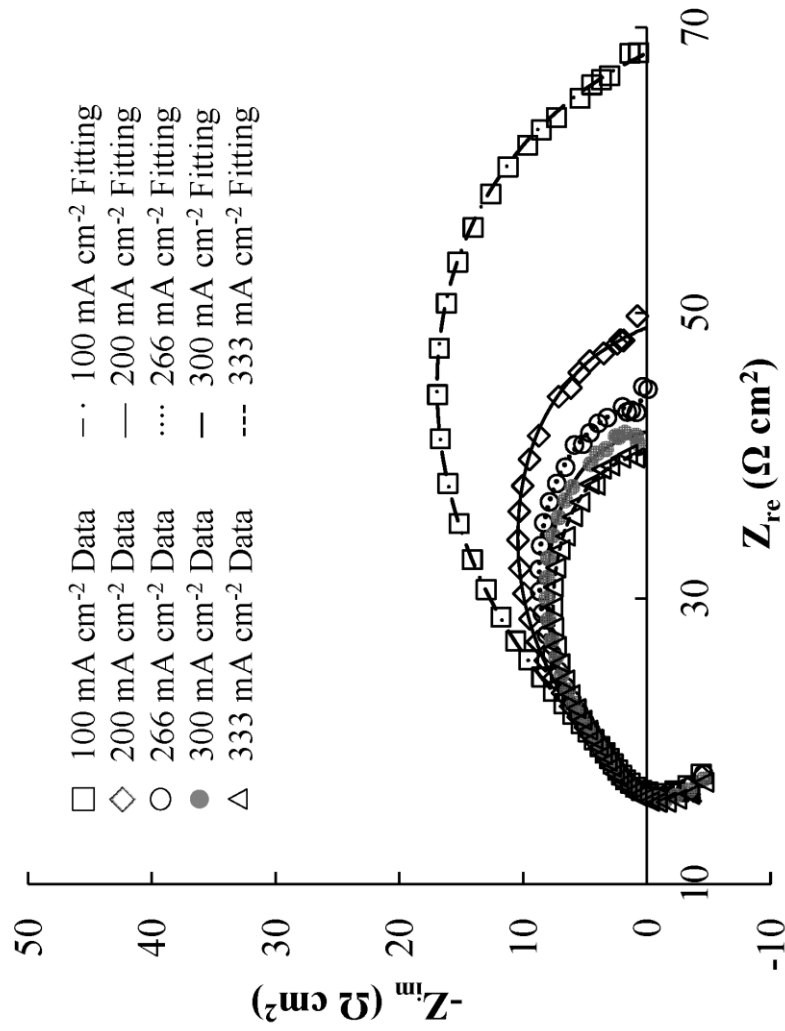
Figure 3.5. The impedance spectra of the HT-PEM fuel cell stack measured under various current loads. The operating temperature is set at 160°C. The fitting curves are simulated by the non-ideal EC model (Figure 3.3). Pure H_2 is supplied to the stack anode at around 45 mbar and ambient temperature. Ambient air is taken into the stack cathode by the blower.

curves show great goodness of fit with the changing current density. The fitting values of each EC elements and their changes with current loads are analyzed below to perform EC element interpretation.

3.3.2.2.EC element interpretation

3.3.2.2.1. Ohmic resistance

The ohmic loss refers to pure resistive loss and can be simulated by an ideal resistor R_Ω. It consists of resistances contributed by membranes, electrodes, catalyst layers, gas diffusion layers, component connections, and any other hardware connected to the measuring system, such as wires, heaters, blowers, and controller boards. However, it is difficult to discriminate their impedance one from another. The variation of ohmic loss with changing current load reflects the change of proton conductivity of the membranes.

a. Proton conductivity mechanism

The mechanism of proton conductivity changes with PA doping level. Generally, PA is doped onto the PBI backbone in two different manners. As far as the doping level is lower than two molecules of PA per repeat unit of PBI [28] the acids are stably linked to the PBI structure by H bonding. The conductivity at low PA doping level comes from a cooperative movement of two protons along the polymer-PA anion chain [2], that is one proton hopping away from an acid anion to form a N-H bond with the polymer and this anion accepting the proton hopping from another N-H bond at the same time. This type of proton migration provides great contribution to membrane conductivity but is not enough for fuel cell applications. Experimental data [29] supported that the conductivity of PA doped PBI significantly increases with an increasing doping level of PA when more than two molecules of PA per repeat unit of PBI are doped. Other than the PA molecular

bounded to PBI by H bonding, the rest of doped PA molecular form $H_2PO_4^-$ by self-ionization and self-dehydration [30]:

$$5H_3PO_4 \rightleftharpoons 2H_4PO_4^+ + H_3O^+ + H_2PO_4^- + H_2P_2O_7^{2-} \qquad (3.1)$$
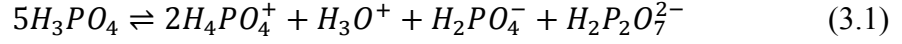
The proton conduction is described as a proton hopping mechanism along the anionic chains of $H_2PO_4^-$ / HPO_4^{2-} [30]. This mechanism provides the main attributions to proton conductivity and significantly increase the conductivity of PA-PBI membranes to met the requirement of EC application.

In PA-PBI system, water is no longer the essential contributor to proton conductivity. This feature enables fuel cell operations above 100ºC. However, the presence of water still have non-negligible effects on proton conductivity of PA-PBI membranes. Additional hydron carriers can be formed by dissociating acid molecular in water [30] and increase the proton conductivity.

$$H_3PO_4 + H_2O \rightleftharpoons H_3O^+ + H_2PO_4^- \qquad (3.2)$$
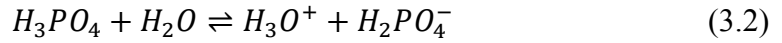
The situation changes when the content of water continuously increases. The reducing concentration of charge carriers due to excessive water content leads to a decrease of conductivity.

b. Dependence on current density

Our experimental data (Figure 3.5) and simulation results (Figure 3.6 and 3.7) present a relevant stable value of ohmic resistance (R_Ω) when the current density is lower than 267 mA cm^{-2}. However, it slightly decreases when the current density increases from 267 mA cm^{-2} to 333 mA cm^{-2}. A decrease of ohmic resistance with increasing current density was reported [15, 18, 19], but Zhang [17] also reported a stable ohmic resistance with the change of current when the current density went over 1.0 A cm^{-2}. The
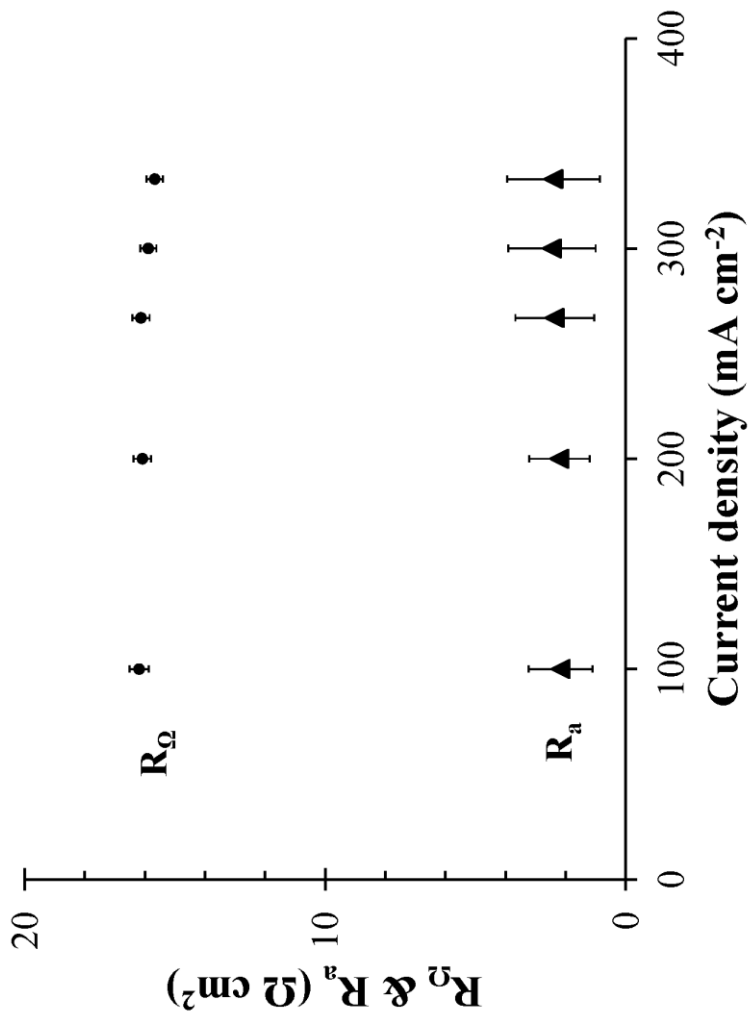
Figure 3.6. The dependence of stack ohmic resistance (R_Ω) and anode activation resistance of HOR process (R_a) on current density. The values are simulated by the non-ideal EC model (Figure 3.3) from the impedance spectra of HT-PEM fuel cell stack measured at an operating temperature of 160°C and changing current density.
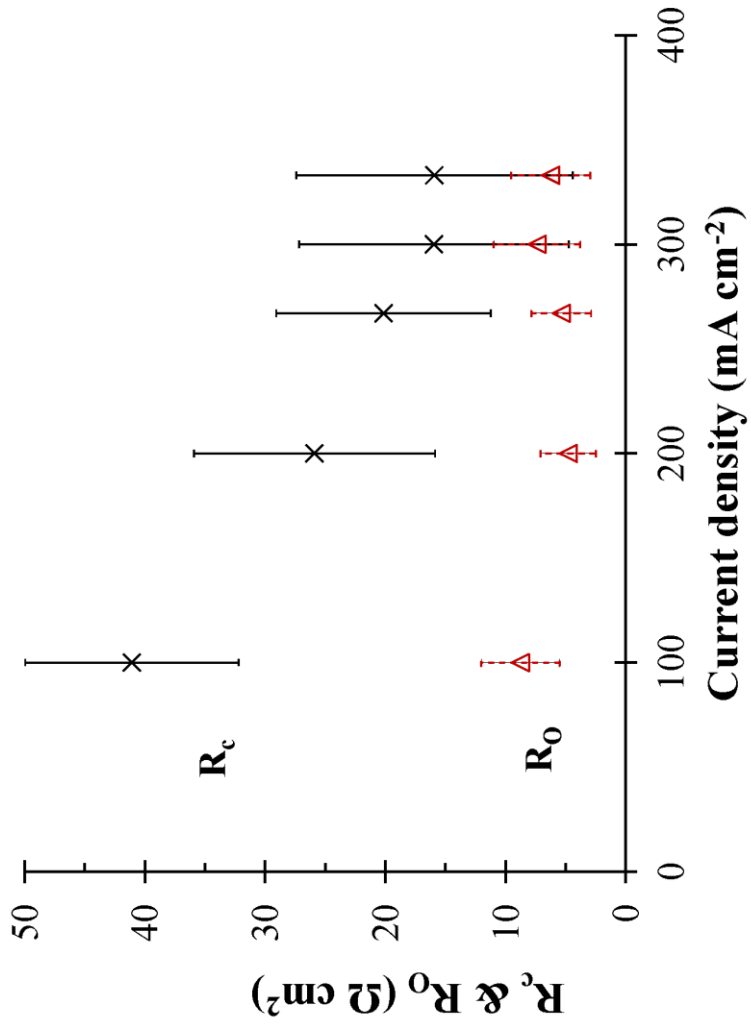
Figure 3.7. The dependence of stack cathode activation resistance of ORR process (R_c) and the equivalent diffusion resistance R_O calculated from Eq. 3.5. The values are simulated from the impedance spectra of HT-PEM fuel cell stack at an operating temperature of 160°C and changing current density.

conductivity following the hopping mechanism changes with temperature and membrane water content. It is theoretically independent on current load. The stable value of R_Ω at low current densities represents a stable conduction process throughout the current density range below 267 mA cm^{-2}. More water is produced under higher current loads. When the current density increases to over 267 mA cm^{-2}, water content of MEAs slightly increases due to the disequilibrium between produced water and purged water. Thus, the slight decrease of R_Ω at higher current loads is observed because the small amount of water increases the proton conductivity.

3.3.2.2.2. Anode electrode

The electrode process occurring on the anode of a hydrogen-oxygen (H_2-O_2) fuel cell is hydrogen oxidation reaction (HOR). It has been widely accepted that the rate determine step (RDS) of HOR is the transfer process of electrons from the absorbed hydrogen atoms to the electrode [31]:

$$M \cdots H \rightleftharpoons (M + e^-) + H^+ \qquad (3.3)$$

HOR kinetics is much faster than oxygen reduction reaction (ORR) kinetics and other cell processes. When the frequency sweeps from high to low values, the impedance arc of HOR charge transfer process appears right after the wiring inductive loop. It usually behaves as a semi-circle much smaller than other impedance arcs. A dominating frequency range from about 100 Hz up to 1000 Hz or even higher [5, 11, 15, 17-19, 23] was reported for this process. Following this theory, the (C_aR_a) sub-circuit in the proposed EC model (Figure 3.3) is employed to simulate the charge transfer process occurring over anode / electrolyte interface. R_a refers to the resistance of transfer process of electrons (Eq. 3.3) occurring on anode electrode. C_a refers to the double-layer

75

capacitance caused by the charge accumulation and separation in the interface of anode and electrolyte. The kinetics of HOR process is so fast that no significant effect of current density is expected on HOR, especially when the cell is operated under low current densities. As shown in Figure 3.6, the charge transfer resistance of HOR (R_a) keeps at a stable value with the change of current load.

3.3.2.2.3. Cathode electrode

The electrode process occurring on the cathode of H_2-O_2 fuel cells is ORR. Its kinetics is very sluggish comparing to HOR process. The impedance of ORR process usually dominates the performance of total cell systems. No consensus has been reached after decades of study on ORR mechanism. The main controversy lies between whether the charge transfer process of ORR is the RDS [32] or the adsorption process of oxygen molecular on catalyst surface is the RDS [33]. The generally accepted mechanism for PEM fuel cell application considers the charge transfer process as the RDS of ORR process but with a change of Tafel slope at higher overpotential [32].

The large capacitive impedance arcs spanning over hundreds of hertz down to several hertz (Figure 3.2) is ascribed to the activation process of ORR. Its behavior and dominating frequency range obtained in this work keep consistency with the results of other published cases of HT-PEM impedance study [5, 17, 19, 23]. In this work, the sub-circuit (Q_cR_c) in the proposed EC model (Figure 3.3) is used to simulate the activation process of ORR. The ORR activation resistance R_c drops about 25 Ω cm^2 when the current density increases from 100 mA cm^{-2} to 300 mA cm^{-2} (Figure 3.7). The electrons accelerate at higher current density, which enhance the charge transfer process and lower the impedance of ORR process. However, the dependence of R_c on current density

76

changes when the current density increases to more than 300 mA cm^{-2}. It keeps at a stable value when the current density increase from 300 mA cm^{-2} to 333 mA cm^{-2} (Figure 3.7). The RDS of ORR process changes in this current density range when the adsorption of oxygen molecular on catalyst surface gradually lags behind the charge transfer process. This explanation could be further validated by continuously measuring cell impedance at even higher current densities.

3.3.2.2.4. Finite diffusion process

The impedance arc dominating the frequency lower than 1 Hz mostly merges with the ORR activation impedance arc. Only a small tail following the ORR impedance arc can be observed from the Nyquist plot (Figure 3.2). The low frequency impedance arc is contributed by the diffusion process of O$_2$ to the cathode electrode. The finite diffusion element (FDE) O is employed in the non-ideal EC model to simulate the low frequency diffusion process. The two simulating parameters of FDE are B and $Y_{o,0}$.

B is the time constant parameter in the unit of sec$^{1/2}$. It reflects the rate of diffusion process. The value of B slightly decreases with the increase of current density, but approaches to a stable level at high current density (Figure 3.8). The increase of current load does not fasten the diffusion process to a significant degree.

$Y_{o,0}$ is the magnitude of FDE admittance at $\omega = 1$ rad s^{-1}, in the unit of S sec$^{1/2}$, which is the reciprocal of Ω sec$^{-1/2}$. Its magnitude is defined based on the model of Warburg element, as [34]:

$$Y_{O,0} = \frac{n^2 F^2 A}{R_{ig} T} \left(\frac{1}{D_O^{1/2} C_O^*} + \frac{1}{D_R^{1/2} C_R^*} \right)^{-1} \tag{3.4}$$

77
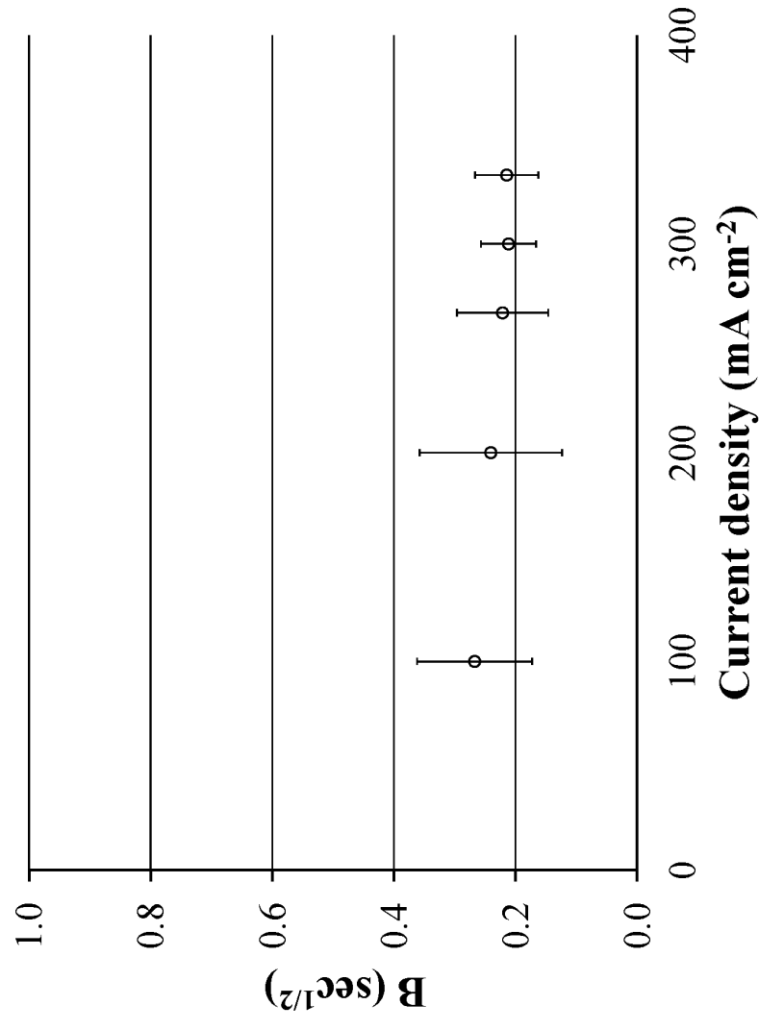
Figure 3.8. The values of the time constant parameter of FDE (B, in the unit of $sec^{1/2}$) simulated from the impedance spectra of HT-PEM fuel cell stack at an operating temperature of 160°C and changing current density.

where, n is the stoichiometric number of electrons involved in the reduction reaction; F is the Faraday constant; R_{ig} is the ideal gas constant; D_O and D_R are diffusivity of oxidized species and reduced species, respectively; and $C_O{}^*$ and $C_R{}^*$ are their bulk concentrations, respectively. R_O is the impedance of FDE [35] calculated at $\omega = 0$, equivalent to the value of R in an paralleled (CR) circuit:

$$R_O = Z_O(\omega = 0) = \lim_{\omega \to 0} \frac{tanh(B\sqrt{j\omega})}{Y_{0,0}\sqrt{j\omega}} = \lim_{\omega \to 0} \frac{B\sqrt{j\omega}}{Y_{0,0}\sqrt{j\omega}} = \frac{B}{Y_{0,0}} \quad (3.5)$$

Ambient air is fed to the cathode as the source of O_2. As the ORR process is enhanced at higher current density, the concentration of O_2 decreases and fails to keep at the constant level due to a faster consumption by the ORR process. The diffusion process of O_2 to the cathode lags behind the electrode reaction at higher current densities and gives large impedance to the stack performance. When the current density increases to higher than 300 mA cm^{-2}, the RDS of ORR process on the cathode changes. The adsorption of oxygen molecular dominates the electrode process, which relieves the lag of O_2 diffusion to the electrode. The explanation can be further validated by operating the HT-PEM fuel cell stack with pure O_2 supplement at varying oxygen stoichiometry.

The impedance arc of diffusion process in the HT-PEM fuel cell system is overlapped by the ORR impedance arc to a large extent. And the diffusion resistance is much smaller than the ORR resistance (Figure 3.7). Thus, the diffusion process does not have dominating limitation to the stack performance of HT-PEM fuel cell under the operating condition during impedance measurement.

3.3.3. EC simulation of traditional PEM

One widely accepted interpretation of PEM fuel cell impedance is to separate the polarization impedance according to anodic and cathodic processes. Following this idea, an ideal EC model (Figure 3.9) consisting with one ohmic resistor, three (CR) sub-circuits, and one wiring inductor was used to simulate the Nexa^{TM} PEM fuel cell stacks in our previous work [27]. Three parallel (CR) sub-circuits were ascribed to anode HOR process (C_aR_a), cathode ORR process (C_cR_c), and cathode finite diffusion process ($C_{diff}R_{diff}$), respectively in sequence from high frequency to low frequency. The EC model with only ideal circuit elements was used to facilitate PSpice simulation.

The newly proposed non-ideal EC model (Figure 3.3) shows great fitness to the impedance spectra measured from the HT-PEM fuel cell stack. It inspires the idea that the non-ideal EC model can be used to simulate the traditional PEM fuel cell stack. As expected, its simulation result shows great consistency to the impedance spectra measured at 200 mA cm^{-2} (Figure 3.10). The small impedance arc simulated by the parallel (C_aR_a) appears in the frequency range larger than 100 Hz. It refers to the activation process of HOR on anode electrodes. The large impedance arcs spanning over from several Hertz up to 100 Hz is contributed by the activation process of ORR on cathode electrodes. For the HT-PEM fuel cell stack, ORR process is the RDS of the total stack performance. But for the traditional PEM fuel cell stack, a large impedance arc comes out in the frequency range below 1 Hz, giving equivalent contribution to the total stack impedance as ORR process. This arc is simulated as a finite diffusion process. The non-ideal EC model reflects the non-ideal characteristics of the electrodes and interfaces, and provide realistic interpretation to each impedance arc.
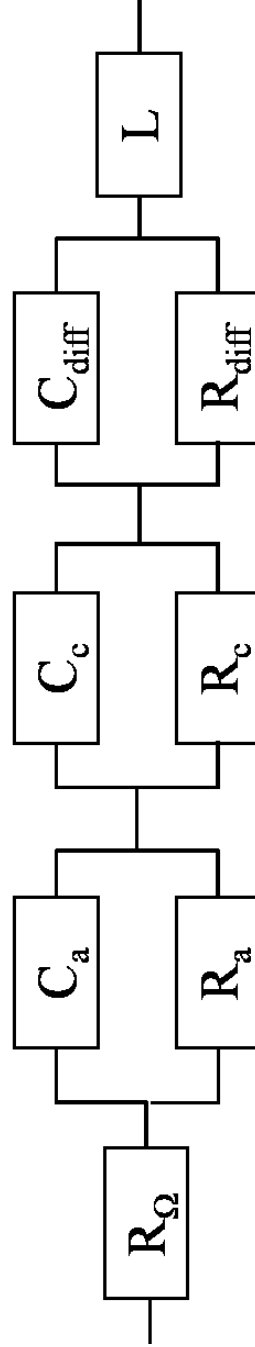
Figure 3.9. The ideal EC model with three time constants.
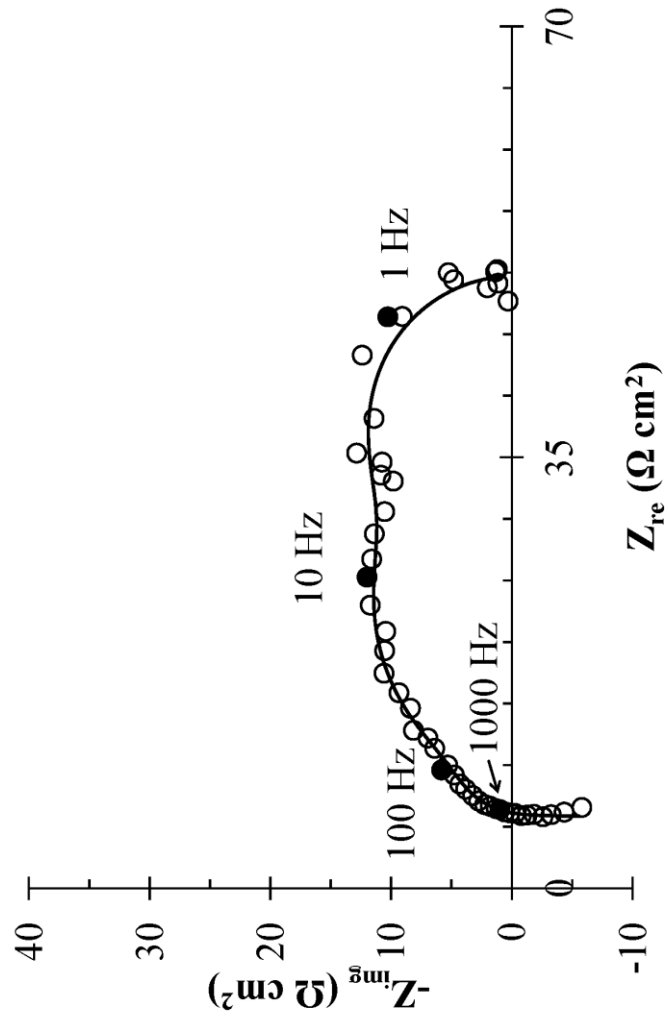
Figure 3.10. The impedance spectrum of the traditional PEM fuel cell stack (○) measured at a *dc* current of 24.4 A (200 mA cm^{-2}). The solid fitting curve is simulated from the non-ideal EC model (Figure 3.3). Pure H$_2$ and ambient air are supplied to the stack.

The impedance spectra of Nexa stack #751 measured under the current density of 100 mA cm^{-2}, 200 mA cm^{-2}, and 267 mA cm^{-2} are compared in Figure 3.11, along with their fitting curves simulated from the non-ideal EC model (Figure 3.3). The high frequency HOR impedance arc almost keeps stable with the increase of current density since the facile HOR does not have strong dependence on cell loads. The ORR impedance arc dominating middle frequency range significantly shrinks when the current density increases from 100 mA cm^{-2} to 200 mA cm^{-2}, but keeps almost unchanged when the current density continuously increases from 200 mA/cm^2 to 267 mA cm^{-2}. This similar behavior to the HT-PEM fuel cell stack can also be explained as a change of RDS. When the current density is low, the charge transfer process of ORR limits the cathode performance. An increase of current density promotes ORR process and decreases its impedance. When the current density increases to a certain level, the adsorption process of ORR lags behind the charge transfer process and limits the cathode behavior.

The significant change of diffusion impedance with increasing current density shows its great dependence on the stack load. According to Eq. 3.4 and Eq. 3.5, the diffusion resistance decreases when the current density changes from 100 mA cm^{-2} to 200 mA cm^{-2} (Figure 3.12). However, more reduced species is produced at higher current density. Due to the operating temperature of the traditional PEM fuel cell stack, the accumulation of liquid water inside the fuel cell at higher current densities brings challenge to the diffusion of O$_2$ to the cathode electrode. The diffusion of liquid water itself away from the electrode also contributes to the diffusion process. On the other side, the increased rate of O$_2$ consumption at higher current densities decreases the O$_2$ concentration in the
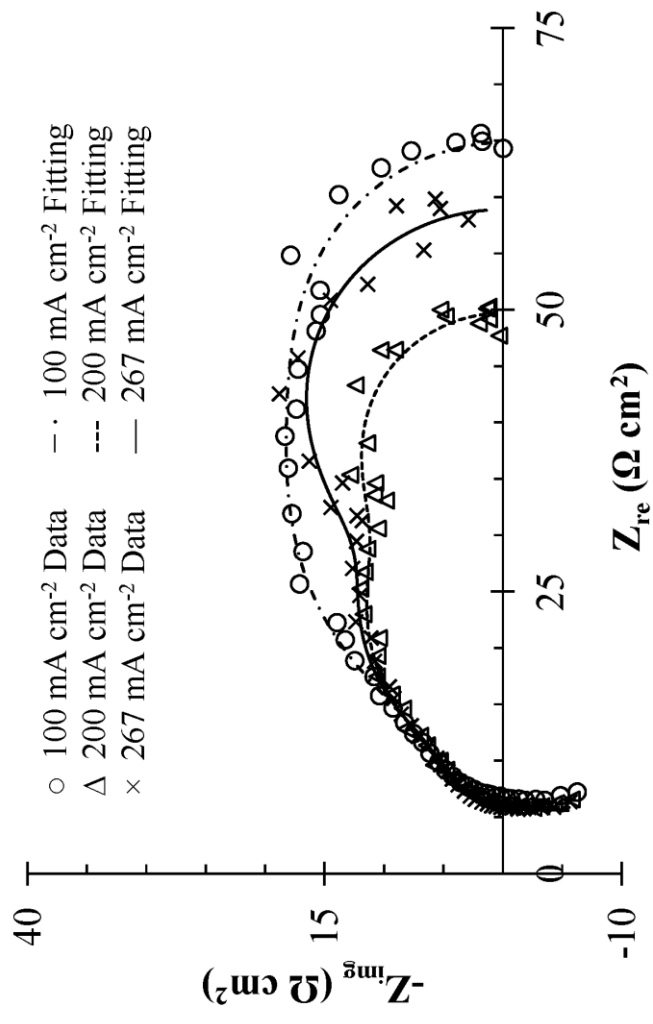
Figure 3.11. Stack impedance of the traditional PEM fuel cell measured at a current density of (○) 100 mA cm^{-2}, (△) 200 mA cm^{-2}, and (×) 267 mA cm^{-2}, along with their fitting curves simulated from the non-ideal EC model (Figure 3.3).
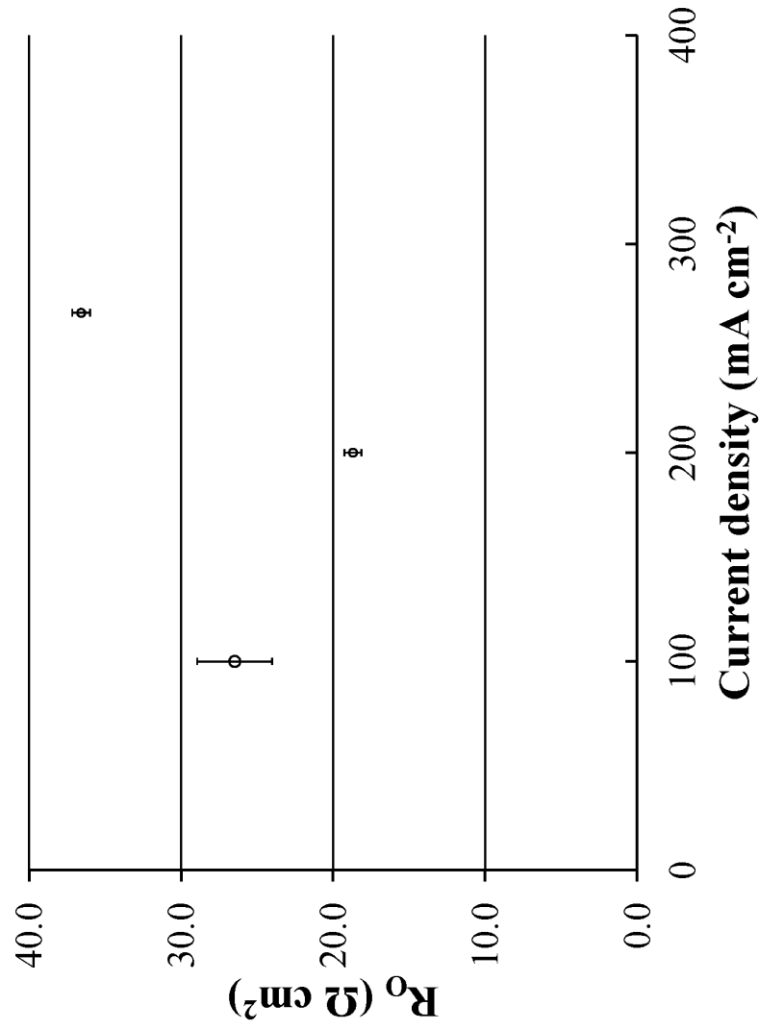
Figure 3.12. The values of the equivalent diffusion resistance R_O simulated from the impedance spectra of traditional PEM fuel cell stack under changing current density.

air supplement, which also gives more impedance to the diffusion process (Eq. 3.4 and Eq. 3.5).

3.3.4. Comparison between HT-PEM and traditional PEM

To facilitate the comparison between two types of PEM fuel cell, their impedance spectra are normalized to a comparable base, which is $\Omega \, cm^2$ per single planar cell (that is $\Omega \, cm^2 \, cell^{-1}$). This unit is based on the average output power density of each single cells inside the stack. Since the impedance spectra are measured from two commercial stack modules. It is difficult to separate the effects of stack control hardware from the effects of membranes and electrodes on ohmic resistances. The comparison between ohmic resistances of two modules cannot provide exact information for membrane comparison. Thus, the impedance spectra of two stacks are compared in the same Nyquist plot (Figure 3.13) after subtracting ohmic resistances. The values of ohmic resistances calculated from EC simulation are used here for subtraction.

The impedance difference between two PEM fuel cell stacks at high frequency range is small, especially under low current density. The HOR activation process on anode occurs so fast that the temperature dependence on its impedance is small. Its impedance slightly decreases when the operating temperature of the PEM fuel cell stack is elevated over 100°C. But the difference of cathode activation impedance between two stacks is significant. The ORR activation process presents much better performance at higher operating temperature. Since the cell performance is mainly dominated by ORR process, the enhancement of its activation provides great improvement of cell performance. The finite diffusion process at low frequency range also shows large differences under different operating temperatures. The diffusion impedance arc of the HT-PEM fuel cell
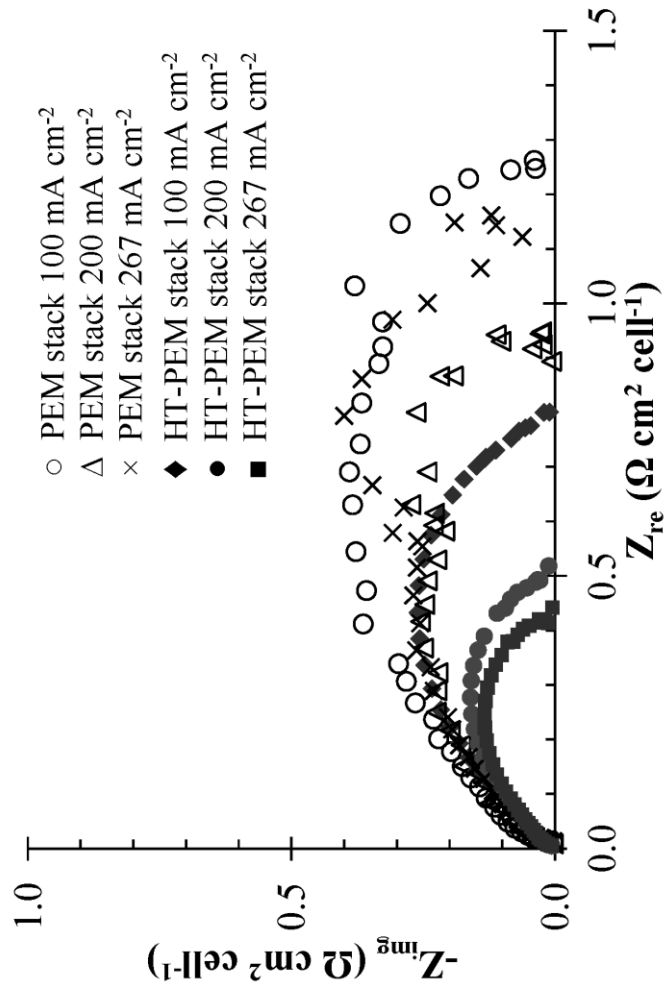
Figure 3.13. Impedance comparison between the traditional PEM fuel cell stack module and the HT-PEM fuel cell stack based on a normalized impedance in the unit of $\Omega \cdot cm^2$ per cell. Ohmic resistances are not included in the comparison.

stack is very small and mostly overlapped by the ORR impedance arc. But the traditional PEM fuel cell stack has a large diffusion impedance arc. At low current region, the diffusion impedance decreases with increasing current density. With the further increase of current density, the dependence of diffusion impedance changes. It increases with increasing current density due to the accumulation of liquid water inside the stack. This problem can be solved in the HT-PEM fuel cell systems with the single phase water environment. The higher operating temperature facilitates the water management inside the PEM fuel cells.

3.4. Conclusion

In this work, both a novel high temperature (HT) proton exchange membrane (PEM) fuel cell stack module operated at elevated temperatures around 160ºC and a traditional one operated at temperature between 40ºC and 65 ºC were studied by impedance measurement and equivalent circuit (EC) simulation. Both PEM fuel cell stacks were manufactured at commercial level. One non-ideal EC model was proposed to simulate the HT-PEM fuel cell stack. The excellent goodness of fit inspired the idea to simulate the traditional PEM fuel cell stack by this non-ideal EC model. Comparing to our previous simulation with ideal EC model [27], the use of one constant phase element (CPE) Q_c and one finite diffusion element (FDE) O enhanced the simulation of the oxygen reduction reaction (ORR) process and the diffusion process at middle and low frequency range.

Based on the EC simulation and impedance interpretation, the chemical and physical processes occurring in the HT and traditional PEM fuel cell stacks were similar. The hydrogen oxidation reaction (HOR) on anode had fast kinetics no matter the operating temperature is above or below 100°C. It contributed a small part to stack impedance. The

ORR process on cathode had sluggish kinetics and dominated the total stack impedance. However, the magnitude of ORR impedance arc in the HT-PEM fuel cell stack system was much smaller than in the traditional system due to the faster kinetics at higher temperature. The elevated operating temperature of HT-PEM fuel cell stack also facilitated the O_2 diffusion process and the water management inside the stack. Thus, the diffusion impedance was decreased to a magnificent degree.

The performance of two commercial PEM fuel cell stacks were compared by EIS technique and EC simulation at a normalized impedance level. Although the application of HT-PEM fuel cells is still in an immaturity stage, the significantly smaller polarization impedance of HT-PEM fuel cell stack gives a promising possibility to future development. This work highlights the ability of EIS and EC simulation in stack characterization and performance evaluation, and experimentally provides references for further study and diagnostics of commercial fuel cell stacks.

Reference

[1] J.J. Fontanella, M.C. Wintersgill, J.S. Wainright, R.F. Savinell, M. Litt, Electrochimica Acta, 43 (1998) 1289-1294.

[2] R. Bouchet, E. Siebert, Solid State Ionics, 118 (1999) 287-299.

[3] H. Xu, Y. Song, H.R. Kunz, J.M. Fenton, Journal of the Electrochemical Society, 152 (2005) A1828-A1836.

[4] V. Ramani, H.R. Kunz, J.M. Fenton, Journal of Power Sources, 152 (2005) 182-188.

[5] N.H. Jalani, M. Ramani, K. Ohlsson, S. Buelte, G. Pacifico, R. Pollard, R. Staudt, R. Datta, Journal of Power Sources, 160 (2006) 1096-1103.

[6] J.W. Hu, H.M. Zhang, J. Hu, Y.F. Zhai, B.L. Yi, Journal of Power Sources, 160 (2006) 1026-1034.

[7] J.W. Hu, H.M. Zhang, Y.F. Zhai, G. Liu, B.L. Yi, International Journal of Hydrogen Energy, 31 (2006) 1855-1862.

[8] J.W. Hu, H.M. Zhang, Y.F. Zhai, G. Liu, J. Hu, B.L. Yi, Electrochimica Acta, 52 (2006) 394-401.

[9] Z.G. Qi, S. Buelte, Journal of Power Sources, 161 (2006) 1126-1132.

[10] J.W. Hu, H.M. Zhang, L. Gang, Energy Conversion and Management, 49 (2008) 1019-1027.

[11] J. Lobato, P. Canizares, M.A. Rodrigo, J.J. Linares, Electrochimica Acta, 52 (2007) 3910-3920.

[12] J. Lobato, P. Canizares, M.A. Rodrigo, J.J. Linares, D. Ubeda, F.J. Pinar, Fuel Cells, 10 (2010) 312-319.

[13] J. Lobato, P. Canizares, M.A. Rodrigo, J.J. Linares, F.J. Pinar, International Journal of Hydrogen Energy, 35 (2010) 1347-1355.

[14] J. Lobato, P. Canizares, M.A. Rodrigo, F.J. Pinar, D. Ubeda, Journal of Power Sources, 196 (2011) 4209-4217.

[15] M. Boaventura, A. Mendes, International Journal of Hydrogen Energy, 35 (2010) 11649-11660.

[16] S.J. Andreasen, J.L. Jespersen, E. Schaltz, S.K. Kaer, Fuel Cells, 9 (2009) 463-473.

[17] J.L. Zhang, Y.H. Tang, C.J. Song, J.J. Zhang, Journal of Power Sources, 172 (2007) 163-171.

[18] C.Y. Chen, W.H. Lai, Journal of Power Sources, 195 (2010) 7152-7159.

[19] M. Mamlouk, K. Scott, Electrochimica Acta, 56 (2011) 5493-5512.

[20] J.L. Jespersen, E. Schaltz, S.K. Kaer, Journal of Power Sources, 191 (2009) 289-296.

[21] S.J. Andreasen, J.R. Vang, S.K. Kaer, International Journal of Hydrogen Energy, 36 (2011) 9815-9830.

[22] R. Bouchet, S. Miller, M. Duclot, J.L. Souquet, Solid State Ionics, 145 (2001) 69-78.

[23] Y. Oono, A. Sounai, M. Hori, Journal of Power Sources, 189 (2009) 943-949.

[24] A.D. Modestov, M.R. Tarasevich, V.Y. Filimonov, N.M. Zagudaeva, Electrochimica Acta, 54 (2009) 7121-7127.

[25] H.L. Lin, Y.S. Hsieh, C.W. Chiu, T.L. Yu, L.C. Chen, Journal of Power Sources, 193 (2009) 170-174.

[26] W.H. Zhu, R.U. Payne, B.J. Tatarchuk, Journal of Power Sources, 168 (2007) 211-217.

[27] W.H. Zhu, R.U. Payne, R.M. Nelms, B.J. Tatarchuk, Journal of Power Sources, 178 (2008) 197-206.

[28] Q.F. Li, R.H. He, J.O. Jensen, N.J. Bjerrum, Chemistry of Materials, 15 (2003) 4896-4915.

[29] Q.F. Li, R.H. He, R.W. Berg, H.A. Hjuler, N.J. Bjerrum, Solid State Ionics, 168 (2004) 177-185.

[30] R.H. He, Q.F. Li, G. Xiao, N.J. Bjerrum, Journal of Membrane Science, 226 (2003) 169-184.

[31] R. O'Hayre, S.-W. Cha, W. Colella, F.B. Prinz, Fuel Cell Fundamentals, John Wiley & Sons, New York, Hoboken, New Jersey, 2006.

[32] D.B. Sepa, M.V. Vojnovic, A. Damjanovic, Electrochimica Acta, 26 (1981) 781-793.

[33] N.M. Markovic, R.R. Adzic, B.D. Cahan, E.B. Yeager, Journal of Electroanalytical Chemistry, 377 (1994) 249-259.

[34] S.R. Taylor, E. Gileadi, Corrosion, 51 (1995) 664-671.

[35] R.U. Payne, Y. Zhu, W.H. Zhu, M.S. Timper, S. Elangovan, B.J. Tatarchuk, International Journal of Electrochemistry, 2011 (2011).

Chapter 4

EIS Application to Proton Exchange Membrane Fuel Cells

Stack Degradation and Performance Diagnostics

4.1. Introduction

In Chapter 3, a non-ideal equivalent circuit (EC) model was proposed to simulate both high temperature (HT) and traditional proton exchange membrane (PEM) fuel cell stacks (Figure 3.3). The interpretation of impedance was performed based on the widely accepted cell mechanisms. A performance comparison between two commercial PEM fuel cell stacks manufactured based on current PEM technologies was also presented in the previous chapter. In this chapter, the rationality of this EC model will be further validated by simulating the HT-PEM fuel cell stack modules under other operating conditions. The emphasis will be placed on the performance comparison to HT stack itself under various operating conditions. The competency of electrochemical impedance spectroscopy (EIS) and EC simulation on stack diagnostics will be shown in this chapter.

Certain degradations is found in the HT-PEM fuel cell stack. It brings uncertainty and unexpected behaviors to the stack performance. The experimental data also present a more complicated behavior. However, the study on this stack still provides important experience and references for practical applications of HT-PEM fuel cells and EIS diagnostics.

4.2. Experimental details

4.2.1. EIS measurement

Following the HT-PEM fuel cell stack specifications, impedance equipment, electric circuit connection, and measurement procedures described in Chapter 3, the impedance of the commercial HT-PEM fuel cell stack was collected under various operating temperatures and stack loads. All measurements was carried out with pure H_2 as fuel supplement and ambient air as both reactant and cooling. The operating temperature was set at 120°C, 140°C, and 160°C from low to high. A *dc* current load of 4.5 A, 9 A, 12 A, 13.5 A, and 15 A was loaded to the stack at each setting temperature, which is a current density of 100 mA cm^{-2}, 200 mA cm^{-2}, 267 mA cm^{-2}, 300 mA cm^{-2}, and 333 mA cm^{-2}, correspondingly. A bleeder resistor of 24 Ω is connected directly across the stack terminals. It is enabled and disabled by the Embedded Fuel Cell Control Unit (EFCU) (Serenergy Inc.) to provide a minimum load of 2 A for the stack module. Under the setting of the EFCU control system, the resistor is not disabled until the stack current goes over 4 A. Thus, the current load is chosen above 4 A to avoid the effect of the bleeder resistor. For each current load setting, the frequency swept from 10 kHz to 0.1 Hz at a rate of 10 points per decade, and the stack impedance was generated at each frequency point. This whole set of measurement procedures was repeated to collect the second sets of impedance spectra of the HT-PEM module for degradation study.

4.2.2. Polarization curves

After finishing the measurement of the first set of impedance data, the method of current sweep was conducted to measure the polarization curve (i-V curve) of the stack. The operating temperature of the stack was set at 160°C. And the stack was running at a

current load of 9 A (200 mA cm^{-2}) to reach a stable condition. The current loaded to the stack was then sweep from 0.5 A to 32 A by a step of 0.5 A at a rate of 1 A/min. After reaching 32 A, the current go back to 0.5 A at the same step magnitude and sweep rate. The output voltage at each current point was measured. Along with the increase of current load, the temperature of the stack was continuously increasing. Thus, the voltage measured during the back cycle was a little bit higher than the forth cycle. An average value was used to plot the polarization curve.

4.3. Results and discussion

Since 160ºC is the theoretical optimal operating temperature, the impedance spectrum measured at this temperature setting in the first data set is analyzed to evaluate the performance comparison to the traditional PEM fuel cell stack in Chapter 3. Impedance spectra measured at other operating temperature in the first data set is analyzed to illustrate temperature dependence of impedance and further validate the current dependence of impedance. The comparison between the first and the second set of stack impedance data is analyzed to perform the degradation study of this stack.

4.3.1. EC simulation of the first set of data

4.3.1.1. Impedance dependence on current density.

The impedance spectra measured at operating temperatures 120ºC (Figure 4.1) and 140ºC (Figure 4.2) under changing stack loads are plotted in Nyquist plots with their fitting curves simulated from the stack EC model. The points indicate the experimental data and the solid and dashed lines represent the simulation results. As the impedance analysis on spectra obtained at 160ºC in Chapter 3, the impedance spectra obtained at lower operating temperatures also shows similar dependence of stack impedance on

Figure 4.1. The impedance spectra of the HT-PEM stack module collected at an operating temperature set at 120°C under varying current load density and their fitting curves simulated from the stack EC model. Pure H_2 was supplied to the stack anode at around 45 mbar and ambient temperature. Ambient air was taken into the stack cathode by the blower.
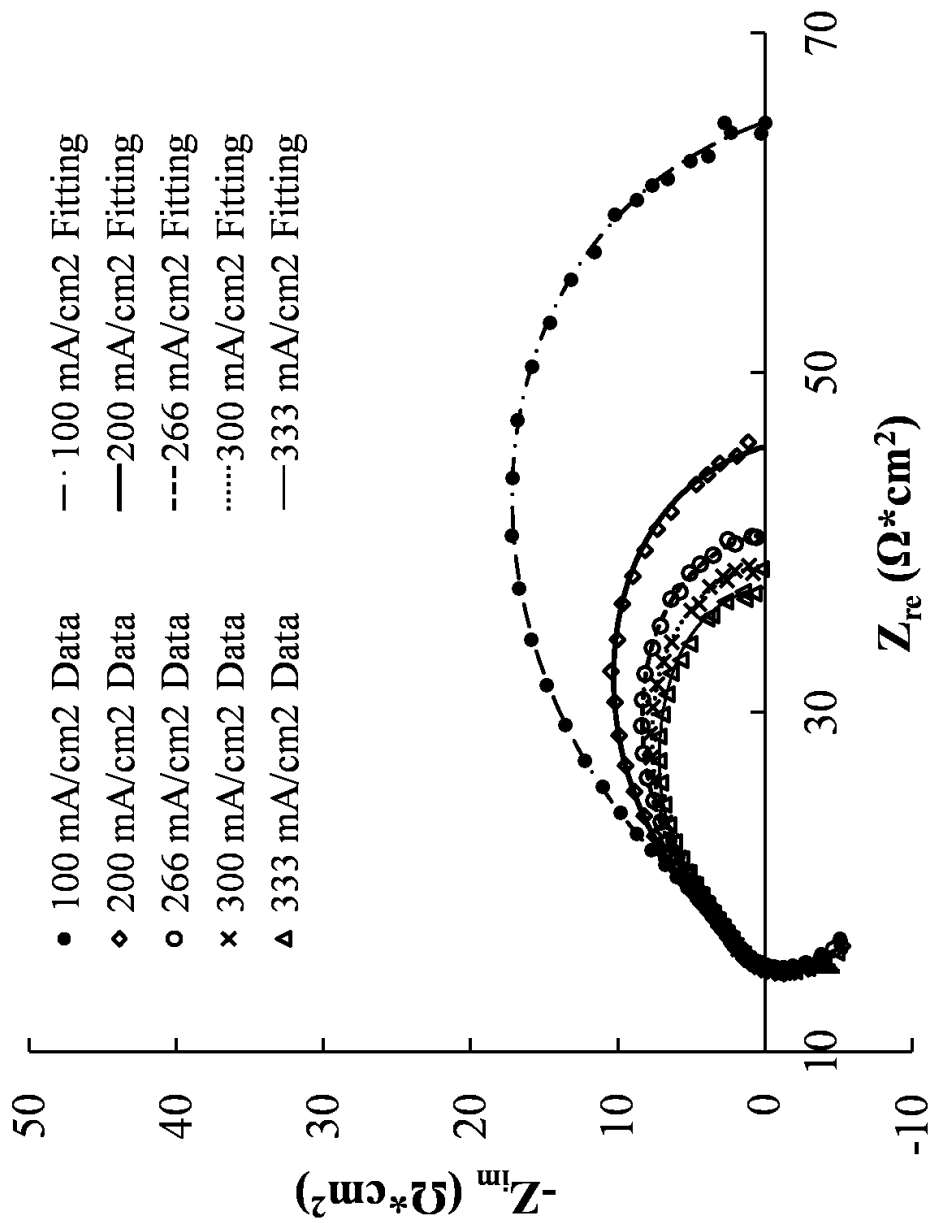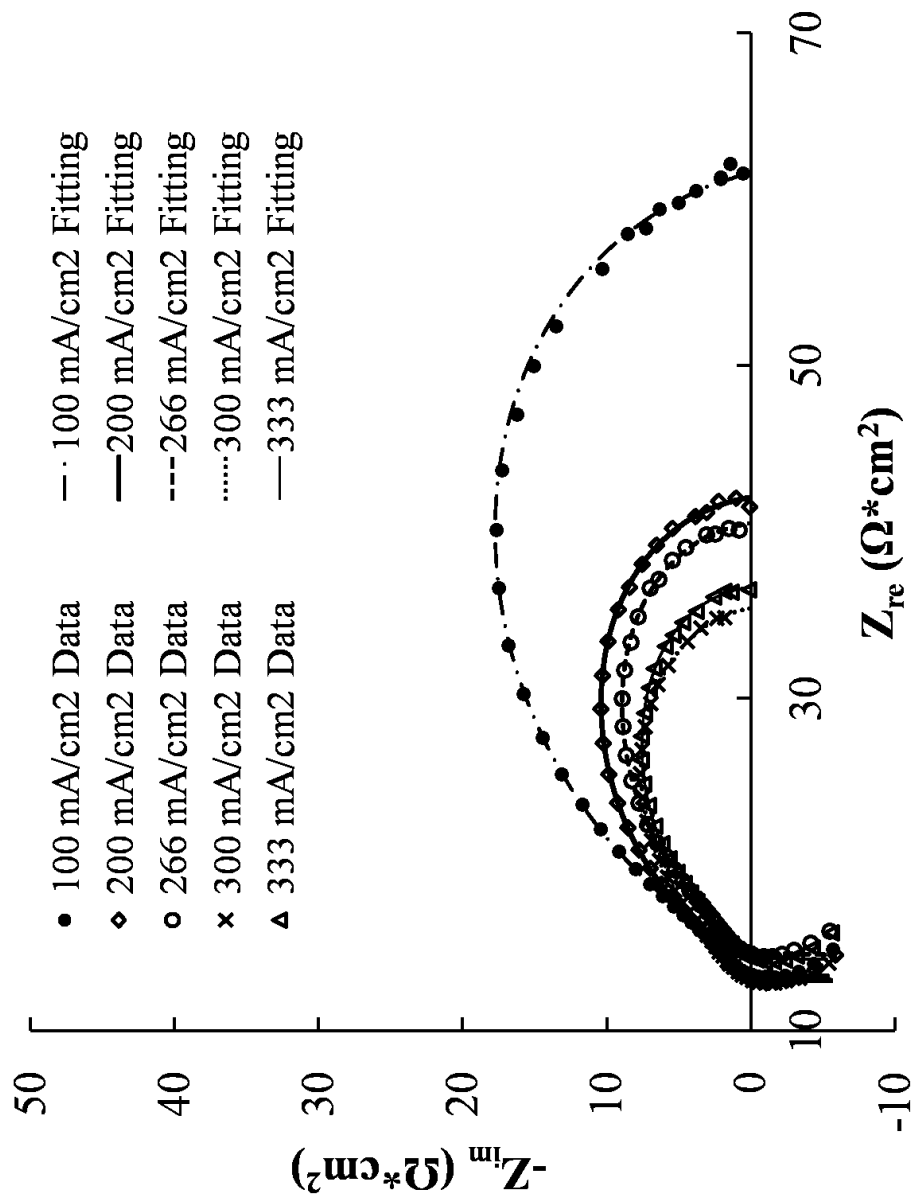
Figure 4.2. The impedance spectra of the HT-PEM stack module collected at an operating temperature set at 140°C under varying current load density and their fitting curves calculated from the derived EC model shown in Figure 3.3. Pure H_2 was supplied to the stack anode at around 45 mbar and ambient temperature. Ambient air was taken into the stack cathode by the blower.

current density. The ohmic resistance (R_Ω) and charge transfer resistance (R_a) do not show significant dependence on current density. But the large capacitive impedance arc, spanning over the middle and low frequency region, shrinks significantly with the increasing current density. This is because that smaller energy is required to surmount the activation barrier at larger overpotential, which means the activation process overcomes smaller impedance at higher temperature.

4.3.1.2. Impedance dependence on temperature.

The impedance spectra measured under a current load of 200 mA cm^{-2} at three different operating temperature is illustrated in Figure 4.3. The points are impedance data measured from the stack, and the lines are fitting curves simulated from the EC model derived in Chapter 3 (Figure 3.3). Generally, smaller impedance is expected at higher operating temperature due to faster kinetics. However, the stack impedance shifts to the right on Nyquist plot when the operating temperature increases from 120°C to 160°C (Figure 4.3). This means the ohmic resistance (R_Ω) of the stack increases with increasing temperature. Comparing the fitting values of the EC elements, the resistance of ORR process on cathode (R_c) (Figure 4.5) also presents the same behavior as the ohmic resistance (R_Ω) (Figure 4.4). While the charge transfer resistance of HOR process on anode (R_a) (Figure 4.4) slightly increases with increasing temperature but almost keeps at a constant level.

Several other groups also reported similar unexpected temperature dependence of the ohmic resistance (R_Ω) [1-3] and ORR resistance (R_c) [1, 2, 4]. The most possible explanations for this phenomenon are the dehydration of the membranes [1, 2] and the decrease of gas concentration in the diffusion layer [1, 4]. Although water is no longer
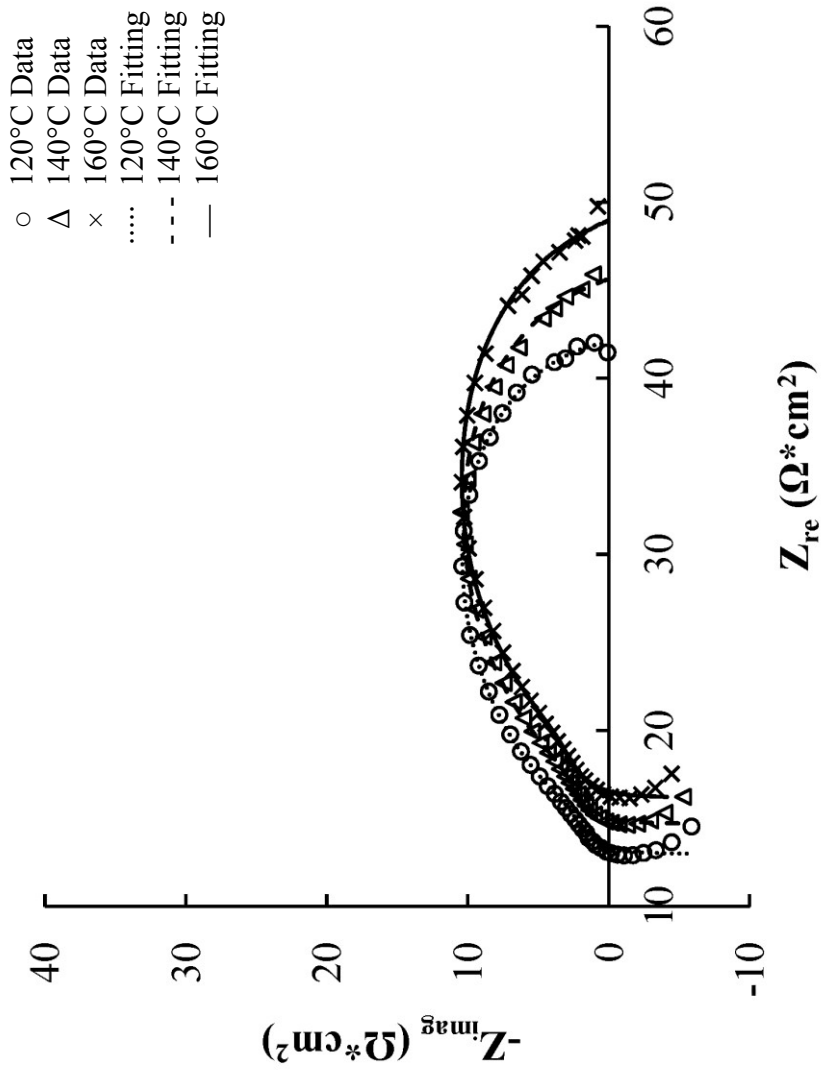
Figure 4.3. The impedance spectra of the HT-PEM fuel cell stack module measured under a current load of 9 A (200 mA cm^{-2}) with the operating temperature set at 120°C, 140°C, and 160°C. Their fitting curves are calculated from the stack EC model derived in Chapter 3 (Figure 3.3). Pure H$_2$ was supplied to the stack anode at around 45 mbar and ambient temperature. Ambient air was taken into the stack cathode by the blower.
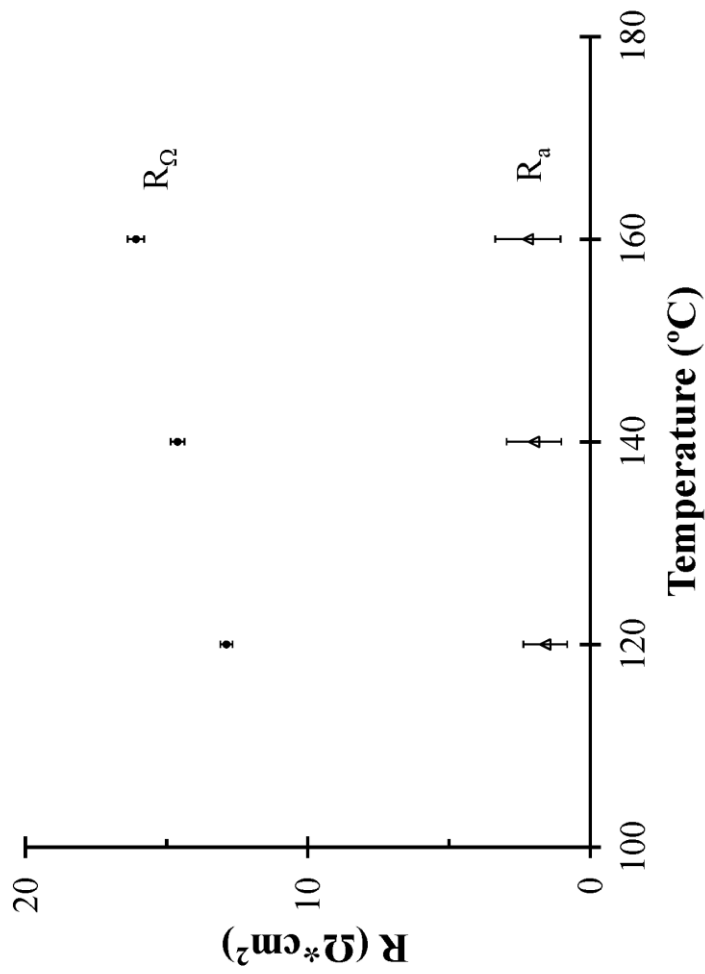
Figure 4.4. The dependence of stack module ohmic resistance R_Ω and anode HOR charge transfer resistance R_a on temperature. The values of resistors were calculated by the stack EC model. The experimental data used for simulation were three impedance spectra of the first data set measured under a current load density of 200 mA cm^{-2} (Figure 4.2).
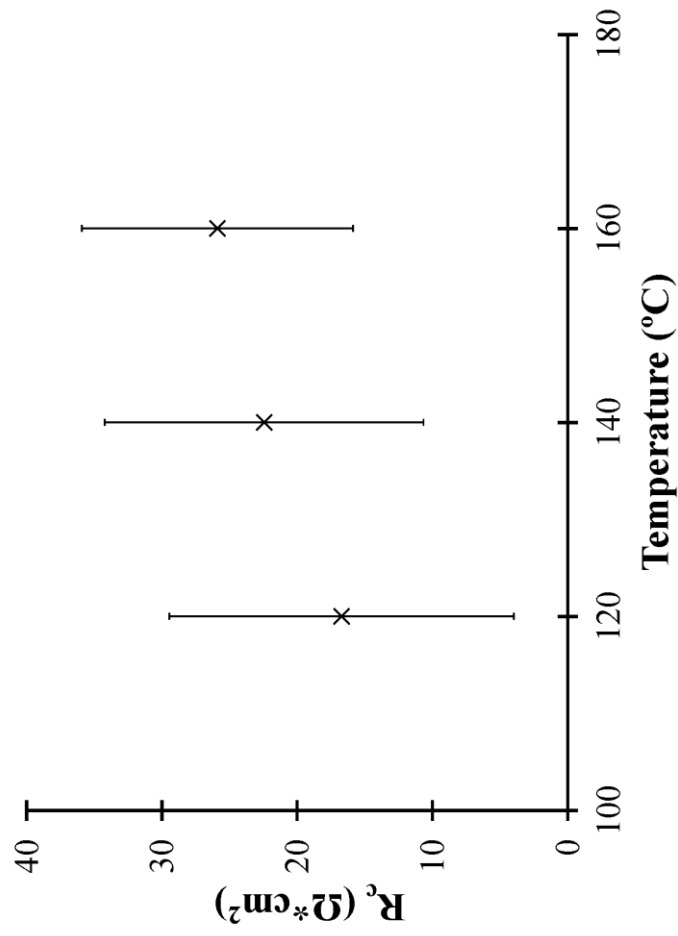
Figure 4.5. The dependence of stack module cathode ORR resistance R_c on temperature. The values of resistors were calculated by the stack EC model. The experimental data used for simulation were three impedance spectra of the first data set measured under a current load density of 200 mA cm^{-2} (Figure 4.2).

essential for proton conductivity in PA doped PBI membranes, the humidity of membranes can change its conduction mechanism [1], which changes the impedance dependence on temperature.

4.3.2. Stack degradation

4.3.2.1. Comparison between two sets data of impedance spectra

The measurement of the second set of impedance spectra repeats the procedure of the first set. Two measurements are carried out under the identical settings of operating conditions. However, the measured impedance spectra have different shapes and different magnitudes (Figure 4.6). The derived stack EC model still present great fitness for data fitting. The fitting values of ohmic resistances and polarization resistances are listed in Table 4.1.

The ohmic resistance (R_Ω) here includes not only the resistances of cell membranes and electrodes, but also electronic devices and controllers connected in the stack modules. Generally, it is expected to be independent on current density. The ohmic resistance (R_Ω) of the first data set presents a slight decrease with increasing current density; however, the change is almost unnoticeable in the Nyquist plots (Figure 4.6). But it is quite significant that the ohmic resistance (R_Ω) of the second data set decreases with increasing current density. This means that the stack underwent a more unstable operation during the second measurement than the first one.

The polarization resistance (R_p) is the sum of the activation resistances and the concentration resistance. In a Nyquist plot, R_p is indicated as the difference between two interceptions in the real axis. Comparing two sets of impedance data, the polarization
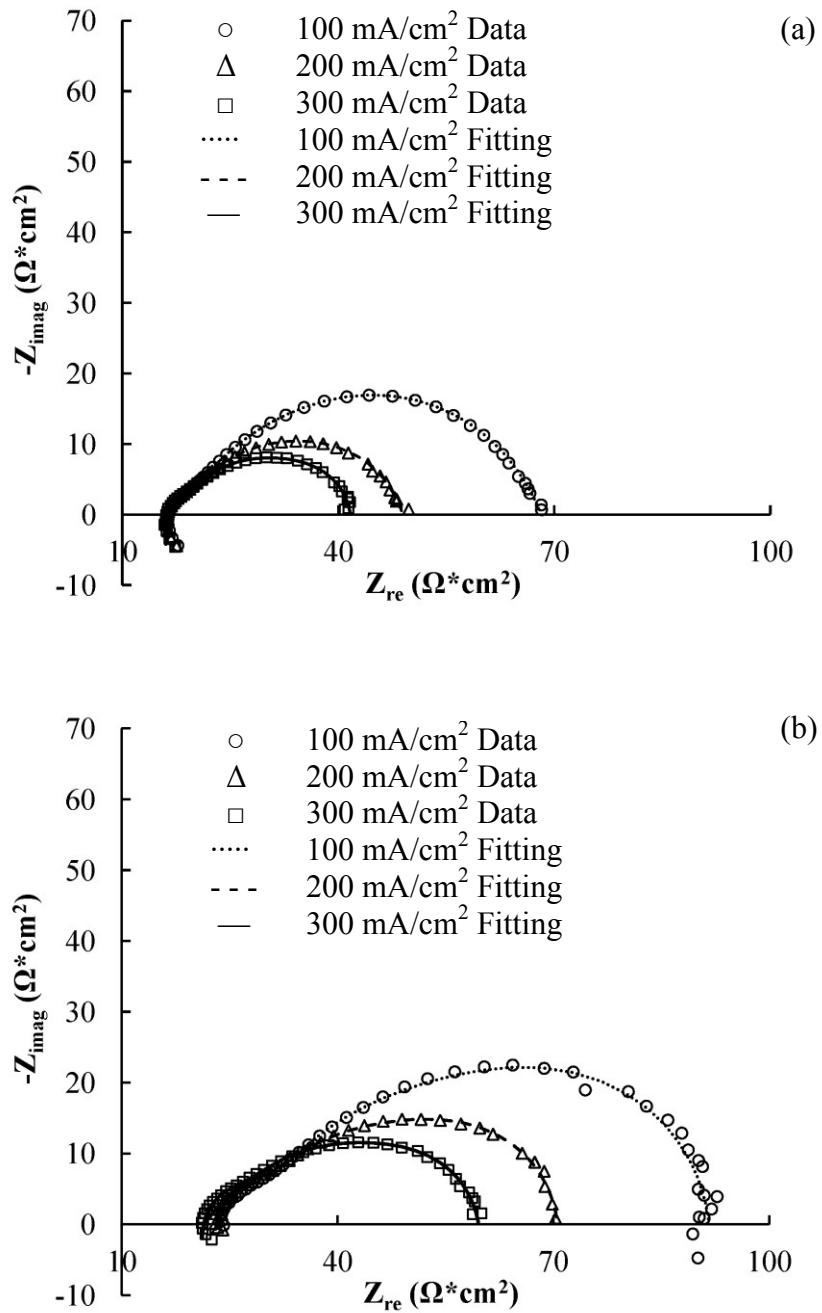
Figure 4.6. The (a) first and (b) second set of impedance spectra measured at 160°C. The current density was loaded at (○) 100 mA cm^{-2}, (Δ) 200 mA cm^{-2}, and (□) 300 mA cm^{-2}, and their fittings (dashed and solid lines) calculated from the stack EC model.

Table 4.1. The fitting data of R_Ω and R_p calculated from the EC simulation.

Current Density	The First Set		The Second Set	
i (mA/cm^2)	R_Ω (Ω*cm^2)	R_p (Ω*cm^2)	R_Ω (Ω*cm^2)	R_p (Ω*cm^2)
100	16.19	52.01	23.22	68.46
200	16.08	32.89	22.68	47.94
300	15.89	25.80	20.93	38.71

resistance (R_p) of the stack increased significantly when conducting the second set of measurement.

To compare in a more intuitive way, two sets of impedance data collected at 160°C and different current densities are plotted together in one Nyquist plot, shown in Figure 4.7. The second set of data, although repeating the procedures and operating conditions of the first set, presents significant differences from the first set of data. Both the ohmic loss and the polarization loss of the second set of impedance data increase, as concluded from the simulation data listed in Table 4.1.

4.3.2.2. Comparison between polarization curves

The performance degradation can also be implied from observing the decrease in cell voltages. When measuring the impedance, the stack voltage was recorded at each current load. The average voltage of single planar cell in the stack was calculated from the stack voltage and plotted in Figure 4.8. The cell voltage decreased when conducting the second set of measurement. Also, the polarization curve measured after the first set of impedance measurement is compared to the one measured by Serenergy at the beginning of life (BOL) of the stack module (Figure 4.9). A significant performance degradation is observed and about one third of the maximum output power measured at its BOL is dropped.

To find out the reasons for the change of the stack impedance, the status of the blower and heater during two sets of measurement were studied. It was shown that the blower worked in the same speed range when the stack was operated at the same conditions. Also, the heater was disabled when performing impedance measurement.
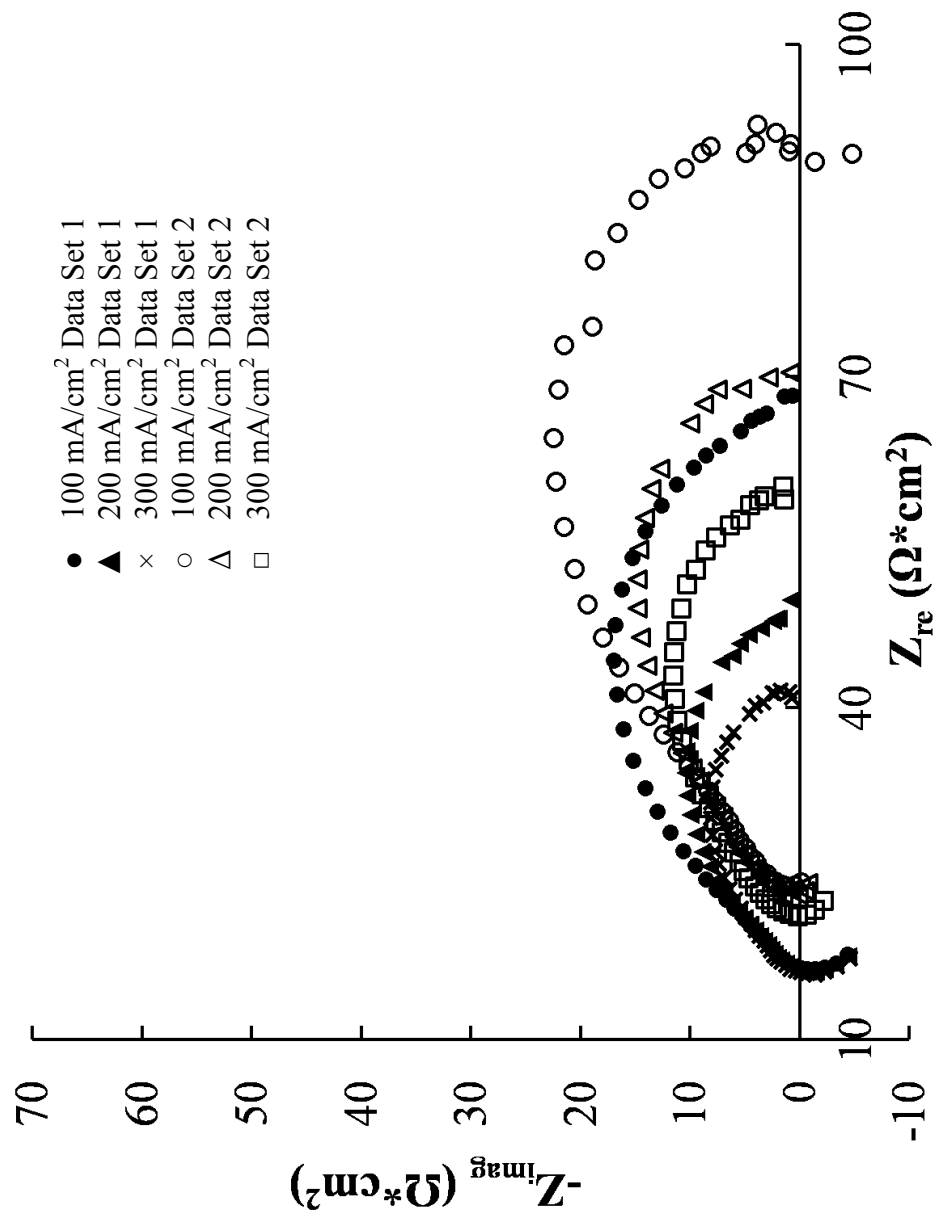
Figure 4.7. Two sets of impedance spectra of the high temperature PEM stack measured under the same operation setting. The operating temperature was set at 160°C and the current density changes from 100 mA cm^{-2} to 300 mA cm^{-2} for each data set.
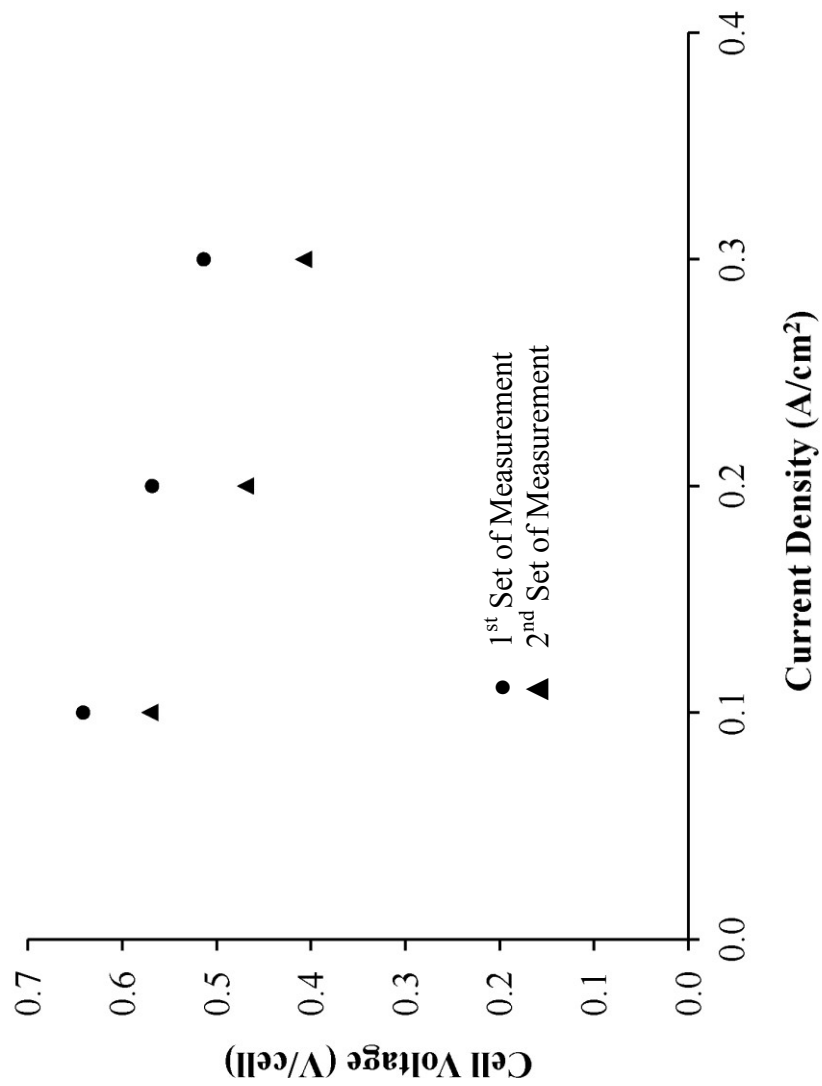
Figure 4.8. The voltage of each single cell in the stack when conducting the (●) first and the (▲) second set of impedance measurement. A current density of 100 mA cm^{-2}, 200 mA cm^{-2}, and 300 mA cm^{-2} was loaded to the stack.
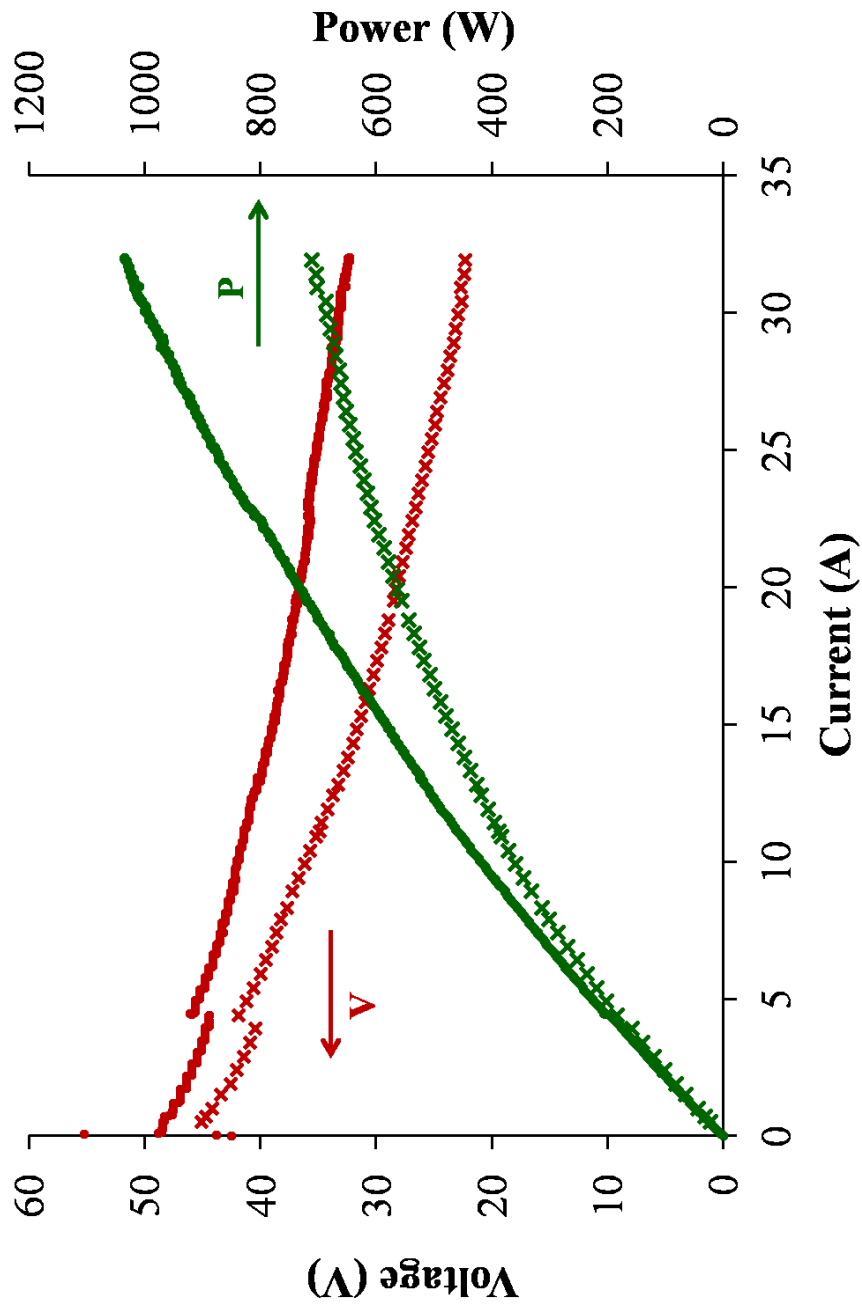
Figure 4.9. Comparison between the polarization curves collected from the HT-PEM stack module (●) at its BOL and (x) after the first set of impedance measurement. Both curves were obtained after the stack was stable at an operating temperature set at 160°C.

Thus, the energy consumptions of the blower and heater did not contribute to the inconsistency of stack impedance.

The temperature profile of the stack is monitored by three temperature sensors during impedance measurement. For both sets of experiments, the variations of the stack temperature with the operating time is more significant when the stack was operated at the current density of 100 mA cm^{-2} than at higher loads. And at this current load, all three temperatures are lower than 160°C. When the current density increases to 200 mA cm^{-2}, the middle and rear temperatures of the stack were able to be stabled at 160°C, and the temperature variations with the operating time is negligible. However, the front temperature still stay at a value lower than 160°C. At a current density of 300 mA cm^{-2}, the front temperature is able to elevate up to about 150°C. The decrease of the temperature gradient over the whole stack provided a more stable condition for the stack operating. Although the temperature profiles behaved similar in both sets of measurements, the temperature variations with the operating time during the second measurement were more observable than during the first one. Also, the front temperature of the stack when conducting the second set of measurement was generally lower than the first one. It amplified the temperature gradient over the whole stack and induced more cell impedance.

4.4. Conclusion

Two sets of impedance measurement were carried out following the same procedure. The operating conditions of the HT-PEM fuel cell stack module is set at the same values. However, the measured impedance spectra failed to present identical or similar performance behavior as expected. The EC model derived in Chapter 3 for stack

simulation is used to simulate these two sets of impedance spectra. The stack model gives great fitness to the experimental data. The performance degradation of the HT-PEM fuel cell stack is quantitatively analyzed by the impedance values simulated from the stack EC model. Polarization curves are also used to illustrate the conditions of the stack module.

The impedance data measured at lower operating temperatures also shows similar current dependence as at 160ºC. Stack impedance decreases with increasing current loads. The difference is most significant when the load increases from 100 mA cm^{-2} to higher current density. The stack impedance increases with decreasing temperature at all loads. Although this trend is not expected according to activation theory, similar phenomena also discovered by other research groups. The complicate proton conduction mechanism of PA-PBI membranes introduces more effect factors to the dependence of stack impedance on operating temperature.

Reference

[1] C.Y. Chen, W.H. Lai, Journal of Power Sources, 195 (2010) 7152-7159.

[2] J. Lobato, P. Canizares, M.A. Rodrigo, J.J. Linares, Electrochimica Acta, 52 (2007) 3910-3920.

[3] J.L. Jespersen, E. Schaltz, S.K. Kaer, Journal of Power Sources, 191 (2009) 289-296.

[4] J.L. Zhang, Y.H. Tang, C.J. Song, J.J. Zhang, Journal of Power Sources, 172 (2007) 163-171.

Chapter 5

EIS Application to Tubular Solid Oxide Fuel Cells

Single Cell Characterization and EC Simulation

5.1. Introduction

Electrochemical impedance spectroscopy (EIS) is applied to the tubular solid oxide fuel cells (T-SOFCs) in this chapter. The cell tubes are manufactured at commercial level. The complex compositions and structures of the electrodes, the oxygen-ion (O^{2-}) conducting electrolytes, and the high operating temperature up to 1000ºC make the kinetic mechanisms of SOFC processes very different from proton exchange membrane (PEM) fuel cells. The practical cell operation with reformate fuel takes the impedance study into a more complicated situation. The mechanisms of electrode reactions in SOFC systems are not well understood. Even less attention has been paid to SOFCs with tubular geometry. No impedance data of SOFCs directly fueled with reformate has been published. The measurements and results described and analyzed in this chapter provide a preliminary study on reformate fueled T-SOFC systems.

5.2. Cell descriptions and experimental details

5.2.1. Tubular solid oxide fuel cells (T-SOFCs)

The impedance spectra of tubular solid oxide fuel cells (T-SOFC, patented by Acumentrics Corp.) were small tubes with a horizontal 22 mm inner diameter by 450 mm long. Five single tubes were horizontally placed in the same Cell Test Stand, parallel to

each other. They were numbered from Cell 1 to Cell 5 in sequence. Cell 1 and Cell 5 were two tubes placed on the sides, and Cell 3 was the one placed in the middle. The tubes were anode-supported SOFCs, with the anode as the inside wall of the tube and the cathode as the outside wall. The O^{2-} conducting electrolyte was stacked between the anode and the cathode. Ambient air was circulated around the tubes, supplying oxygen to the cathodes of the T-SOFCs. A mixture of hydrocarbon with a general structure of C_nH_{2n+2} was fed into the tube. It was reformed inside the tube into hydrogen (H_2) and carbon monoxide (CO) along the flow of the fuel mixture. The generated H_2 and CO were continuously oxidized to water (H_2O) and carbon dioxide (CO_2) along the fuel flow and produced electricity. This tubular geometry of SOFC is able to integrate the reformer into each cell. An approximate area of 215 cm^2 was measured (data provided by Acumentrics) as the nominal area of each single T-SOFC tube. This number is only about one third of the inner area of each tube, because part of the tube was served as the internal fuel reformer for the mixture of hydrocarbons.

5.2.2. Experiments

The testing tubes were manufactured at commercial level. The measurements were conducted during cell operations under different temperatures, current densities, and fuel utilizations. These parameters were set before cell operations at a desired number. However, it was usually difficult to stable the cells exactly at the operating conditions as set. The parameters described below refers to the desired number set before the operations. The status of cell tubes were stabled as close to the set parameters as possible during the practical operations.

The Cell Test Stand was preheated to 800ºC. The impedance spectrum of Cell 1 was measurement under a current density around 120 mA cm^{-2} at a fuel utilization around 50%. The measurement was repeated on Cell 3 and Cell 5 in sequence under the same operation setting. The impedance was then measured from Cell 3. The Cell Test Stand was preheated to about 750°C. A current density of 120 mA cm^{-2} was loaded to Cell 3. Its impedance spectra were obtained after the tube was stabilized at a fuel utilization of 50%, 75%, and 29% in sequence. For validation of EC simulation, the impedance spectra of Cell 3 were then measured under a current density of 150 mA cm^{-2} with a fuel utilization stable at around 50% and 75%.

The impedance measurement was performed by Gamry FC350^{TM} fuel cell monitor (Gamry Instruments) in mode of low noise Galvanostatic EIS. For each measurement of impedance spectra, the frequency swept from 10 kHz down to 0.01 Hz at the rate of 10 points per decade. The amplitude of *ac* signal applied to the single T-SOFC tube during the measurement was 0.25 A. The external electric currents were loaded to the testing cells by connecting to TDI-Dynaload$^{®}$ RBL488 programmable load.

5.3. Results and discussion

5.3.1. Comparison of impedance spectra between cells

The impedance spectra measured from Cell 1, Cell 3, and Cell 5 under a current density of 120 mA cm^{-2} at 800ºC with a fuel utilization of 50% is plotted in the same Nyquist plot for comparison (Figure 5.1). The configuration of three cell tubes are identical to each other, however significant differences can be observed from their impedance under the same operation setting. Cell 3 performs smaller total impedance than the other two cells. It is placed in the middle between Cell 1 and Cell 5. This
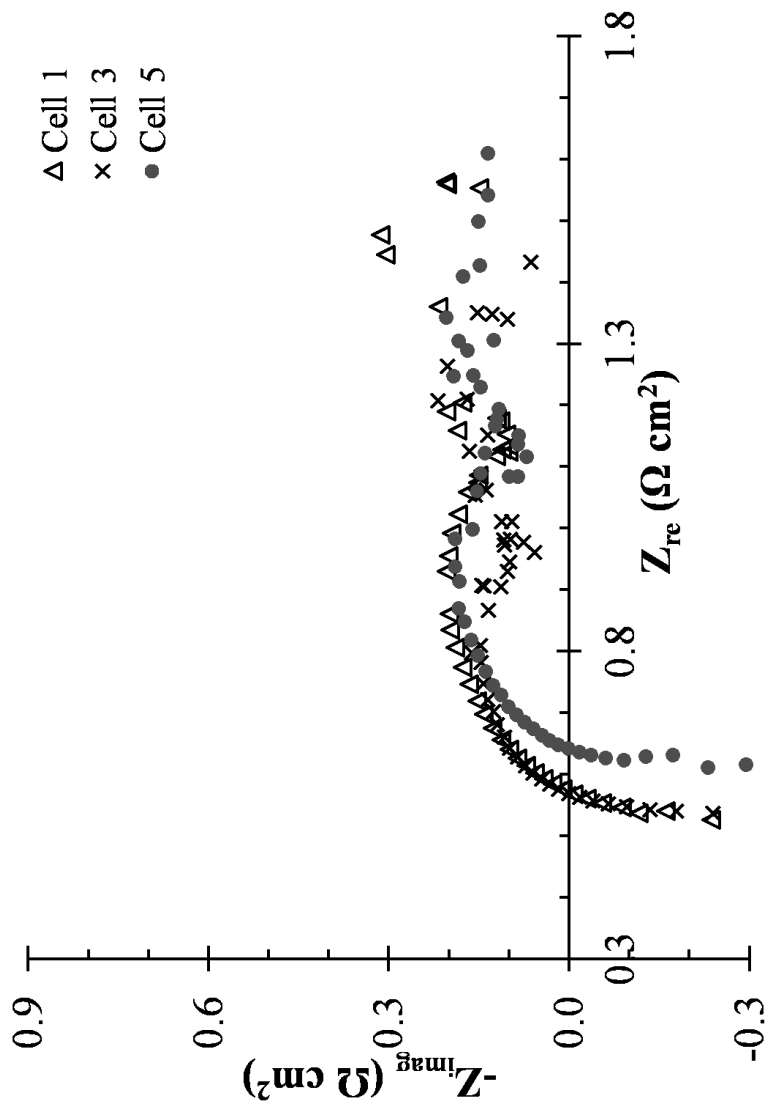
Figure 5.1. Impedance spectra of Cell 1 (△), Cell 3 (×), and Cell 5 (●) measured under a current density of 120 mA cm^{-2} at 800°C with a fuel utilization of 50%.

position minimize the effect of ambient environment on the cell operation during measurement. Both the operating temperature and fuel supplement are able to be maintained at a more stable status closer to the setting of operation. The impedance spectra measured from Cell 3 are used for simulation analysis below.

5.3.2. EC simulation

The impedance spectrum of Cell 3 measured under a current density of 120 mA cm^{-2} at 800°C with a fuel utilization of 50% is shown in Figure 5.2, along with its fitting curve simulated from the non-ideal EC model shown in Figure 5.3. Two large capacitive impedance arcs are clearly separated in the Nyquist plot. The one in the higher frequency region is considered as three overlapped impedance arcs contributed from different processes. The paralleled (R_aC_a) sub-circuit simulates the impedance arc above 100 Hz, ascribing to the oxidation reaction process at anode. The paralleled (R_cQ_c) sub-circuit simulates the impedance arc dominating the frequency range from 100 Hz down to around 10 Hz, ascribing to the oxygen reduction reaction (ORR) process at cathode. SOFC systems have more complicated ORR mechanism on cathode than PEM fuel cell systems. The rate determining step (RDS) changes with different cell operating conditions, electrode materials, and other cell configurations. Measurements at different O_2 concentration can be used to validate the simulation and interpretation of ORR impedance. The constant phase element (CPE) Q_c is used to replace an ideal capacitor for non-ideal characteristics of the electrode. The finite diffusion element (FDE) O simulates the impedance arc dominating the frequency range from 10 Hz to 1 Hz. This arc overlaps the arc of (R_cQ_c) to a significant extent and bridges it to the low frequency capacitive impedance arc. It is considered as the contribution from the diffusion process on cathode.

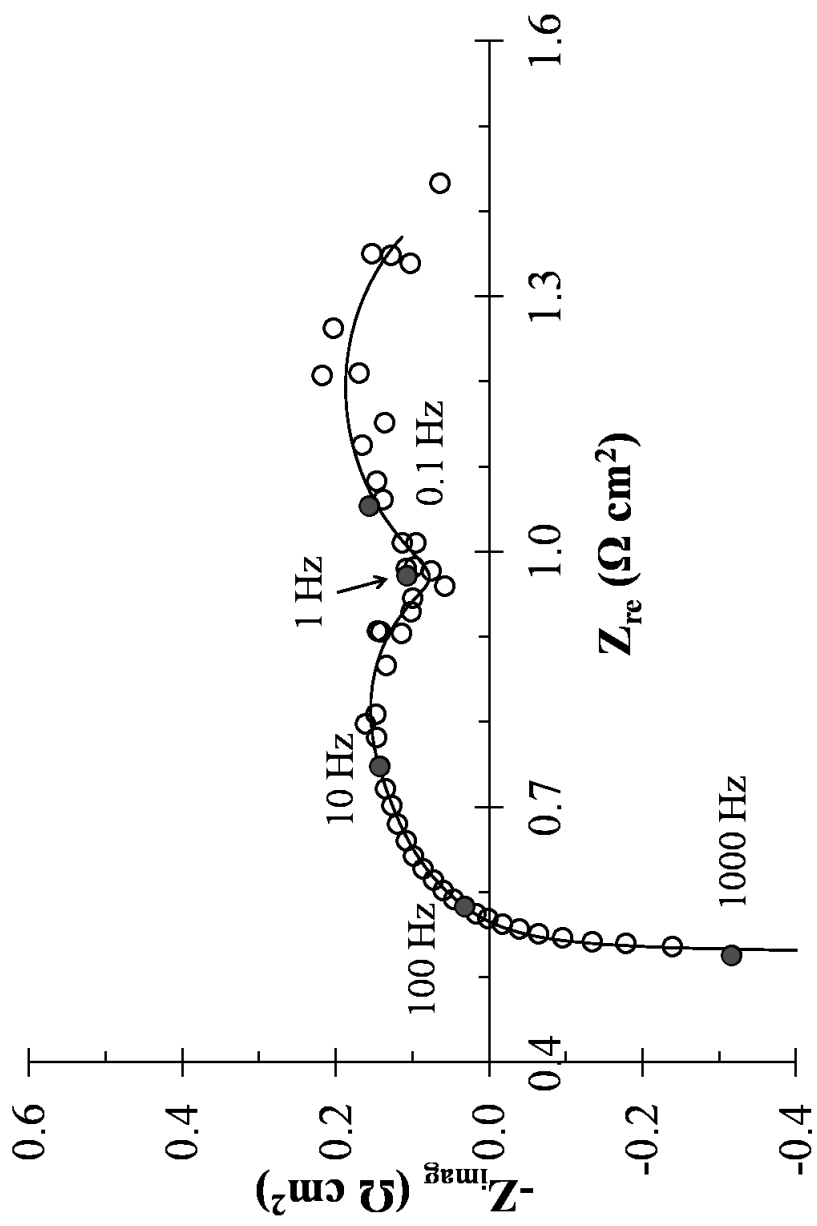**Figure 5.2.** Impedance spectra of Cell 3 (○) measured under a current density of 120 mA cm^{-2} at 800°C with a fuel utilization of 50%. The solid line is its fitting curve simulated from the non-ideal EC model shown in Figure 5.3. The dark dots marked out the impedance data measured at the frequency of 1000 Hz, 100 Hz, 10 Hz, 1 Hz, and 0.1 Hz.

117
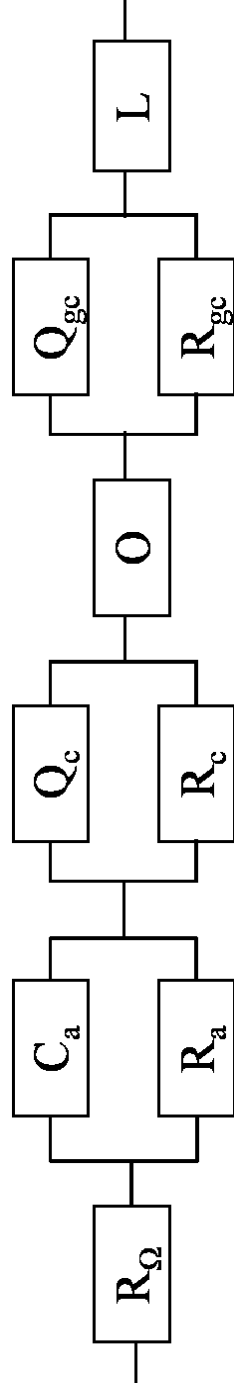
Figure 5.3. Non-ideal EC model for T-SOFC single cell simulation

The total resistance of the large capacitive impedance arc at higher frequency region is about 0.4 Ω cm^2, illustrated directly by the Nyquist plot (Figure 5.2). The impedance arc dominating the frequency range below 0.1 Hz is simulated by the paralleled ($R_{gc}Q_{gc}$) sub-circuit of the proposed EC model. It also shows a resistance of about 0.4 Ω cm^2 in Figure 5.2, equivalent to the total resistance of the capacitive arc at higher frequency. The capacitive impedance arc with such magnitude at frequency below 0.1 Hz is not related to charge transfer processes or adsorption processes. The term of "gas conversion" was put forward for the impedance arcs with similar characters in Primdahl's work [1] on their three electrode SOFC pellets. It refers to a bulk process over the electrode, with dependence on gas flow rate. The fit curve simulated from the non-ideal EC model has good consistency with the impedance spectra measured from Cell 3.

Comparing to the impedance spectra measured from the disc-like SOFC button cells fueled with a gas mixture of pure hydrogen (H_2) and water (H_2O) [2], the capacitive impedance arc does not come out until the frequency sweeps down to the magnitude of 100 Hz. However, the cathode activation process simulated by (R_cQ_c), the diffusion process simulated by O, and the gas conversion process simulated by ($R_{gc}Q_{gc}$) still dominate the frequency region similar to other studies [1-3]. This behavior indicates that the anode electrode process simulated by (R_aC_a) occurs at a slower rate in this SOFC system than in other SOFC systems. The SOFC tubes studied in this work are fueled directly with a mixture of hydrocarbons. The anode processes start with the reforming reaction of hydrocarbon, followed by the oxidation reaction of H_2 and CO. The mechanism of hydrocarbon reforming at anode has not been well understood. Its kinetics

was reported to have dependence on the steam ratio of the fuel supplement [4]. The mechanism of CO oxidation also slows the activation process on anode electrode.

5.3.3. Impedance interpretation

5.3.3.1. Dependence of temperature

Impedance spectra of Cell 3 measured when the operating temperature is set at 750°C and 800°C are plotted in Figure 5.4. Their fit curves are simulated by the proposed non-ideal EC model. The current density during measurement is 120 mA cm^{-2}, and the fuel utilization is stable at around 50%. The most significant changes introduced by the operating temperature is the decreased ohmic resistance R_Ω at elevated temperature. The measurements at only two different temperatures failed to give any quantitative dependence. However, the decrease of ohmic resistance with temperature is expected as the conductivity of O^{2-} through the ceramic electrolyte follows Arrhenius behavior [4]. The resistances of activation processes on both electrodes (R_a and R_c) decrease with increasing temperature due to improved kinetics (Figure 5.5).

As stated in Chapter 1, the diffusion resistance (R_O) is the equivalent resistance of FDE calculated from the simulation values of its time parameter B and admittance parameter $Y_{O,0}$:

$$R_O = B/Y_{O,0} \qquad (5.1)$$

The dependence of diffusion process on temperature is complicated. The kinetics of reduction reaction and the diffusivity of gas mixtures both have strong dependence on temperature, and their changes give different effects to the diffusion resistance. Moreover, the cathode diffusion process is not only contributed by the process of O_2 gas diffusion to the electrode. The surface diffusion process of adsorbed oxygen also limits
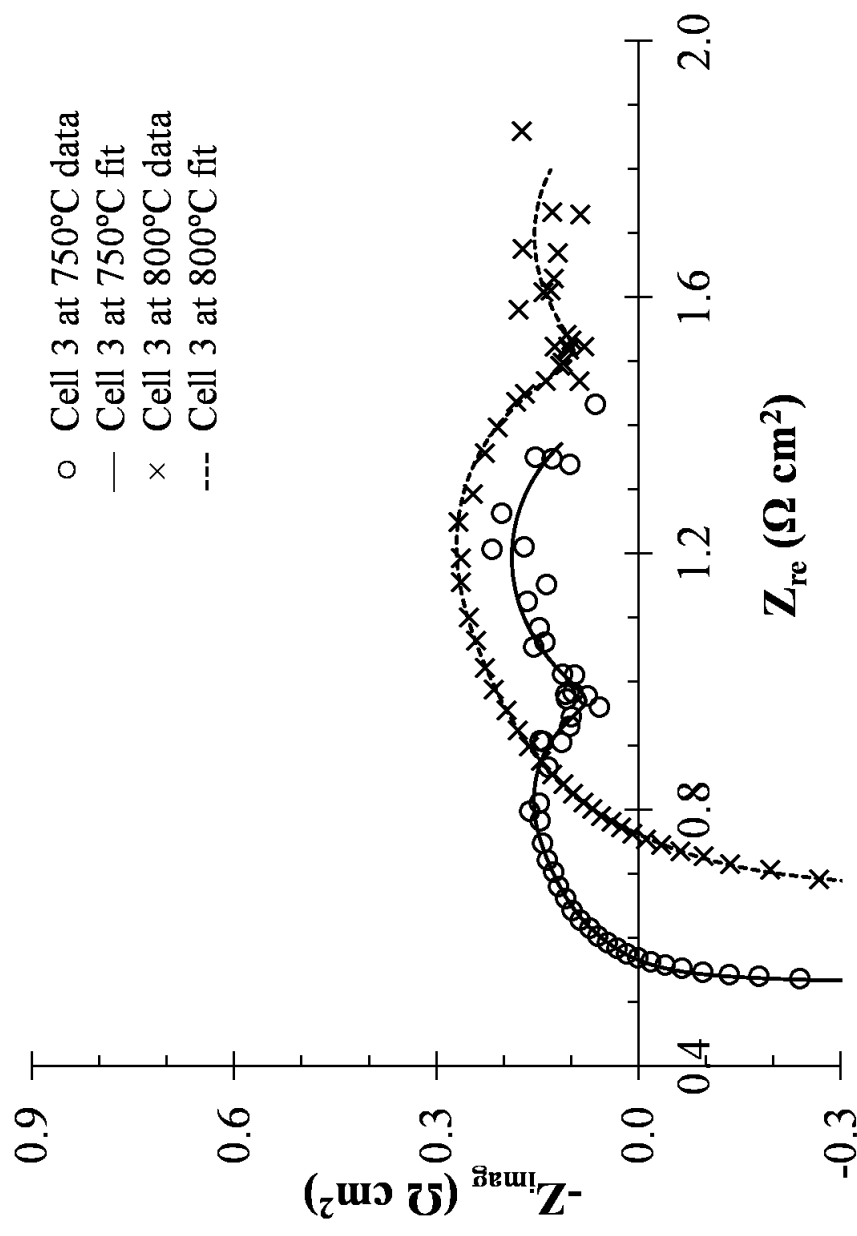
Figure 5.4. Impedance spectra of Cell 3 measured when the operating temperature is set at ($\circ$) 750°C and ($\times$) 800°C, along with their fit curves simulated from the non-ideal EC model (Figure 5.3). The current density is 120 mA cm^{-2} with a fuel utilization of 50%.

Figure 5.5. Values of resistance elements in the proposed non-ideal EC model (Figure 5.3) calculated from the simulation of Cell 3, operating at different temperature of 750°C and 800°C under a current density of 120 mA cm^{-2} with a fuel utilization of 50%. The impedance spectra for simulation are shown in Figure 5.4.

the cell performance, which is a thermally activated process [4]. Its impedance can be decreased at higher operating temperature.

The change of gas conversion resistance (R_{gc}) show reverse dependence on temperature. It increases with the increasing temperature (Figure 5.5). According to Primdahl's CSTR model established for the conversion of H_2-H_2O gas mixture [1], the value of R_{gc} is first order with respect to the operating temperature and first order reciprocal of the gas mixture flow rate. Their idea of the CSTR model can be explained as a convection process in the volume over the anode. With the increase of temperature, the volume of gas mixture expands, which decreases the gas flow rate and increases the gas conversion resistance.

5.3.3.2. Dependence of current density

Impedance spectra of Cell 3 measured under a current density of 120 mA cm^{-2} and 150 mA cm^{-2} are illustrated in Figure 5.6, along with their fit curves. The operating temperature is set at 750ºC, with a fuel utilization stabilized at about 50%. The changes of impedance spectra with the increase of cell load are mainly contributed by the improved performance of diffusion process and gas conversion process under the cell operation at higher current density (Figure 5.7). The increased current density facilitates the diffusion process of O_2 by accelerating the consumption rate of O_2. And it also decreases the gas conversion resistance by increasing the flow rate of fuel supplement. The effects of current density on activation processes of both electrodes are not as significant as expected for charge transfer processes, because the RDS of anode oxidation reaction and cathode reduction reaction change to adsorption processes especially at high operating temperatures.
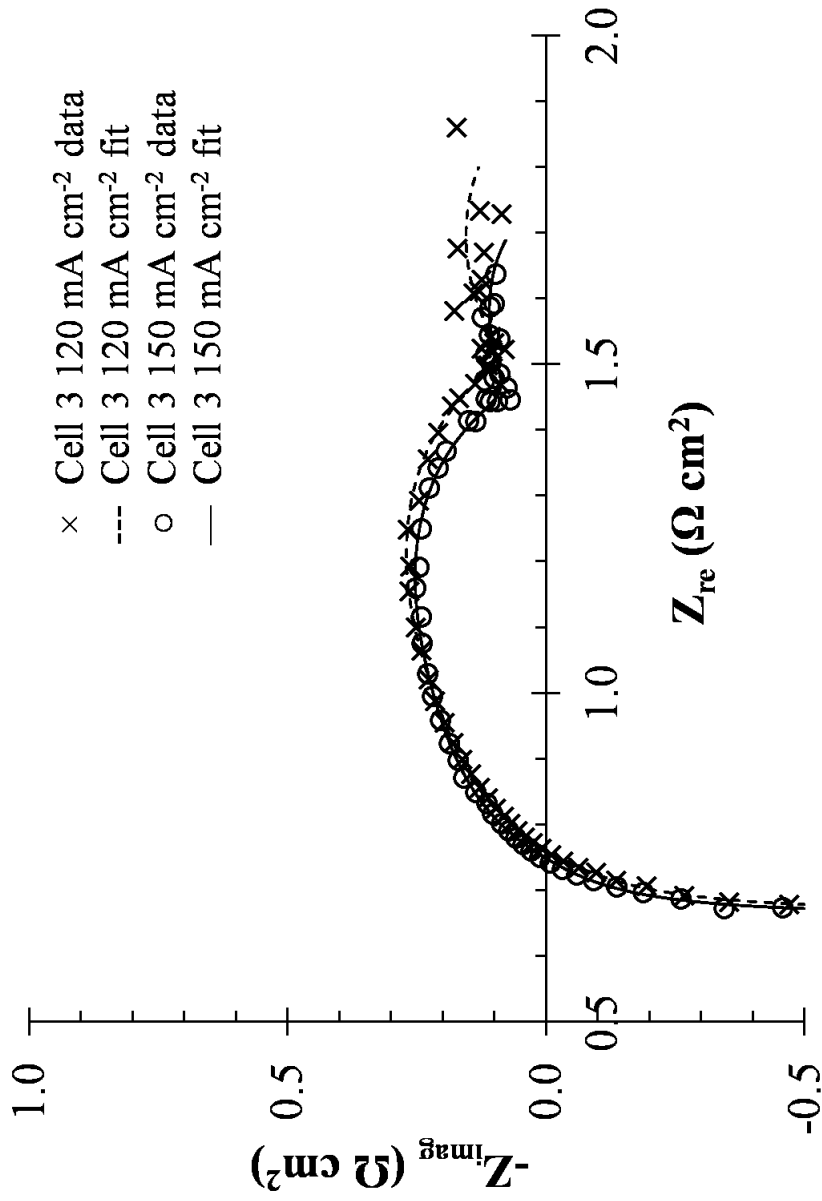
Figure 5.6. Impedance spectra of Cell 3 measured under a current density of (○) 120 mA cm⁻² and (×) 150 mA cm⁻², along with their fit curves simulated from the non-ideal EC model (Figure 5.3). The operating temperature is set at 750°C, with a fuel utilization of 50%.
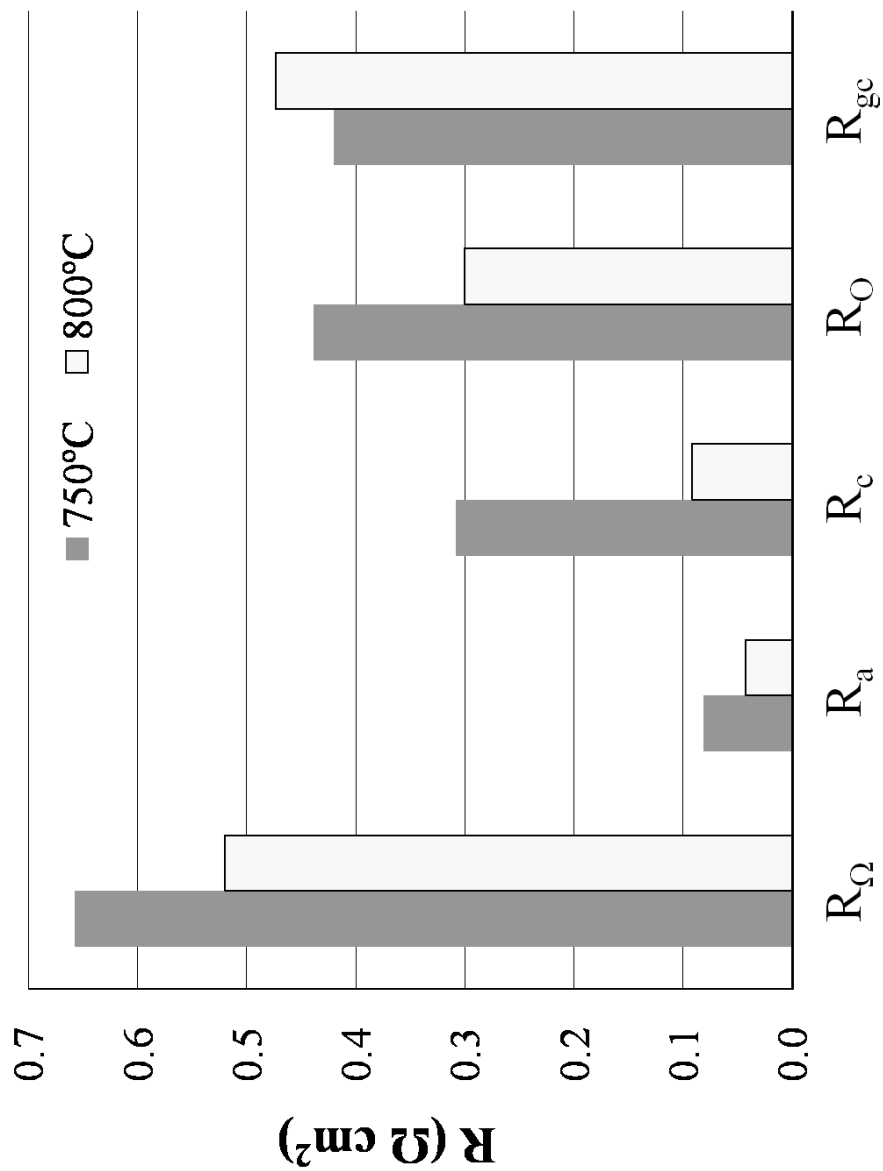
124
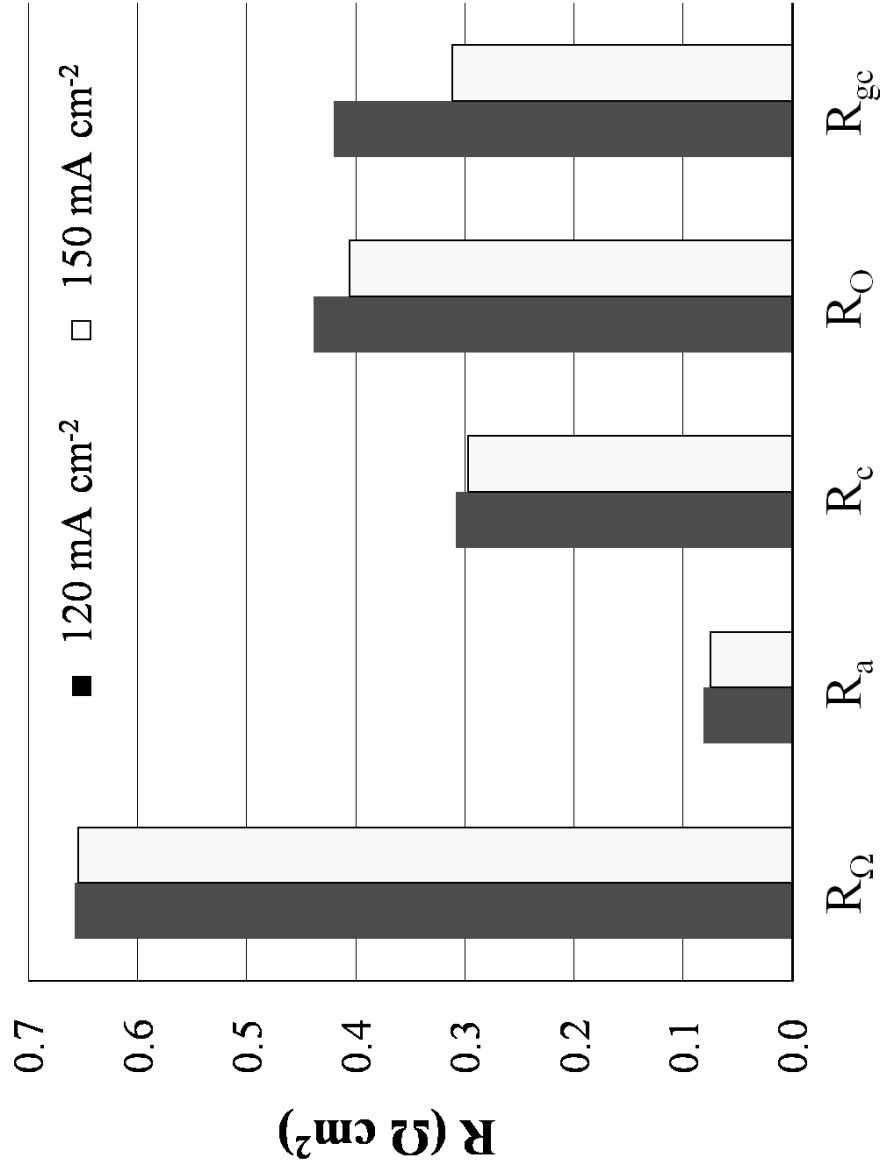
Figure 5.7. Values of resistance elements in the proposed non-ideal EC model (Figure 5.3) calculated from the simulation of Cell 3, operating at different current density of 120 mA cm^{-2} and 150 mA cm^{-2} at a temperature of 750°C with a fuel utilization of 50%. The impedance spectra for simulation are shown in Figure 5.6.

5.3.3.3. Dependence of fuel utilization

Impedance spectra of Cell 3 measured with different fuel utilization are shown in Figure 5.8. The operating temperature is set at 750ºC. A current density of 120 mA cm^{-2} is loaded to the cell tube during measurement. A smaller fuel utilization means that the larger flow rate of fuel supplement is required when the rate of fuel consumption keeps constant under the same setting of operating temperature and cell load. The impedance of electrode kinetic processes and cathode diffusion process slightly decreases with decreasing fuel utilization and almost keeps at a constant level. The impedance arc of gas conversion process significantly enlarges when the fuel utilization increases from 50% to 75%. The decrease of gas flow rate limits the cell performance. This behavior also validates that the impedance arc dominating the frequency below 0.1 Hz is contributed by the concentration process of gas conversion over the anode.

5.4. Conclusion

The single cells of tubular solid oxide fuel cell (T-SOFC) fueled directly with reformate mixture are studied by impedance measurement and equivalent circuit (EC) simulation in this chapter. Based on the mechanisms put forward for SOFC button cells and pellets with pure H_2 fuel supplement, a non-ideal EC model with four time constants was proposed for impedance simulation. Due to the complexity of SOFC mechanisms and the difficulty of SOFC operation at varying conditions, the proposed EC model lacks validation for impedance interpretation. However, the impedance spectra measured under several different operation conditions, though limited, provide a preliminary validation for the physical interpretation of EC elements. The conduction of oxygen-ion through electrolyte is the main contribution to the ohmic resistance. The adsorption process of
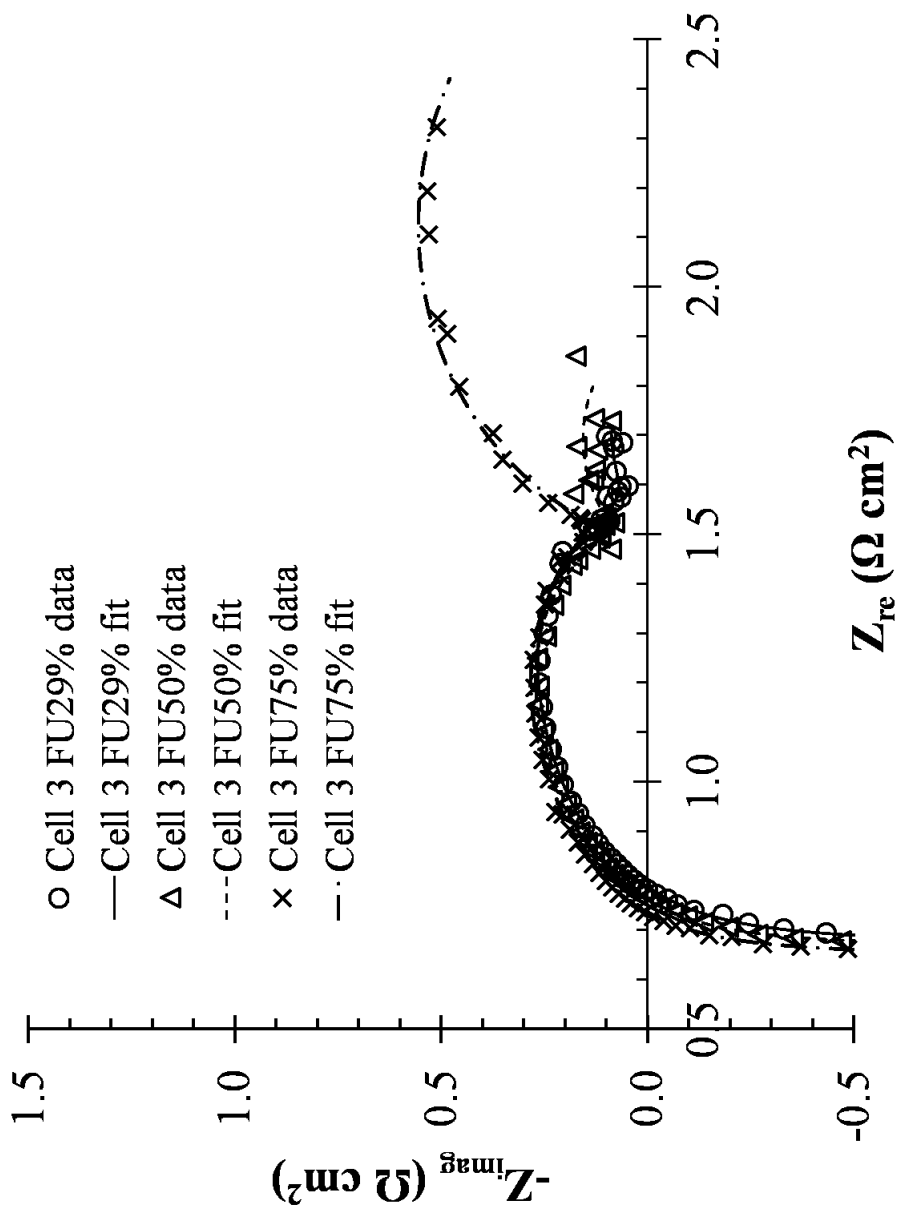
Figure 5.8. Impedance spectra of Cell 3 measured when operating with a fuel utilization (FU) of ($\circ$) 29%, ($\triangle$) 50%, and ($\times$) 75% along with their fit curves simulated from the non-ideal EC model (Figure 5.3). The operating temperature is set at 750°C, with a current density load of 120 mA cm^{-2}.

127

hydrogen and the adsorption process of oxygen are considered as rate determining steps of the chemical reaction processes on both electrodes. The contribution to the diffusion process is ascribed but not limited to the gas diffusion process of O_2 to cathode electrode. The impedance contribution from surface diffusion process of adsorbed oxygen can also be considered for the diffusion impedance arc. The impedance contribution of gas conversion process is confirmed by studying the effect of fuel utilization on cell performance.

Reference

[1] S. Primdahl, M. Mogensen, Journal of the Electrochemical Society, 145 (1998) 2431-2438.

[2] R.U. Payne, Y. Zhu, W.H. Zhu, M.S. Timper, S. Elangovan, B.J. Tatarchuk, International Journal of Electrochemistry, 2011 (2011).

[3] M.J. Jorgensen, M. Mogensen, Journal of the Electrochemical Society, 148 (2001) A433-A442.

[4] N.Q. Minh, T. Takahashi, Science and Technology of Ceramic Fuel Cells, Elsevier Science, 1995.

Chapter 6

EIS Application to Ni-MH Rechargeable Batteries

EC Simulation and Characterization of Batteries
and Study of Correlation between State-of-Charge and Impedance

6.1. Introduction

Two commercial nickel metal-hydride (Ni-MH) rechargeable battery D cells are studied by impedance measurement and EC simulation to perform cell characterization, degradation diagnostics, and SoC study. The content included in this chapter is in the process of submission as a journal article to Applied Energy. To avoid duplicate content in this dissertation, the introduction and part of the experimental details are not included in this chapter.

The purpose of this work is not limited to characterize two Ni-MH rechargeable batteries through impedance measurement and EC simulation. It also analyzes and explains the interpretation of battery impedance and the validity of EC model based on battery chemistry. The change of impedance at different SoC level studied in this work provide important experimental data for power prediction and improvement of smart charging systems.

6.2. Experimental details

Two sealed Ni-MH rechargeable batteries were studied by AC impedance in this work, numbered Cell A and Cell B respectively. They are D-size cylindrical cells with a

height of 60 mm and a diameter of 32 mm. These two commercial Ni-MH cells were originally purchased from a Radioshack® store (a division of Tandy Corp., Fort Worth, TX) in a brand new condition. The rated voltage is labeled at 1.2 V and the original cell capacity is rated at 4500 mAh (Radioshack® #23-519).

Performance degradation was gradually occurring in the Ni-MH Cell A and Cell B due to years of charge-discharge cycles and storages. The degradation can be reflected quantitatively by an decrease of cell capacity or an increase of cell impedance. Any irreversible changes of active electrode materials, electrode structures, and electrolyte compositions can cause cell degradation. Based on the current knowledge of rechargeable battery technology, a gradual reduction of cell capacity is inevitable, but a cycle life of about 500 charge-discharge cycles [1] can be generally achieved by sealed Ni-MH batteries with regular operation. After aging, the two commercial Ni-MH rechargeable batteries Cell A and Cell B were measured at 3702 mAh and 4362 mAh [2], less than 4500 mAh as specified by the manufacturer.

For impedance measurement at a certain capacity level, the specified amount of charge was input to the fully-discharged cells at a rate of $0.2C$. The percentage of the input capacity to the cell capacity is defined as state-of-recharge (SoR), *i.e.* the ratio of charge input to the rated cell capacity:

$$SoR = \% \; \frac{Amount \; of \; Charge \; Input}{Cell \; Capacity} \qquad (6.1)$$

As described in our published work [2], SoR is different from SoC but has certain correlation to it. When the specified SoR level was reached, the impedance measurement was applied to the cells under a *dc* load current of $0.1C$ (discharge process). Thus, the

loaded *dc* current is 370 mA for Cell A, and 436 mA for Cell B. Gamry FC350^{TM} fuel cell monitor, connecting to TDI-Dynaload$^®$ RBL488 programmable load, was employed to obtain impedance spectra when the frequency swept from 10 kHz down to 0.01 Hz. The impedance data were recorded at a rate of 5 points per decade frequency. When finishing the impedance measurement, the cells were continuously discharged to the cut-off voltage of 1.0 V at a rate of 0.2*C*. In other words, the cells were discharged to a SoC level of 0% after each impedance test. The impedance measurement at a higher SoR level was then began by repeating this procedure. The proposed EC model was then used to simulate the measured impedance spectra in Gamry Echem Analyst. The mode of hybrid EIS was selected in this work for Ni-MH cell measurement. The amplitude of the desired voltage perturbation *ΔV* was set at 5 mV.

After conducting all the impedance measurements and other performance tests [2], the cells were broken down to get samples of the negative electrodes. The electrode composition was then analyzed by energy dispersive X-ray spectroscopy (EDX or EDS). EDS is a bulk analytical technique used to qualitatively and quantitatively detect element composition. It is able to probe about 3-4 μm below the surface of the powder and has a sensitivity of about 1000 ppm for elements from Beryllium (Be) with atomic number 4 to Uranium (U) with atomic number 92. The electrode samples were powdered and pressed into double-sided C tape on the EDS specimen mount. The specimen should be thick enough to completely cover the tape. The composition of metal alloy used for the negative electrodes were then detected by identifying the metal elements and their percentage.

6.3. Results and discussion

6.3.1. Electrode compositions

The formulas of metal hydride alloys used for commercial Ni-MH batteries are quite different one from the other, but they are basically follow the disordered AB_5 type, A_2B_7 type, or disordered AB_2 type [3]. Each type has its typical components. However, in all cases, A refers to rare earth mixture and B refers to transition metals. Following Ovshinsky's pioneering metal alloy structure for battery electrodes [4], the disordered AB_5 type mischmetal (Mm) alloy has been developed to the most commercial level performing better cycle ability than other alloys [5].

In this work, EDS reports that the electrode samples roughly follow the atomic ratio of AB_5. A type elements include Lanthanum (La) and Cerium (Ce). B type elements include Nickel (Ni), Cobalt (Co), Aluminum (Al), and Manganese (Mn) with the primary component of Ni. Small amount of Potassium (K) is also detected. It is introduced by contacting with the electrolyte. Mn is able to adjust the metal-hydrogen bond strength [6]. And the existence of Al and Co significantly promotes electrode kinetics [3, 6]. The formula of this AB_5 type hydride alloy can be expressed as $(La_{9.70}Ce_{4.39})(Ni_{60.75}Co_{6.66}Al_{3.59}Mn_{4.45})$, following Ovshinsky's expression [3].

6.3.2. Impedance spectra and EC simulation

Two batteries are expected to have similar performance due to identical specifications. In Nyquist plots (Figure 6.1), the impedance spectra of both batteries consist with two overlapped semi-circles at higher frequency region and a straight tail at lower frequency region. However, Cell B has a significantly larger impedance than Cell A. The impedance of Cell B also shows greater changes with increasing SoR level than
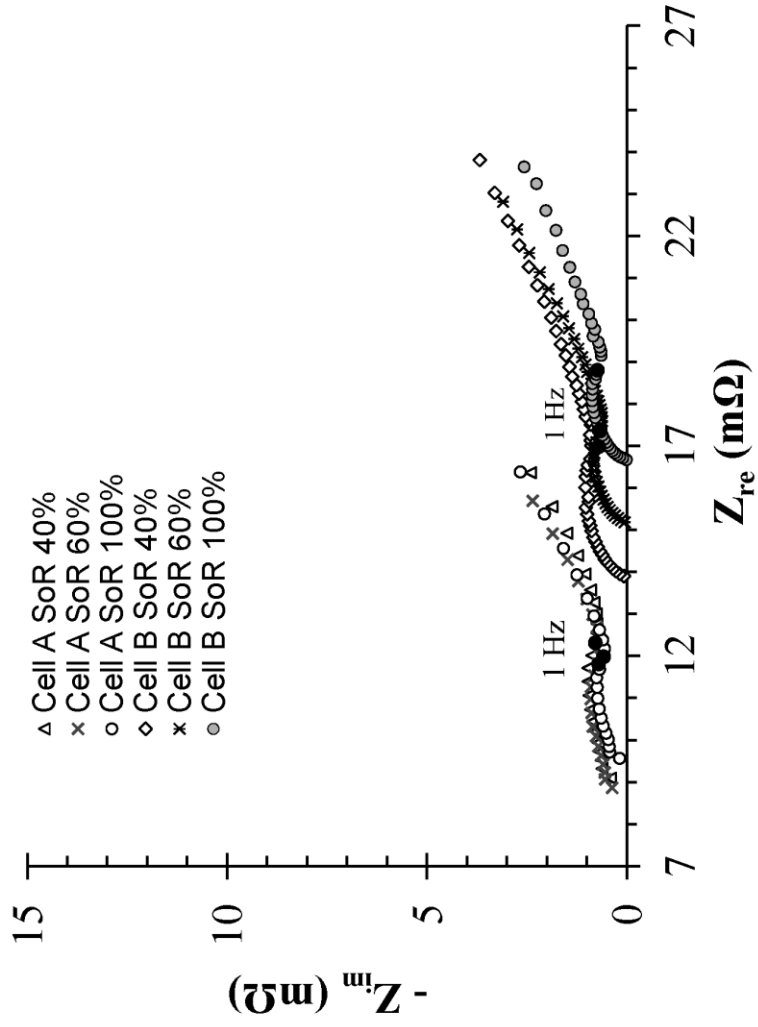
Figure 6.1. Impedance spectra of Ni-MH battery Cell A and Cell B measured after charging to the SoR level at 40%, 60%, and 100%. The impedance points measured at the frequency of 1 Hz are highlighted in the plot (●).

Cell A. The different magnitude and behavior of impedance spectra represent different SoH of two batteries.

According to the shape of impedance spectra, one parallel (QR) sub-circuit in series with one modified Randles circuit was proposed to simulate the measured impedance spectra (Figure 6.2). A typical Randles circuit (Figure 6.3) consists of one ohmic resistance R_Ω, one parallel ($C_{dl}R_{ct}$) sub-circuit behaving as a semi-circle in Nyquist plot, and one Warburg element (symbol in W) behaving as a unit slope line at the lowest frequency region [7]. This typical model considers faradaic impedance contributed by both kinetic reaction processes and diffusion processes. Since two overlapped semi-circles are observed from the impedance spectra of Ni-MH cells (Figure 6.1), one more parallel (CR) sub-circuit is added in series with Randles circuit to derive the ideal EC model for Ni-MH cells (Figure 6.3). Three constant phase elements (CPEs, symbol in Q) are used to replace two ideal capacitors and one Warburg element (W) in the case of non-ideal processes. The non-ideal EC model shown in Figure 6.2 is finally derived after these modifications.

Kuriyama [8] proposed a four time constant EC model for their metal hydride electrodes. The model consisted of three (CR) parallel circuits and one Warburg element. The fitting values of model elements were used to study the deterioration mechanism of electrodes without showing the fitting curves. However, EC models having less time constants were preferred to avoid redundancy. Cheng [9] and Buller [10] chose EC models with less time constants to simulate the impedance spectra of their battery systems. In this work, a three time constant EC model is proposed for battery simulation based on the behavior of our impedance spectra.
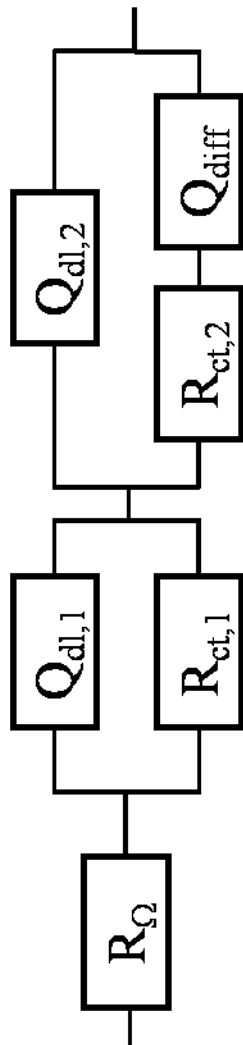
Figure 6.2. The non-ideal EC model employed to simulate the impedance spectra measured from both Ni-MH rechargeable batteries.
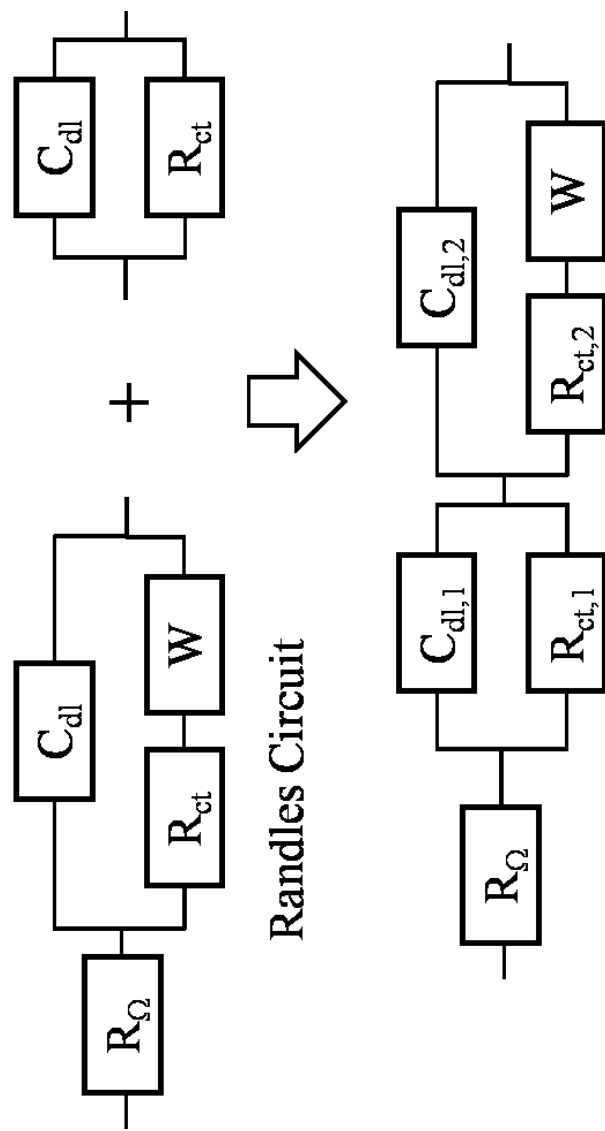
Figure 6.3. The ideal EC model for the Ni-MH rechargeable batteries, structured based on Randles circuit.

Figure 6.2 illustrates the EC model employed for the simulation of both Ni-MH rechargeable batteries. The fitting curve shown in Figure 6.4 simulates the impedance spectra of Cell A measured at 30% SoR level. The pure resistor R_Ω refers to the smaller intercept of impedance spectra in real axis. Two parallel sub-circuits ($Q_{dl,1}R_{ct,1}$) and ($Q_{dl,2}R_{ct,2}$) are used to simulate two overlapping impedance arcs in higher frequency range. For non-ideal capacitive behavior, the exponential numbers of $Q_{dl,1}$ and $Q_{dl,2}$ are expected to stay in the range between 0.8 and 1. The element Q_{diff} simulates the straight lines in the lowest frequency range for the non-ideal Warburg behavior with an exponential number less than 0.5.

The fitting curves shown in Figure 6.5 and Figure 6.6 simulate impedance spectra of Cell A and Cell B at different SoR levels by the proposed EC model. In higher frequency range, the two parallel (QR) circuits simulate the measured impedance spectra quite well. The difficulty remains in low frequency region. The fitting curves gradually deviate from the impedance data when the frequency decreases to lower than 1 Hz. This deviation becomes more significant at higher SoR levels, especially at 100% SoR level. Similar fitting deviation can be observed in Ruiz's simulation of the MH electrode with a mathematical model [11]. Li's fitting curves [12] for their nickel electrodes cannot provide references for diffusion impedance simulation because they only published fitting results for charge transfer impedance at high frequency region. Other impedance studies of Ni-MH systems [8, 9, 13, 14] rarely revealed fitting curves comparing to measured impedance spectra. The attentions were usually paid to faradaic impedance at higher frequency region contributed by hydrogen oxidation reaction (HOR) and NiOOH reduction reaction.
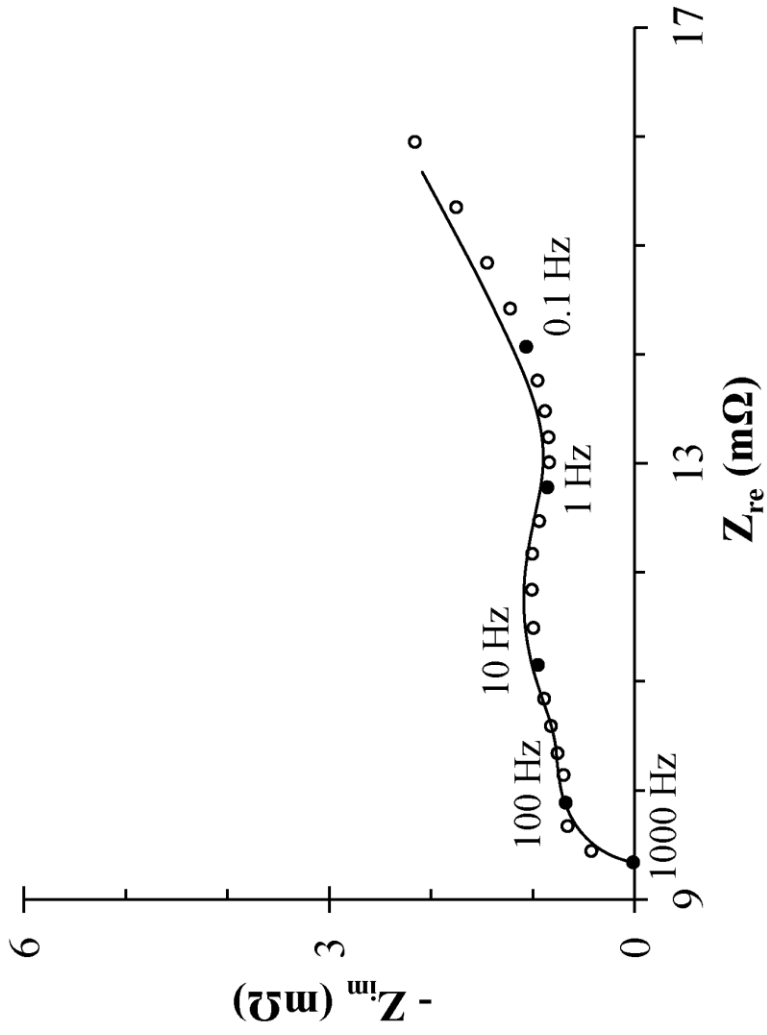
Figure 6.4. Impedance spectra measured from Cell A at the SoR level of 30% and simulated by the EC model proposed in Figure 6.2.
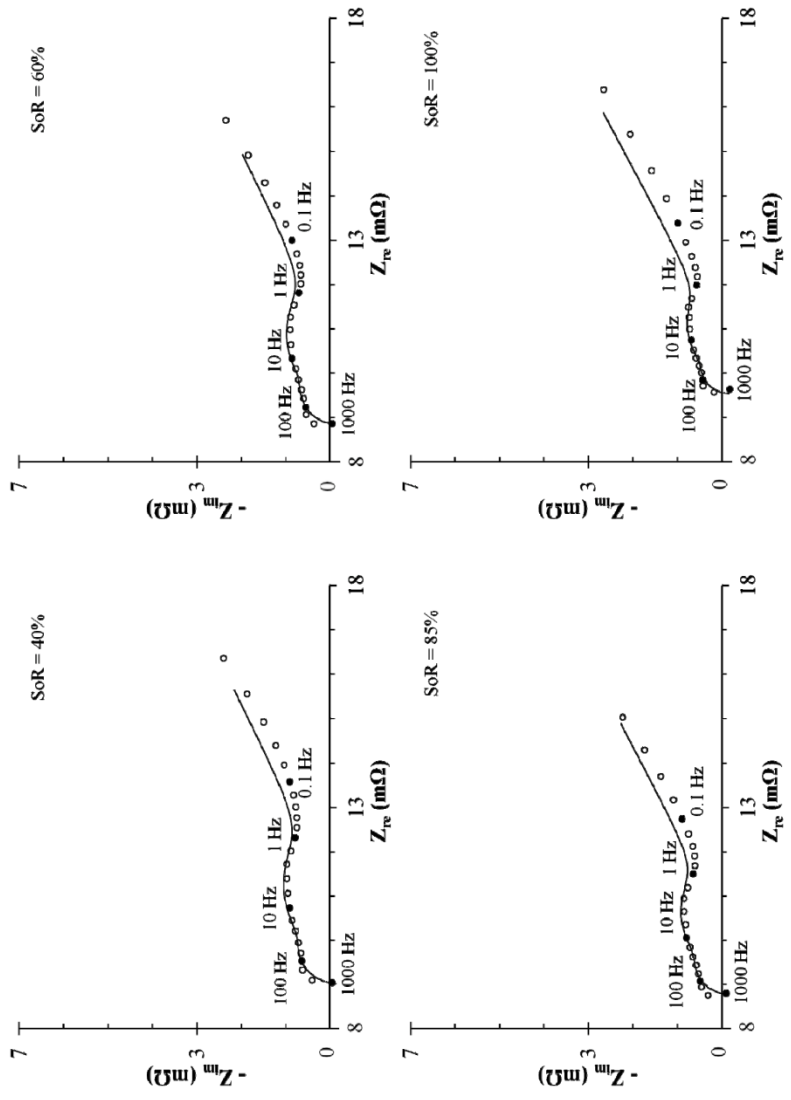
Figure 6.5. Impedance spectra measured from Cell A at different SoR level and their fitting curves simulated from the EC model shown in Figure 6.2.
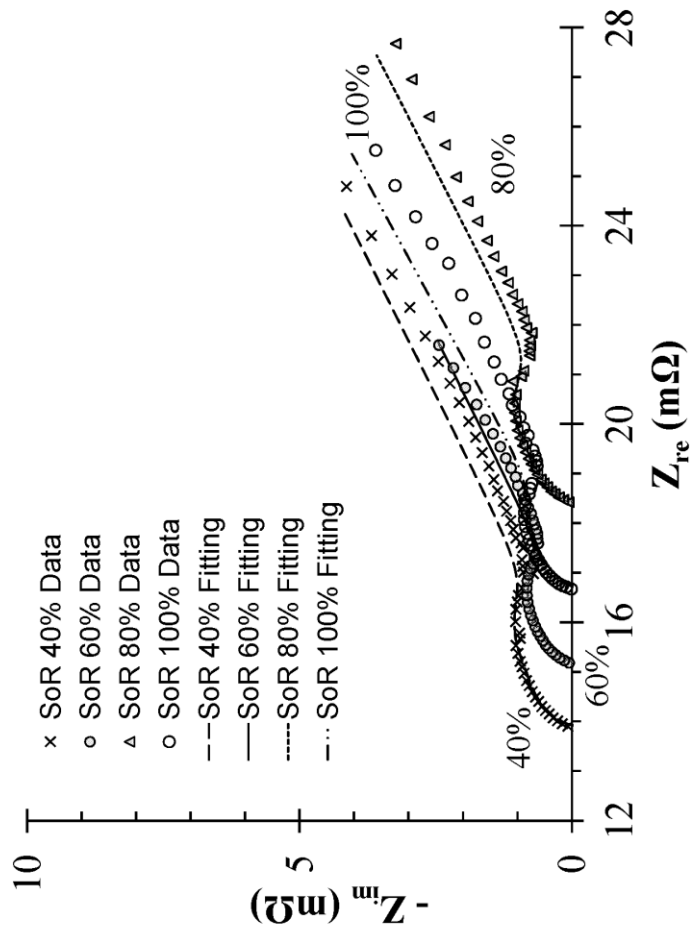
140

Figure 6.6. Impedance spectra measured from Cell B at different SoR level and their fitting curves simulated from the EC model shown in Figure 6.2.

6.3.3. EC element interpretation

The pure resistor R_Ω in series with all other EC elements is contributed by ohmic resistance. It comprises the resistance of cell components (electrodes, electrolyte, and conducting substrates) and resistance introduced by contact and connection. The parallel sub-circuits $(Q_{1,dl}R_{1,ct})$ and $(Q_{2,dl}R_{2,ct})$ refer to charge transfer processes related to kinetic reactions occurring on each electrode. The diffusion element Q_{diff} is connected with $(Q_{2,dl}R_{2,ct})$ in the EC model. The EC arrangement ascribes the major contribution of the diffusion impedance to the electrode where the kinetic process of $(Q_{2,dl}R_{2,ct})$ occurs.

Cell mechanisms are the basis of EC simulation and impedance interpretation. The electrolyte of commercial Ni-MH rechargeable batteries is usually a concentrated potassium hydroxide (KOH) solution. The mechanism of discharge process can be expressed by the overall electrochemical reaction [1] as:

$$NiOOH + MH \xrightarrow{\text{discharge}} Ni(OH)_2 + M, E^0_{cell} = 1.35\ V\ vs\ SHE \qquad (6.2)$$
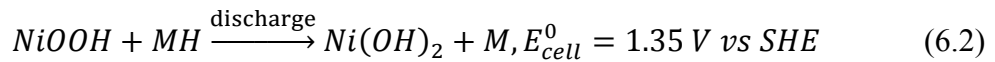
The reactant nickel oxyhydroxide (NiOOH) refers to the active material of positive electrodes. The reactant MH refers to the hydrided metal alloy of negative electrodes, that is hydrogen (H_2) absorbed into metal alloys. The overall mechanism of charge process is simply the reversing reaction of Eq. 6.2. However, it was proved that the electrode kinetics was asymmetric. Batteries usually undertake larger impedance during charge process than discharge process under the same measuring conditions [14]. The mechanisms discussed below are typically for discharge process.

6.3.3.1.Mechanism on negative electrodes

The half-cell process on the negative electrode is called the dehydriding reaction [13]. It can be expressed step by step as:

a) Hydrogen atoms adsorbed in metal alloy transfer from bulk sites to surface sites, that is metal alloy sites at the interface of electrode and electrolyte:

$$M_B \cdots H_{ad} + M_S \longrightarrow M_S \cdots H_{ad} + M_B \tag{6.3}$$
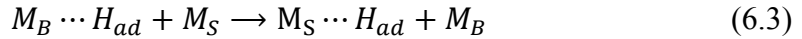
where H_{ad} refers to the hydrogen atom adsorbed in the metal alloy; M_S and M_B refer to the empty sites of metal alloy on surface and in bulk, respectively. Viitanen [15] explained this process as hydrogen released from the hydride phase to form adsorbed hydrogen atoms.

b) HOR at the electrode/electrolyte interface, that is a charge transfer step coupled by the diffusion process of hydroxide ions from bulk electrolyte to the electrode/electrolyte interface:

$$OH_B^- \longrightarrow OH_S^- \tag{6.4}$$

$$M_S \cdots H_{ad,S} + OH_S^- \longrightarrow M_S + H_2O_S + e^- \tag{6.5}$$
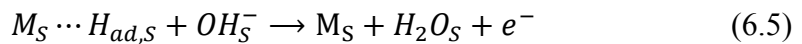
where OH_B^- and OH_S^- refer to the hydroxide ions in the bulk of electrolyte and at the interface of electrode/electrolyte, respectively; H_2O_S is water atoms produced by the HOR process at the electrode/electrolyte interface.

c) Transport of water molecules away from electrode/electrolyte interface to bulk electrolyte

$$H_2O_S \longrightarrow H_2O_B \tag{6.6}$$

where H_2O_B is water molecules in bulk electrolyte.

It is accepted that the rate limiting step on the negative electrode is the one-electron transfer kinetic process (Eq. 6.5) when there is sufficient hydrogen atoms adsorbed in the metal alloy sites on electrode surface. Diffusion of hydrogen atoms from bulk electrode to surface sites (Eq. 6.3) is a semi-infinite diffusion process featured by Warburg behavior at low frequency. This process does not have significant effect on cell impedance under general conditions [13, 16], but will become the rate limiting process at low temperature [17] due to decrease of diffusion coefficient. The mass transfer process of hydroxide ions (Eq. 6.4) from bulk electrolyte to electrolyte/electrode interface is a porous bounded diffusion process. This process is generally negligible unless batteries are operated under a large *dc* current load. The effect of hydroxide ion diffusion process become significant because its transfer rate lags behind the electrode kinetics. The transfer process of water molecules (Eq. 6.6) can be neglected when compared to other processes, because its concentration in electrolyte are assumed to be large enough [13] and globally constant during battery operation [18]..

6.3.3.2.Mechanism on positive electrodes

Zimmerman [19] proposed a mechanism for the discharge process on the positive electrodes. Following his idea, the step-by-step reaction can be explained as

a) Transport process of water molecules from bulk electrolyte to the interface of electrolyte and electrode, followed by the formation of proton at catalytic site at the interface:

$$H_2O_B \longrightarrow H_2O_S \qquad\qquad (6.7)$$

$$H_2O_S \longrightarrow OH_S^- + H_S^+ \qquad\qquad (6.8)$$

b) Transport process of hydroxide ions from the interface back to the electrolyte bulk:

$$OH_S^- \rightarrow OH_B^- \qquad (6.9)$$

c) Reduction reaction of electrode active material NiOOH, that is a charge transfer process coupled by the diffusion process of proton from the surface site to the charge transfer site in the electrode bulk:

$$H_S^+ \rightarrow H_B^+ \qquad (6.10)$$

$$NiOOH + H_B^+ + e^- \rightarrow Ni(OH)_2 \qquad (6.11)$$
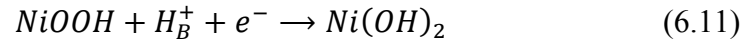
The situation on positive electrodes is different from what discussed above for negative electrodes. Diffusion processes are considered as the rate limiting step [19], because the effect of diffusion process on nickel hydroxide electrode is normally observed under general battery operating conditions [19]. This means the charge transfer process expressed as Eq. 6.11 is not the rate limiting process. And the diffusion process of proton in positive electrode (Eq. 6.10) is regarded as the rate limiting step under normal discharge process. The impedance of proton diffusion process presents the Warburg behavior.

6.3.3.3. Full battery impedance

The impedance arcs of semi-infinite diffusion processes can be observed from impedance spectra of both negative electrode studies [8, 16, 20] and positive electrode studies [21, 22]. However, only one Warburg behavior arc is observed at low frequency region from the impedance spectra of Ni-MH cells (Figure 6.1). Thus the difficulty of interpretation lies in the diffusion process. Karden [14] measured the half-cell impedance separately and compared the sum of them to the total cell impedance. The comparison

clearly illustrated that the negative electrode impedance dominated higher frequency region and the diffusion impedance in lower frequency region was contributed by the positive electrode. Hammouche [18] also found that the nickel hydroxide electrode contributed the diffusion impedance to the full cell under normal discharge operation. Based on the discussion of half-cell mechanism in the previous section, the diffusion element Q_{diff} in this simulation work is ascribed to the rate limiting diffusion process of positive electrode. It is explained as the solid-state diffusion process of proton in nickel hydroxide electrode shown as Eq. 6.10. The ($Q_{2,dl}R_{2,ct}$) circuit connected with the diffusion element is applied to simulate the charge transfer process occurring on the electrolyte/positive electrode interface coupling with the reduction reaction of the active material NiOOH (Eq. 6.11). And the sub-circuit ($Q_{1,dl}R_{1,ct}$) is ascribed to the one electron transfer process of HOR occurring on the surface of the negative electrode.

6.3.4. Correlation between impedance and SoR

The correlation between SoR and SoC was studied on Cell B [2]. When certain amount of charge was input to Cell B, its SoR was calculated. Then, its SoC was measured by discharging Cell B to cut-off voltage at 0.2C. The comparison of SoR to SoC is plotted versus the amount of input charge in Figure 6.7. The value of SoR is identical to the value of SoC even when the SoC level increases up to over 80%. As SoR continue to linearly increase with the amount of input charge, the increase of SoC slows down. The value of SoC deviates from SoR at high SoC level, but within a small magnitude of difference. The reason is that the side reactions of oxygen reduction reaction (ORR) on positive electrodes (Eq. 6.12) compete for the input charges. To protect Ni-MH batteries under this overcharge condition, the capacity of negative
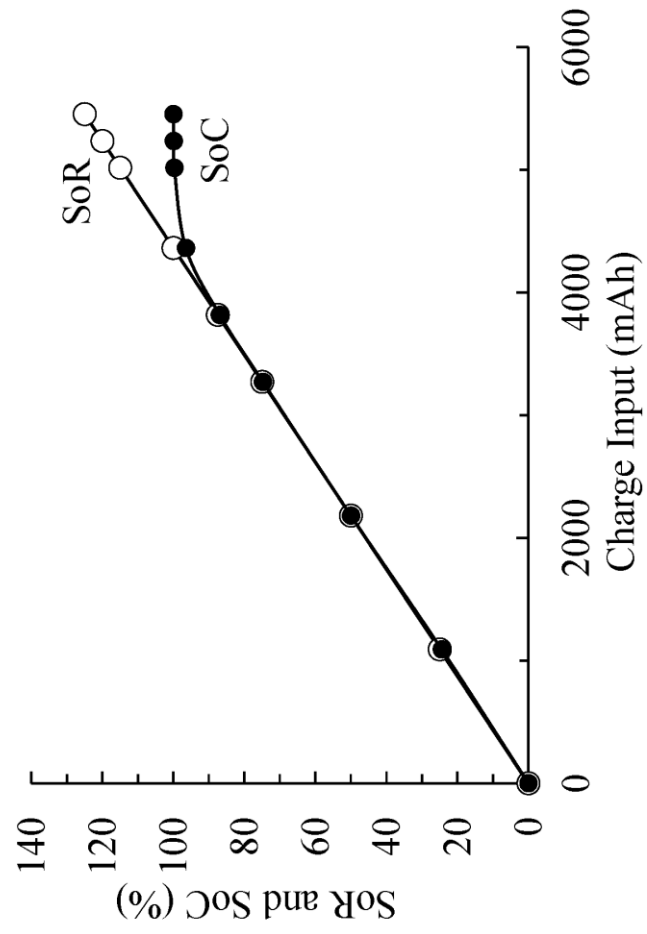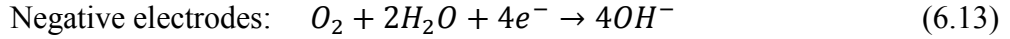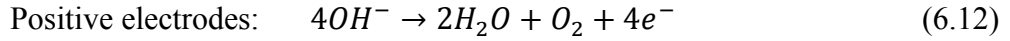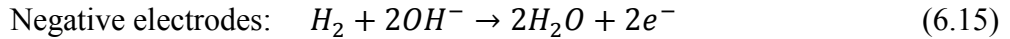
146

Figure 6.7. Correlation between SoC and SoR. Data are measured from Cell B [2].

electrodes are usually designed as 1.5 to 2 times of positive electrodes [1]. The oxygen evolved on positive electrodes then diffuses through electrolyte and reach negative electrodes to recombine with water molecular (Eq. 6.13). The side reactions on both electrodes under overcharge condition can be expressed as [1]:

$$\text{Positive electrodes:} \quad 4OH^- \rightarrow 2H_2O + O_2 + 4e^- \tag{6.12}$$

$$\text{Negative electrodes:} \quad O_2 + 2H_2O + 4e^- \rightarrow 4OH^- \tag{6.13}$$

Side reactions also competes with cell reactions when the operation falls into overdischarge conditions at low SoC levels [1]:

$$\text{Positive electrodes:} \quad 2H_2O + 2e^- \rightarrow H_2 + 2OH^- \tag{6.14}$$

$$\text{Negative electrodes:} \quad H_2 + 2OH^- \rightarrow 2H_2O + 2e^- \tag{6.15}$$
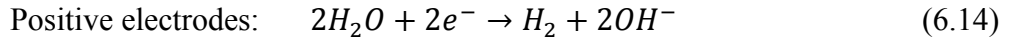
Hydrogen transfers from positive electrode to negative electrode through electrolyte. Side reactions occurring under both overcharge and overdischarge conditions consume charges without changing electrolyte and electrodes. In this way, Ni-MH cells are balanced but cell efficiency drops to an unsatisfactory level. Nelson pointed out that the realistic operation window for hybrid driving duty cycle of HEVs is from 30% SoC to 70% SoC [23]. As observed in Figure 6.7, within this charge-discharge window, the values of SoR are equivalent to SoC. When studying the correlation between cell impedance and SoC, SoR can be used as SoC during normal operation levels for simplification.

The change of ohmic resistance and charge transfer resistance with SoR level is shown in Figure 6.8 to 6.10. The resistances of Cell A and Cell B contributed by the same processes are plotted on the same figure for comparison. The ohmic resistance R_Ω of Cell

Figure 6.8. Ohmic resistance (R_Ω) of (○) Cell A and (●) Cell B at different SoR levels. Values are calculated by the EC model shown in Figure 6.2.

Figure 6.9. Charge transfer resistance contributed by HOR process on the negative electrodes of ($\triangle$) Cell A and ($\blacktriangle$) Cell B at different SoR levels. Values are calculated by the EC model shown in Figure 6.2.

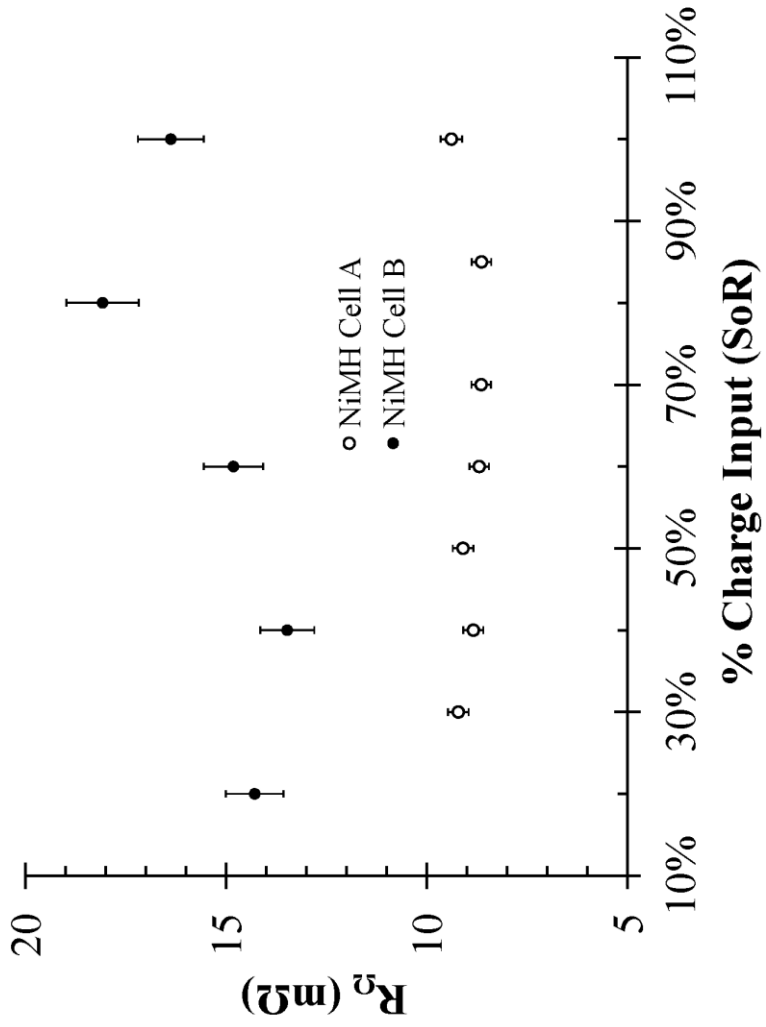**Figure 6.10.** Charge transfer resistance contributed by NiOOH reduction process on the positive electrodes of (□) Cell A and (■) Cell B at different SoR levels. Values are calculated by the EC model shown in Figure 6.2.

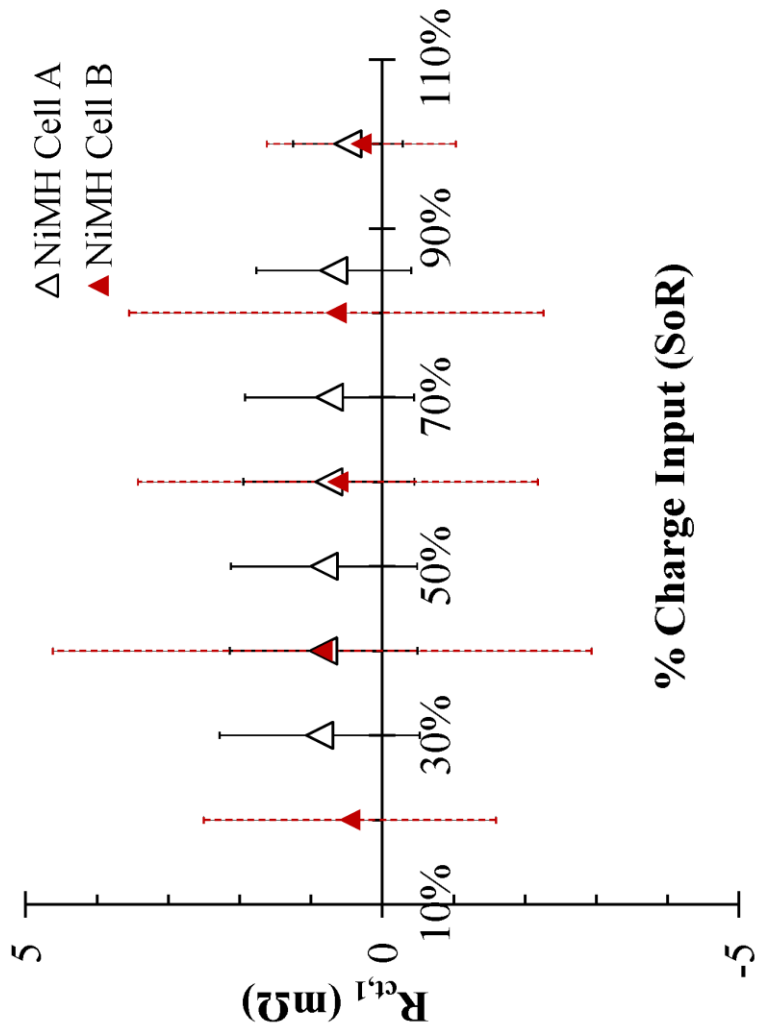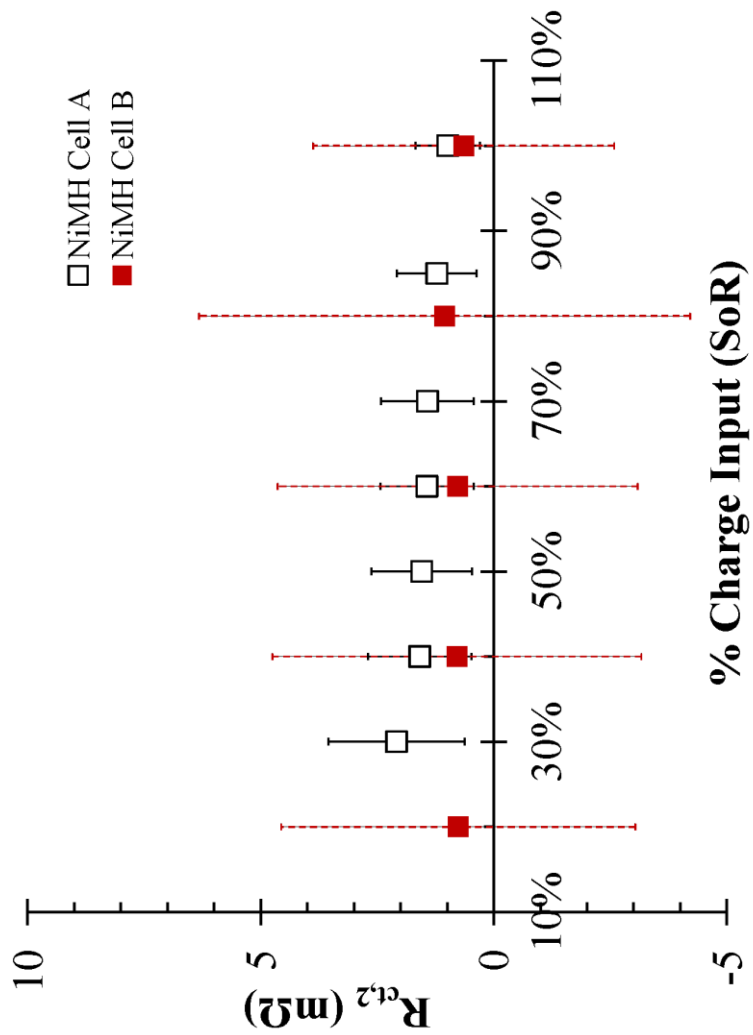A stays at a lower and more stable level than Cell B (Figure 6.8). Between 30% SoR and 70% SoR, R_Ω of Cell B increases with increasing SoR due to the reduction of NiOOH and the formation of $Ni(OH)_2$ on the positive electrodes. However, this expected variation is not significant in Cell A. Cell A has lower cell capacity after aging. The smaller change of electrode composition before and after the reduction of NiOOH presents a more stable R_Ω of Cell A than Cell B. The cell electrodes are not the only contribution to the ohmic resistance of Ni-MH cells. The lower R_Ω of Cell A does not determine the condition of its cell capacity. The status of electrolyte and any other auxiliary components also changes the value of R_Ω. The values of R_Ω at SoR levels lower than 30% and higher than 70% are slightly higher than R_Ω at SoR levels between 30% and 70% due to dissolution of H_2 and O_2 evolved by the side reactions.

The charge transfer resistances contributed by the HOR process on negative electrodes ($R_{ct,1}$) are plotted against SoR levels in Figure 6.9. $R_{ct,1}$ of Cell A decreases with increasing SoR level. This trend can also be observed from Cell B except the point at 20% SoR level. At higher SoR level, more active materials on negative electrodes facilitate the kinetic reactions and decrease the charge transfer resistance. The $R_{ct,1}$ of both cells stay at an equivalent value at each SoR level. This reflects an equivalent electrode kinetics of HOR process on negative electrodes of both cells. Although the cell capacity of two cells are different after aging, the capacity of negative electrodes is designed at a sufficient level for cell protection. The reduction of cell capacity does not have significant effect on HOR kinetics.

The cell capacity is dominated by the capacity of positive electrodes. Significant differences exist between the charge transfer resistances contributed by positive

electrodes ($R_{ct,2}$) of two cells (Figure 6.10). Cell B has a much smaller and more stable $R_{ct,2}$ comparing to Cell A. This means that more active materials are remained at the positive electrode of Cell B, corresponding to a faster kinetics and higher electrode capacity. The better cell capacity of Cell B can be reflected by the smaller charge transfer resistance of its positive electrode ($R_{ct,2}$). As a result of experimental measurement, the cell capacity of Cell A after aging is measured at about 3702 mAh, much smaller than the 4362 mAh of Cell B. Since the positive electrode of Cell A is more degraded comparing to Cell B due to insufficient amount of active materials, the production of $Ni(OH)_2$ at low SoR levels is expected to have more significant effects on electrode kinetic process (Eq. 6.11). Thus, the $R_{ct,2}$ of Cell A presents a more significant increase with decreasing SoR level as expected.

6.4. Conclusion

In this work, electrochemical impedance spectroscopy (EIS) and equivalent circuit (EC) simulation was applied to characterize two aged commercial Ni-MH rechargeable batteries. The proposed EC model is able to simulated the impedance spectra measured from both cells at varying SoR levels. The two cells should perform similar or even identical behaviors at brand new conditions; however, significant performance differences could be observed from their impedance spectra after aging. The EC simulation broke the total cell impedance down into several parts. According to the widely accepted battery chemistry, these parts are ascribed to the ohmic conduction, the electron transfer process of hydrogen oxidation reaction (HOR) on the negative electrode, the charge transfer process of NiOOH reduction process on the positive electrode, and the solid-state diffusion process on the positive electrode. The discrimination and

interpretation of impedance spectra illustrated that the difference between cell impedance is mainly contributed from ohmic resistance, and secondly contributed from the NiOOH reduction process on the positive electrode.

The two aged cells studied in this work were at different state-of-health (SoH). Their impedance were measured at different levels of state-of-recharge (SoR) during discharging process. The correlation of impedance contributed by different cell processes to SoR level was analyzed, along with its correlation to cell capacity level. The ohmic resistance increases with increasing SoR level, while the activation resistances of both electrodes decrease with increasing SoR level. The degradation of cell capacity can be reflected by the change of activation resistance of positive electrode.

So far, there has been only a few research focusing on impedance of Ni-MH batteries. More experimental data of commercial Ni-MH batteries measured under various SoH and SoC are required to establish a quantitative model between SoC and impedance. This work not only demonstrates the ability of EIS and EC simulation to perform battery diagnostics on commercial cells, but also provides a probability to find another method for determining the value of SoC, which can help to improve the smart-charging systems strongly required by hybrid electric vehicles (HEVs), electric vehicles (EVs), and other electronic products.

Reference

[1] D. Linden, T.B. Reddy, Handbook of Batteries, McGraw-Hill, 2002.

[2] W.H. Zhu, Y. Zhu, Z. Davis, B.J. Tatarchuk, Applied Energy, 106 (2013) 307-313.

[3] M.A. Fetcenko, S.R. Ovshinsky, B. Reichman, K. Young, C. Fierro, J. Koch, A. Zallen, W. Mays, T. Ouchi, Journal of Power Sources, 165 (2007) 544-551.

[4] Venkatesan S, Fetcenko MA, Corrigan DA, Gifford PR, Dhar SK, and Ovshinsky SR, MRS online proceedings library 1995; 393: 243; doi:10.1557/PROC-393-243.

[5] E. Barsoukov, J.R. Macdonald, Impedance Spectroscopy: Theory, Experiment, and Applications, Wiley-Interscience, 2005.

[6] S.R. Ovshinsky, M.A. Fetcenko, J. Ross, Science, 260 (1993) 176-181.

[7] A.J. Bard, L.R. Faulkner, Electrochemical Methods: Fundamentals and Applications, Wiley, 2001.

[8] N. Kuriyama, T. Sakai, H. Miyamura, I. Uehara, H. Ishikawa, T. Iwasaki, Journal of Alloys and Compounds, 202 (1993) 183-197.

[9] S.A. Cheng, J.Q. Zhang, M.H. Zhao, C.N. Cao, Journal of Alloys and Compounds, 293 (1999) 814-820.

[10] S. Buller, M. Thele, E. Karden, R.W. De Doncker, Journal of Power Sources, 113 (2003) 422-430.

[11] F.C. Ruiz, P.S. Martinez, E.B. Castro, R. Humana, H.A. Peretti, A. Visintin, International Journal of Hydrogen Energy, 38 (2013) 240-245.

[12] Y.W. Li, J.H. Yao, Y.X. Zhu, Z.G. Zou, H.B. Wang, Journal of Power Sources, 203 (2012) 177-183.

[13] W.L. Zhang, M.P.S. Kumar, S. Srinivasan, H.J. Ploehn, Journal of the Electrochemical Society, 142 (1995) 2935-2943.

[14] E. Karden, S. Buller, R.W. De Doncker, Journal of Power Sources, 85 (2000) 72-78.

[15] M. Viitanen, Journal of the Electrochemical Society, 140 (1993) 936-942.

[16] R.M. Humana, J.E. Thomas, F. Ruiz, S.G. Real, E.B. Castro, A. Visintin, International Journal of Hydrogen Energy, 37 (2012) 14966-14971.

[17] H. Wenzl, Batteries: Capacity, in: C.K. Dyer, P.T. Moseley, Z. Ogumi, D.A.J. Rand, B. Scrosati, J. Garche (Eds.) Encyclopedia of Electrochemical Power Sources, Elsevier Science, 2009, pp. 395-400.

[18] A. Hammouche, E. Karden, R.W. De Doncker, Journal of Power Sources, 127 (2004) 105-111.

[19] A.H. Zimmerman, P.K. Effa, Journal of the Electrochemical Society, 131 (1984) 709-713.

[20] L.O. Valoen, A. Lasia, J.O. Jensen, R. Tunold, Electrochimica Acta, 47 (2002) 2871-2884.

[21] M. Ortiz, D. Becker, G. Garaventta, A. Visintin, E.B. Castro, S.G. Real, Electrochimica Acta, 56 (2011) 7946-7954.

[22] Y.J. Leng, J.Q. Zhang, S.A. Cheng, C.N. Cao, Z.S. Ye, Electrochimica Acta, 43 (1998) 1945-1949.

[23] R.F. Nelson, Journal of Power Sources, 91 (2000) 2-26.

Chapter 7

Conclusions and Future Challenges

7.1. General conclusion

This dissertation systematically integrates the projects done in the past few research years, including the system characterization and performance evaluation of the proton exchange membrane (PEM) fuel cell stacks, the single cells of tubular solid oxide fuel cell (T-SOFC), and nickel-metal hydride (Ni-MH) rechargeable batteries. The competence of electrochemical impedance spectroscopy (EIS) is highlighted to perform dynamic *in-situ* characterization of energy conversion and storage systems.

Basic equivalent circuit (EC) elements and models are established according to the generalized mathematic models for electrochemical processes. However, the mechanisms, materials, and geometric structures differ from one power system to another. The behaviors and variation tendencies of impedance spectra are sensitive to the specific system processes and operating conditions of the power systems. Both having kinetic processes and diffusion processes, the fuel cell systems and Ni-MH rechargeable battery systems have significantly different characteristic impedance shapes. Even for fuel cell systems, the magnitudes and changing tendency of impedance arcs are different among the high temperature (HT) PEM fuel cell stack, the traditional PEM fuel cell stack, and the T-SOFC single cell tubes, because different electrolyte membranes provide different proton conduction mechanisms. On the other side, the non-uniqueness of EC

157

models brings great challenges to model validation. Large amount of data sets measuring under different operating conditions and system configurations are required to validate the simulation. The uniqueness of power systems are employed to validate and interpret EC models; while the non-uniqueness of EC models is utilized to generalize power systems into a comparable level and facilitate the establishment of standard procedures for performance evaluation and diagnostics of power systems.

7.2. Challenges to the Future

7.2.1. Energy conversion systems

Fuel cells are famous by its high energy efficiency and zero emission. However, the realization of commercial fuel cell systems subjects to several restrictions, not only of fuel cell itself but also of required up and down processes and auxiliaries. Hydrogen infrastructure is one of the most challenge issues closely related to fuel cell commercialization. The development of hydrogen storage and transportation is currently grinding to a standstill. Economic concerns and safety uncertainty bring additional difficulty to technological issues.

The alternative solution is to develop the fuel cell systems powered by methanol reformate. CO tolerance becomes the upmost concern to the direct methanol technologies. As analyzed in previous chapters, the novel phosphoric acid (PA) doped polybenzimidazole (PBI) successfully achieved the PEM fuel cell operation at elevated temperatures. However, current technology is still not sufficient to support a stable performance. The HT-PEM fuel cell stack is able to provide a power output at commercial level, but the novel MEAs are vulnerable to ambient and operating

158

conditions. Unclear mechanisms of proton conductivity and lack of experimental data bring further uncertainty to diagnose the degradation of the stack.

SOFC operated at an temperature up to hundred Celsius degree facilitates the pretreatment of fuels. It overcomes the CO poisoning issue for PEM fuel cell systems; however, the irreversible sulfur poisoning is still one of the most challengeable issue for SOFC operation. Although the operating temperature up to 1000ºC enhanced the kinetic processes, it also places strict requirements on the characteristics of materials of electrodes and electrolytes. Considering the recovery of heat, a lower operating temperature is desired but without sacrificing the energy efficiency. SOFC systems for operation around 400ºC to 600ºC are still under research. Without validated mechanisms, the feasibility and improvement of direct reformate operation is another big issue of SOFC research due to the complicated fuel compositions with reactants and reaction intermediates sensitive to electrochemical reaction and surface processes.

7.2.2. Energy storage systems

The Ni-MH battery has natural protection against overcharging and over-discharging with oxygen and hydrogen recombination inside the cell to form water. The overcharge process, overdischarge process, capacity retention, and the *in-situ* state-of-charge (SoC) parameter are quite important to the battery cycle life and calendar life time. The improvement of the battery energy storage and conversion efficiencies will significantly increase the overall energy efficiency and prolong the HEV's traveling miles per unit fuel use.

Impedance-based battery models are essential to the simulation of the complexity of modern power electronics. Battery behaviors are highly non-linear and their dynamic performance depends on different parameters such as temperature, service life-time, and state-of-charge. Future batteries for vehicle applications of electric vehicles (EVs) and hybrid-electric vehicles (HEVs) require the development of deep-cycle long-life EV batteries and high-rate long-life HEV batteries. Flat thin-plate structures have been made progress for deep-cycle requirement and cranking power needs. The related technology greatly reduces lead used in the system. The further work on newly structured batteries is necessary for examination of basic battery chemistry and improved electrode processes, exploration of mass transfer limitations, and investigation of the failure mode or mechanisms. Active material, utilization of active material, support structure, current collector, separator, electrolyte, and battery system maintenance (gas recombination and thermal management) are important factors for battery performance, state-of-healthy (SoH), and operating life-cycle time. Further advanced battery design concepts and structure improvements potentially give birth to the novel battery performance and promote the technical improvements for the high-rate and deep-cycle applications in future power reserve and energy storage applications.

The advanced vehicle systems or processes with higher energy efficiency are preferred to use for saving fuels and improving the mileage of per unit fuel use. Hybrid power-trains reduce undesirable emissions and also have their potential to improve fuel economy significantly. A highly efficient engine can charge the battery pack and propel the vehicle at the same time. The battery pack is also returned with some energy from the electric motor, which is served as another generator in the regenerative braking or

coasting mode. Therefore, the battery burst charge acceptance during frequent braking and power output capability during heavy acceleration are significantly important for the HEV fuel efficiency and engine emissions.

Publications

Refereed Journal Articles

[1] Ying Zhu, W. H. Zhu, and B. J. Tatarchuk, "Dynamic Analysis and Diagnostics of a High Temperature PEM Fuel Cell Stack", ECS Transactions 2013 50(2): 745-751.

[2] Ying Zhu, W. H. Zhu, and B. J. Tatarchuk, "In-situ Performance Analysis of a High Temperature Proton Exchange Membrane Fuel Cell Stack at Loads", ECS Transactions 2013 45(13): 67-72.

[3] Wenhua H. Zhu, Ying Zhu, Zenda Davis, and B. J. Tatarchuk, "Energy Efficiency and Capacity Retention of Ni-MH Batteries for Storage Applications", Applied Energy, 106 (2013) 307-313.

[4] Wenhua H. Zhu, Ying Zhu, and B. J. Tatarchuk, "A Simplified Equivalent Circuit Model for Simulation of Pb-Acid Batteries at Load for Energy Storage Application", Energy Conversion and Management, 52 (2011) 2794-2799.

[5] Robert U. Payne, Ying Zhu, Wenhua Zhu, Mark S. Timper, S. Elangovan and B. J. Tatarchuk, "Diffusion and Gas Conversion Analysis of Solid Oxide Fuel Cells at Loads via AC Impedance", International Journal of Electrochemistry, vol. 2011, Article ID 465452, doi:10.4061/2011/465452.

Book Chapter

[6] Ying Zhu, Wenhua H. Zhu and Bruce J. Tatarchuk (2013). "In-Situ Dynamic Characterization of Energy Storage and Conversion Systems", in: Energy Storage - Technologies and Applications, Ahmed Zobaa (Ed.), Chapter 10, pp. 239-270, InTech, Croatia, 2013. ISBN: 978-953-51-0951-8.

Conference Proceedings / Abstracts

[7] Ying Zhu, W. H. Zhu, and B. J. Tatarchuk, "An In-situ Dynamic Performance Study on an HT-PEM Stack and its Comparison to a Traditional PEM Stack", in: Proceedings of the 45th Power Sources Conference, pp.139-142, Las Vegas, Nevada, June 11-14, 2012.

[8] W. H. Zhu, Ying Zhu, and B. J. Tatarchuk, "Rate Performance and Energy Efficiency of Lithium-Ion Batteries for Storage Applications", in: Proceedings of the 45th Power Sources Conference, pp.13-16, Las Vegas, Nevada, June 11-14, 2012.

[9] W. H. Zhu, Ying Zhu, and Bruce J. Tatarchuk, "Energy Efficiency of Ni-MH Battery for Rapid Storage Application", in: Pittcon 2012 Conference & Expo - Energy & Fuels: Advanced Materials and Characterization Methods, #1690-6, Orlando, FL, March 10-15, 2012.

[10] Ying Zhu, W. H. Zhu, and B. J. Tatarchuk, "In-situ Electrical Characterization of a High Temperature PEM Fuel Cell Stack at Loads", in: AIChE Annual Meeting: Fuels and Petrochemicals Division - Alternate Fuels & New Technology - Fuel Cell Technology II, #373b, Minneapolis, MN, October 16-21, 2011.

[11] Ying Zhu, W. H. Zhu, and B. J. Tatarchuk, "Validation of the Equivalent Circuit Diagram for SOFC Modeling", in: AIChE Annual Meeting: Fuels and Petrochemicals Division - Alternate Fuels & New Technology - Fuel Cell Technology II, #373c, Minneapolis, MN, October 16-21, 2011.

[12] W. H. Zhu, Ying Zhu, and B. J. Tatarchuk, "Comparison of On-Board Hydrogen Production from Several Non-Fossil Fuel Feedstocks", in: Proceedings of the AIChE Annual Meeting: Environmental Division - Renewable Hydrogen Production I, #259b, Minneapolis, MN, October 16-21, 2011.

[13] Ying Zhu, W. H. Zhu, and B. J. Tatarchuk, "Breakdown of Polarization Losses in Button Sized SOFCs and a Prismatic Stack via Impedance Spectroscopy", in: Proceedings of the AIChE Annual Meeting: Fuels and Petrochemicals Division - Fuel Cell Technology and Alternate Fuels & New Technology, #641a, pp.1-7, Salt Lake City, UT, November 7-12, 2010.

[14] W. H. Zhu, Ying Zhu, and B. J. Tatarchuk, "Self-Discharge Evaluation of Ni-MH Battery Using Metal Hydride Alloy for Energy Storage Applications", in: Proceedings of the AIChE Annual Meeting: Materials Engineering and Sciences Division - Composites for Energy Applications, #139c, pp.1-3, Salt Lake City, UT, November 7-12, 2010.

[15] Ying Zhu, W. H. Zhu, and B. J. Tatarchuk, "AC Impedance Study of Mass Transfer Processes and Hydrogen Oxidation Reaction in Solid Oxide Fuel Cells", in: Proceedings of the 44th Power Sources Conference, pp.401- 404, Las Vegas, Nevada, June 14-17, 2010.

[16] W. H. Zhu, Ying Zhu, and B. J. Tatarchuk, "Advanced Pb-Acid Batteries for Potential High-Rate Power Applications", in: Proceedings of the 44th Power Sources Conference, pp.75-78, Las Vegas, Nevada, June 14-17, 2010.

[17] Ying Zhu, W. H. Zhu, and B. J. Tatarchuk, "AC Impedance in Characterization of SOFC and Interpretation of a Low Frequency Inductive Loop", in: Proceedings of the AIChE Annual Meeting: Fuels and Petrochemicals Division – Fuel Cell Technology, #89e, Nashville, TN, November 8-13, 2009.

[18] W. H. Zhu, Ying Zhu, and B. J. Tatarchuk, "Massive Deep-Cycle Pb-Acid Batteries for Energy Storage Applications", in: Proceedings of the AIChE Annual Meeting: Sustainable Electricity - Generation and Storage, #676d, pp.1-4, Nashville, TN, November 8-13, 2009.

[19] R.U. Payne, Ying Zhu, W.H. Zhu, and B. J. Tatarchuk, "Determining Kinetic and Mass Transfer Limiting Behavior of a SOFC via AC Impedance", in: Proceedings of the AIChE Annual Meeting: Novel Electrochemistry and Materials for Fuel Cells II, #768d, Philadelphia, PA, November 16-21, 2008.

[20] W. H. Zhu, R.U. Payne, Ying Zhu, and B. J. Tatarchuk, "Electrical Characterization of Lead-Acid Battery at Load for HEV Applications", in: Proceedings of the AIChE Annual Meeting: Battery and Fuel Cell Energy on Vehicles, #457a, pp.1-3, Philadelphia, PA, November 16-21, 2008.